Modeling System-level Iron Homeostasis in the Human Brain over the Lifespan

Zoe Cohen

Electrical Engineering and Computer Sciences
University of California, Berkeley

May 1, 2024

Modeling System-level Iron Homeostasis in the Human Brain over the Lifespan

by

Zoe Cohen

A dissertation submitted in partial satisfaction of the

requirements for the degree of

Doctor of Philosophy

in

Engineering - Electrical Engineering and Computer Sciences

in the

Graduate Division

of the

University of California, Berkeley

Committee in charge:

Professor Chunlei Liu, Chair
Professor Michael Lustig
Associate Professor Moriel Vandsburger

Fall 2023

Modeling System-level Iron Homeostasis in the Human Brain over the Lifespan

Abstract

Modeling System-level Iron Homeostasis in the Human Brain over the Lifespan

by

Zoe Cohen

Doctor of Philosophy in Engineering – Electrical Engineering and Computer Sciences

University of California, Berkeley

Professor Chunlei Liu, Chair

Iron is vital for proper functioning of the brain. Deficiency of iron can impair the formation of myelin sheaths, disrupting critical communication between neurons and causing disorder in movement, mood, attention, energy levels, and more. Although iron is critical for many neural processes, it is a delicate balance to maintain a healthy amount of iron. When unbound in the cell, ferrous iron can serve as a catalyst in the formation of reactive oxygen species which can cause DNA damage and cellular death in excess. Even in normal aging, iron accumulates in deep grey matter areas that are known to exhibit damage in neurodegenerative disorders like Alzheimer's and Parkinson's disease. We propose a mathematical model to describe the network transmission of iron throughout the brain over the lifespan, resulting in the accumulation seen in the deep grey nuclei.

The model is a linear Markov model with an input term, and the parameters are estimated using iron concentration estimates from Quantitative Susceptibility Mapping (QSM) Magnetic Resonance Imaging (MRI). We discuss the motivation behind using QSM for model training and how parameters were estimated. We also present an evaluation of the model performance and validation performed using a population collected separately from the training dataset. Finally, we share results for an application case of the model by comparing the model prediction when trained on healthy controls and subjects diagnosed with either Alzheimer's or mild cognitive impairment. These results show that our model is consistent in predicting iron transport dynamics for separate healthy populations and also predicts altered dynamics when trained on pathological QSM data.

Our model is able to predict iron transport dynamics that accurately reproduce the spatial and temporal distribution of iron seen over the lifespan. This work serves to help unravel the mystery of iron accumulation in the brain, a process which has implications for the treatment and early diagnosis of neurodegenerative disorders.

To Maddy, the best thing to come out of my PhD.

Contents

List of Figures

List of Tables

Acknowledgements

I wouldn't have made it this far without finding Chunlei Liu as an advisor, and for that I'm grateful. Thank you Chunlei for advising me on the project that is the focus of my dissertation, and for seeing me through to graduation. Chunlei's support and guidance have been invaluable to me, and he consistently pushed me to consider new perspectives on my research project. He taught me to see the bigger picture of what I was working on, and his feedback made me a much better researcher.

Thank you also to my fellow lab-mates for providing help and support: Jingjia Chen, Sang Min Han, Maruf Ahmed, Shafeeq Ibraheem, Miriam Hernandez Morales, Koyam Morales Weil, Tanya Deniz Ipek, Engin Baysoy, Katie Lamar, Ben Cary, Rebekah Zhao, and Tiffany Tran. Thank you to Laurance Lau for working with me during your undergrad and masters. I also would like to thank my other committee members, Moriel Vandsburger and Miki Lustig. I was a GSI for Moriel's class on medical imaging in spring of 2020, and I very much enjoyed working with him, even as we haphazardly made the transition to remote lecturing when the chaos of the pandemic hit.

My PhD journey hasn't exactly been linear. I started off in Ruzena Bajcsy's lab, thinking I'd be working on robotics. I soon learned she had other plans for me when she asked me about using MRI to measure muscles. I enjoyed our one-on-one meetings and getting to listen to Ruzena's ideas and stories, and I have a lot of fond memories from my time in the Human Assistive Robotic Technologies (HART) lab. I want to thank Ruzena for serving on my qualifying exam committee and attending my dissertation, as well as the entire HART lab for welcoming me to Berkeley. Thanks especially to Laura Hallock, Robert Matthew, Sarah Seko, Drew McPherson, Isabella Huang, Carolyn Matl, Mike Estrada and Gregorij Kurillo for helping me start off on the right foot. Thanks also to Miroslav Jascur, Ekin Karasan, and Zhiyong Zhang for helping me learn to use the MRI while working under Ruzena, which ultimately led me to my thesis project.

I owe Shirley Salanio an immense debt of gratitude for helping me find my current advisor, Chunlei Liu, and for every other time she has helped me with urgent matters both big and small. She has been so supportive and an integral part of my experience at Berkeley. Thanks also to Pat Hernan, Audrey Sillers, Susanne Kauer and Jean Nguyen for supporting me throughout my PhD.

Thank you to my friends for giving me life outside of grad school, I would not have made it to the end without you. I'm especially grateful to my roommates who lived with me for various amounts of time over five years in Berkeley and provided endless support and fun: Karl Krauth, Nathaniel Tarshish, Arya Reais-Parsi, and my sister Sara Cohen (who I love living in the same city as but will never share an apartment with again). Thank you also to my favorite neighbors and Germans, Axel Huebl and Lotti Obst-Huebl. You all are the absolute sweetest and I am so thankful for meeting you. Thank you to my other friends for hosting me at their houses, taking

x

me to parties, watching my cat Heather, making me laugh, listening to me, visiting me when I couldn't walk, jamming on guitar, going to concerts and on hikes, cooking, dancing, building houses and sailing with me, and for making the past six and a half years a lot of fun: Allison Sharrar, Aine Banfield, Jonah Siegel-Warren, Alex Reinking, Alex Moreno, Grace Dinh, Grace Nolan, Utkarsha Agwan, Robin Netzorg, Sarah Dean, Pavlo Manovi, Jackie Grode, Rachel Quint, Emily Dickas, Alyssa Morrow, Lucas Spangher, Stella Lu, P.J. Frederick, Varun Godbole, and Donna Ni. Thanks to Justin Eskesen for mentoring me as I make the transition into industry. I really enjoyed working under you at Reefgen, and the experience helped me regain my passion for engineering and solving problems. Thanks also to my cat, Heather, for occasionally sitting on me and for being the cutest.

I would like to thank my family for supporting me, for listening to me vent about grad school on countless occasions, and for trying to give me hope about life on the other side. Thank you to my Mom, Dad, my brothers Josh and Charlie, my Grandma and Poppa, and thanks again to my sister and also my second-best friend, Sara. Thanks to the Mulhall family for your unwavering support. Thanks to Simon, Sue, Callum, and Elliot, for being amazing and generous hosts in Australia on multiple occasions, and thanks to Professor Simon Foote for being my unofficial second advisor this past year.

As for my first best friend, thank you thank you thank you to my girlfriend, fiancé, and wife in the state of California, Maddy Foote. Maddy, you make me better every second I'm around you, and you are the main reason I am graduating today. I love you so much, and I could not have done this without you. Thank you for loving, supporting, and putting up with me. Also thank you for dragging me on vacations, those were really fun.

Chapter 1

Introduction and Motivation

1.1 Iron's role in the brain

Iron is necessary for several crucial processes in the body. It's the reason our blood is red [1]. It binds oxygen in hemoglobin, which is used throughout the body to make cellular energy, adenosine triphosphate (ATP), and iron acts as a critical player in this process [1], [2]. Iron also serves as an essential cofactor for various enzymes, in addition to facilitating DNA repair [1], [2]. In the brain, iron is required in large amounts for proper functioning, including for neurotransmitter synthesis and signaling, ATP production, and especially for the myelination of axons, which provides insulation for the transmission of neural signals [1], [3], [4].

Axons are long branches from the cell bodies of neurons which conduct electrical signals across relatively vast distances in the brain [5]. The propagation of electrical signals down an axon triggers a release of molecules called neurotransmitters. The end of one neuron's axon interfaces with branches off the cell body of another neuron, which have receptors that bind the released neurotransmitters. This process, called a synapse, is the mechanism of communication between neurons in the brain [5]. The transfer of electrical impulses down axons must be extremely fast for the brain to function properly. This speed is achieved by myelin, a lipid membrane which wraps around axons similarly to insulation on a wire [6], [7]. Iron is required in large amounts for myelination of axons, and in fact, most of the iron in the brain can be found within the cells that produce myelin, oligodendrocytes [3], [8], [9].

Iron is attained by the body through food and its absorption is controlled by the small intestine [10]. Studies on rats link the amount of iron in the diet to brain function reflected in behavior, indicating that problems occur outside of a specific range required for normal functioning [10]–[12]. At extremely high levels, excessive dietary iron can lead to dysfunction, manifesting as iron overload in the brain and functional impairments [11]. Iron deficiency is associated with problems as well. Iron-deficient children have higher incidence of anxiety, depression, and social and attentional issues [13]. These problems can persist even after the initial deficiency is resolved. There is increasing evidence that iron deficiency in the first year of life can have lasting structural effects on the brain, even translating to cognitive and behavioral problems later in life [14]. This is thought to be because iron is rapidly and preferentially acquired by specific brain regions during development, and there appears to be a distinct window of time during which this accelerated accumulation can occur [13], [15].

1.2 Spatiotemporal pattern of iron accumulation in the brain
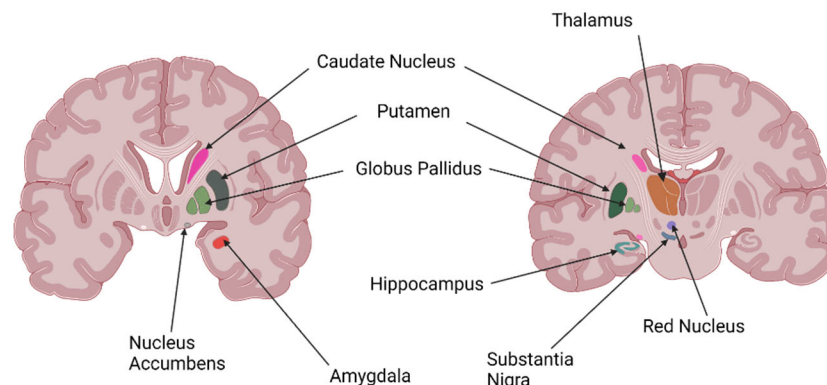
Figure 1.1: **Deep Grey Nuclei Regions of the Brain**. Deep grey matter regions of the brain include the caudate nucleus, putamen, globus pallidus, hippocampus, thalamus, amygdala, red nucleus, substantia nigra, and nucleus accumbens. Created with BioRender.com

Iron accumulates specifically in deep grey matter regions in the brain during development [13], [15]. Grey matter, mostly composed of neuronal cell bodies, is one of the two major tissue types in the brain, resulting from the distinct morphological aspects of neurons [5]. The other, white matter, is composed of the myelinated axon fibers [5]. The deep grey matter structures that accumulate high amounts of iron are found below the cortex, the outer, folded grey matter tissue of the brain, and include the basal ganglia, substantia nigra, hippocampus, amygdala and thalamus, among others (Fig. 1.1) [5]. Interestingly, these nuclei are responsible for many of the higher order brain functions that are affected by iron deficiency, particularly movement, cognition, and perception.

The basal ganglia, composed of the caudate nucleus, putamen, globus pallidus, and nucleus accumbens, are associated with control of voluntary movements, learning, cognition, and emotion [5]. The substantia nigra and red nucleus are also critically involved in coordinating movement [5]. These regions are shaped by neurotransmitters that are metabolically sensitive to brain iron levels [13], [14], [16]. Similarly, there is evidence that iron may serve an important regulatory role in the neurotransmitters that act in the hippocampus, thought to be the seat of memory in the brain, leading to improved memory by increasing the strength of nerve impulses along these pathways [17]. The amygdala is also involved in memory, as well as processing of fear and other emotions, and, finally, the thalamus is responsible for directing motor and sensory inputs from the body to other regions of the brain for processing and control [5]. Iron has been demonstrated to be important for the functioning of these regions as well [16], [18].

Not only do these regions selectively uptake iron in the developing brain, but they continue to accumulate iron throughout the lifespan [19]–[21]. This is partly due to a highly regulated, robust process that has evolved to control the storage, release, and transport of iron in the brain [22]–[24]. This phenomenon can be seen with Quantitative Susceptibility Mapping (QSM), which is a type of Magnetic Resonance Imaging (MRI) sensitive to iron stored in the brain [6], [19], [25], [26]. QSM images taken over the lifespan demonstrate the pattern of iron
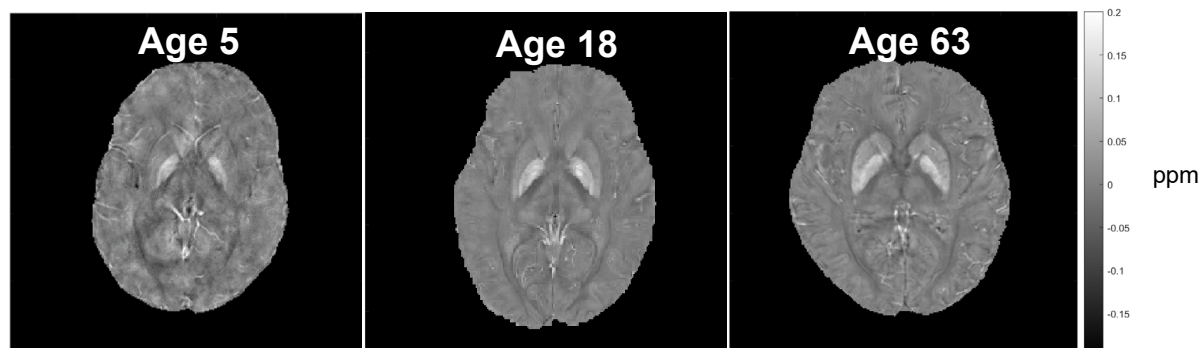
Figure 1.2: **Quantitative Susceptibility Mapping (QSM) Images over the Lifespan**. QSM images taken for subjects of varying ages show aging-associated iron accumulation, which appears as bright, in the deep grey nuclei regions of the brain. QSM is measured in parts per million (ppm). These images were collected by Y. Zhang et al. [20].

accumulation in the brain in deep grey nuclei regions and show that iron levels in these regions increase with age (Fig. 1.2).

It is unknown how or why iron is distributed this way in the brain. Answering this question would have profound implications for our understanding of the brain, as well as neurodegenerative disorders, many of which are hallmarked by alterations in the pattern of iron deposition associated with normal aging.

1.3 Implication for neurodegenerative disease

The same deep grey nuclei regions that preferentially accumulate iron are also the first ones to show dysfunction in neurodegenerative disorders like Alzheimer's and Parkinson's [27], [28]. In Parkinson's disease, damage is seen in the substantia nigra, which exhibits iron overload [29]. In Alzheimer's disease, regions of elevated iron colocalize with sites of destructive amyloid beta plaques, and alterations are seen in the normal pattern of iron deposition throughout the disease progression [30], [31]. Although it is clear that a certain amount of iron is required for the developing brain, there is a threshold beyond which iron is harmful [11], [15], [17], [32]. Excess iron can interact with oxygen to cause oxidative stress, and this likely plays a role in neurodegeneration [33]. An additional complicating factor is that the brain appears to become more sensitive to increased dietary iron with age [10], [12]. The question of how and why iron accumulates in deep nuclei regions in the brain has implications for understanding these disorders like Alzheimer's and Parkinson's that occur with advanced age.

1.4 Iron homeostasis in the brain

Because of the delicate balance between iron deficiency and overload, iron entry into the brain is highly regulated, and its distribution within the brain is also controlled by a network of transport

and storage proteins [22], [34]. Prominent players include transferrin (Tf), transferrin receptor (TFR), divalent metal transporter 1 (DMT1), ferroportin (Fpn), and ferritin (Ftn) [24], [35]. Tf and TFR are thought to provide the primary route of iron influx into the brain across the blood brain barrier (BBB) [22]–[24]. TFR is present on the luminal side of the brain microvascular endothelial cells (BMECs), which make up the BBB, and iron is taken up by these cells via receptor-mediated endocytosis of Tf-bound TFR [24], [36]. Separation from the Tf-TFR complex is facilitated by the acidic environment of the endosome, which then releases the non-Tf bound iron into the BMEC cytosol via DMT1 [36]. Afterwards, iron is ultimately transported into the brain by Fpn, the only known iron exporter [24], [37]. In addition to BMECs, Fpn is expressed in glial cells like astrocytes and oligodendrocytes, as well as neurons [34], [37]. Upon release from BMECs, non-Tf bound iron may be taken up by astrocytes before being distributed to neurons and other cells [34]. This is supported by the presence of DMT1, which can transport iron and other metal ions across cell membranes, on the end feet of astrocytes [9], [36]. Ftn is the major iron storage protein, capable of holding up to 4500 iron molecules [38]. These pathways formed by the proteins Tf, TFR, DMT1, Fpn, and Ft, are thought to make up the main mechanism of iron transport into brain regions, as well as storage.

Although the transport of iron across the BBB into the brain has been extensively studied, the transport of iron within the brain has not. It is clear that characterizing the process of iron homeostasis in the brain on the system level is critical for understanding neurodegenerative disorders. In this work, we outline a proposed mathematical model of iron homeostasis in the brain, with the goal of understanding how iron transport in the brain results in the spatially varying pattern of iron accumulation seen with age.

1.5   Dissertation Organization

This dissertation is organized as follows. In Chapter 2, we introduce a method of non-invasively measuring iron in the brain, Quantitative Susceptibility Mapping (QSM) Magnetic Resonance Imaging (MRI), and report on a correlation analysis we performed between QSM and iron homeostasis, as measured by gene expression. In Chapter 3 we define the proposed model, and in Chapters 4 and 5 we present results for estimating the model parameters with two different hypotheses. Chapter 6 details an attempt to address the limitations of QSM as a brain iron estimate by decomposing it into positive and negative susceptibility components. Chapter 7 presents an application case of using our model to predict altered iron transport dynamics in subjects with Alzheimer's disease or mild cognitive impairment. Finally, in Chapter 8 we discuss future work and conclusions.

Chapter 2

Evaluating Quantitative Susceptibility Mapping MRI as a Measurement of Iron in the Brain

We are interested in a non-invasive method of measuring iron in the brain that is both spatially localized and age-dependent. For this, we turn to quantitative susceptibility mapping (QSM) magnetic resonance imaging (MRI). MRI, and particularly QSM, is an imaging modality with specific strengths that apply well to the problem of studying iron in the brain. Various aspects of the MR signal are known to be sensitive to specific tissues, depending on the properties and molecular species present in those tissues [39]. QSM is an MRI technique that can quantitatively measure magnetic susceptibility, a tissue property that is dominated by iron in the deep grey nuclei regions of the brain [25], [40]. We will describe the source of the MR signal and how it changes depending on tissue properties, and then explain how the QSM is measured and calculated. We explain the biological basis for the QSM signal in the brain, and then describe a comparative analysis between QSM data and the expression of genes involved in iron homeostasis and myelination. The results of our analysis show that the QSM signal is highly correlated with the expression of iron transport and myelination genes in the deep grey nuclei regions of the brain, indicating that QSM is well-suited as an estimate of iron in the brain for use in our model of iron homeostasis.

2.1 Basic principles of MRI

MRI works by perturbing the hydrogen atoms within water molecules with magnetic fields [39]. Atoms with an odd number of protons or neutrons possess a property called nuclear spin angular momentum, and hydrogen is typically used in MRI as it is the most abundant and sensitive spin in the body [39]. Without an external magnetic field, the spins are oriented randomly, and the net macroscopic magnetic moment produced is zero [39]. When an external magnetic field is applied, the magnetic moment vectors of the nuclear spins align in the direction of the applied field and resonate at a frequency that is proportional to the strength of the applied field [39]. This frequency, called the Larmor frequency, can be written as $f = \gamma B$, where γ is the gyromagnetic ratio, and B is the magnetic field strength [39].

Conventionally, the external B0 field is applied in the longitudinal direction, which induces a net magnetization vector in the same direction [39]. The nuclear spins will remain in this equilibrium until the introduction of energy into the system in the form of a radiofrequency (RF) pulse [39]. Applying a radiofrequency (RF) pulse tuned to the Larmor frequency, B1, changes the direction of the induced magnetic field and tips it into the transverse plane, where an

RF receiver coil is placed [39]. After the cessation of the B1 pulse, the magnetization vector relaxes back up to its equilibrium position as the spins give off energy and continue oscillating at the Larmor frequency [39]. It is this signal, called the free induction decay (FID), that is measured and that provides contrast in an MR image. The FID is a damped sine wave, oscillating at the Larmor frequency [41]. The damping of this signal is called T2* decay and causes the FID to decay exponentially with time constant T2* [41]. In addition to spin-spin relaxation, the value of T2* is governed by molecular differences between tissues, particularly magnetic field inhomogeneities which can be caused by magnetic susceptibility, the ratio between the magnetization of a material when placed in an external magnetic field and the strength of the applied magnetic field [42]. QSM is an MRI modality that is sensitive even to tiny magnetic field inhomogeneities [26], [40]. In the brain, iron is largely responsible for the positive magnetic susceptibility signal, which makes QSM an excellent candidate as a non-invasive estimate of iron [6], [25], [43].

2.2 Introduction to QSM

QSM is an MRI modality in which the signal of each voxel in the image is a measurement of the corresponding magnetic susceptibility within that voxel [40], [44]–[47]. A susceptibility source warps the applied magnetic field which then alters the frequency of the proton spins, captured by the MRI phase of gradient echo signal [40], [48]. QSM measures the susceptibility across all voxels in the brain by modeling each voxel as a susceptibility source, and then solving backwards for the susceptibility distribution from the MRI phase [40].

In addition to being non-invasive and relatively high spatial resolution, QSM yields quantitative information about the susceptibility of tissues, which reflects their molecular composition [26], [49]–[52]. Iron and myelin are believed to be the two primary sources of susceptibility contrast observed in the brain [6], [19], [25]. Ferritin (Ft), the iron storage molecule, is paramagnetic and dominates the positive QSM signal in regions that accumulate iron [25], [51], [53], [54]. The molecular basis behind the positive susceptibility is Ft's large iron core, which can store up to 4,500 iron atoms [38]. In addition to its storage capacity, there is evidence that the heavy-chain subunit of Ft (H-Ft) can transport iron, and a receptor that binds H-Ft has been identified on myelinating oligodendrocytes [55], [56]. The relationship between the positive susceptibility signal and iron-loaded ferritin in the brain has been confirmed by both histology and dissection studies [6], [25], [42].

Besides iron-loaded Ft, the other main contribution to the QSM signal in the brain is myelin, which is diamagnetic and results in negative QSM in the white matter [19], [21], [25], [57]. Various genes have been implicated in the process of myelination, most of which are expressed by oligodendrocytes [58]. Oligodendrocytes are glial cells that wrap around the axons of neurons, forming the insulating myelin sheath [7]. Myelination is initiated by changes in gene expression, which prompt oligodendrocyte precursor cells to migrate within the brain, branch

morphologically, and form sheaths around axons [7], [59]. [58] define a set of genes involved in this process, including myelin basic protein (MBP), 2',3'-cyclic nucleotide 3'-phosphodiesterase (CNP), myelin-associated glycoprotein (MAG), myelin and lymphocyte protein (MAL), myelin-associated oligodendrocytic basic protein (MOBP), myelin oligodendrocyte glycoprotein (MOG), claudin-11 (CLDN11), proteolipid protein (PLP1), galactose-3-O-sulfotransferase-1 (GAL3ST1), proteolipid plasmolipin (PLLP), integrin-linked kinase (ILK), oligodendrocyte-myelin glycoprotein (OMG), kallikrein-related peptidase 6 (KLK6), oligodendrocyte transcription factor 2 (OLIG2), eukaryotic translation initiation factor 2 alpha kinase 3 (EIF2AK3), POU domain class 3 transcription factor 1 (POU3F1) and neuregulin 1 (NRG1). All of these are expressed by oligodendrocytes, except NRG1 which is expressed in neurons and astrocytes but acts to regulate the migration of oligodendrocyte precursor cells [60]. These genes are implicated in the production and reorganization of the lipids and proteins that compose the myelin sheath, many of which are diamagnetic [61].

Although the QSM image is captured at millimeter resolution, we wanted to assess whether the susceptibility signal from QSM could reflect iron homeostasis on a molecular level, as measured by gene expression. In Chapter 1, we introduced the players involved in the transport of iron across the BBB and within the brain. Gene expression can serve as a window into the underlying proteins involved in these processes [62]. This question has already been supported by other studies, particularly [63], which concludes that the expression of genes involved in iron homeostasis and myelination is correlated with the QSM signal in the deep grey nuclei. Other previous genome-wide association studies have shown a correlation between biomarkers of body iron levels and genes involved in iron transport and storage in the brain [64], [65]. However, these analyses find correlations across subjects and are limited by a single measure of expression for a given gene that is not localized to the brain but in the blood, therefore neglecting the spatial dimension of gene expression. For this reason, we use the Allen Human Brain Atlas (AHBA), a publicly available dataset of gene expression measured across regions of the brain, to expand upon these studies in characterizing the relationship between QSM and brain iron homeostasis [62], [66].

We conduct a comparative analysis between QSM and the expression of genes known to be involved in iron transport and myelination across brain regions, with a goal of further understanding the pathways by which iron selectively accumulates in deep grey nuclei regions of the aging brain. We found that QSM is related to the expression of genes relevant to iron homeostasis and myelination measured across these deep grey nuclei regions.

2.3   Comparison of QSM and Expression of Genes Involved in Iron Transport and Myelination: Methodology

We performed linear regressions between age-matched QSM and gene expression data across functionally distinct regions in the deep grey matter. A linear regression model was fit for each

of 15,627 unique genes from the AHBA microarray dataset, collected from six normal post-mortem brains, aged 24-57 (median 44), both male and female [62], [66], [67], and the average QSM of nine healthy subjects, aged 41-49 (median 45), both male and female, calculated across the same regions [20]. More information about these datasets, as well as processing and the set-up of the regression problem, are described as follows.

2.3.1 MRI acquisition and post processing

We calculated the average QSM signal in 34 distinct regions in the brain for nine healthy subjects age-matched to the median age of the AHBA dataset. The QSM dataset is described in [20]. Briefly, subjects were scanned on a 3T scanner (GE Healthcare Signa HDxt at Rui Jin Hospital in Shanghai, China) following approval of the institutional review board and signing of informed consent. T2*-weighted images were acquired using a three-dimensional multi-echo gradient echo sequence (TE1/spacing/TE8 = 5.468/3/26.5 ms, TR = 54.6 ms, original spatial resolution .86 x .86 x 2 mm^3 resampled to 1 x 1 x 1 mm^3). The QSM image was then reconstructed using STI Suite V3.0 (https://people.eecs.berkeley.edu/ chunlei.liu/software.html). The brain was extracted from each image using FSL's brain extraction tool (BET) [68]. Following Laplacian-based phase unwrapping and normalization, background phase removal was then performed using a variable-kernel Sophisticated Harmonic Artifact Reduction for Phase data (V-SHARP) method [53], [69], [70]. The radius of the spherical mean value filter varied from 1 pixel at the boundary of the brain to 25 pixels around the center of the brain [53]. Lastly, the STAR-QSM algorithm was used to reconstruct the QSM image from the filtered phase image [71]. The resulting susceptibility values were referenced relative to the mean susceptibility across the whole brain, which has been shown to be as reliable as using CSF as the susceptibility reference [19].

(a) Registration to Age-specific Atlas

Subject QSMs

Age Specific Atlas with Deep Grey Nuclei Segmentation

Calculate Avg. QSM within ROIs, Avg. over Subjects

(b)
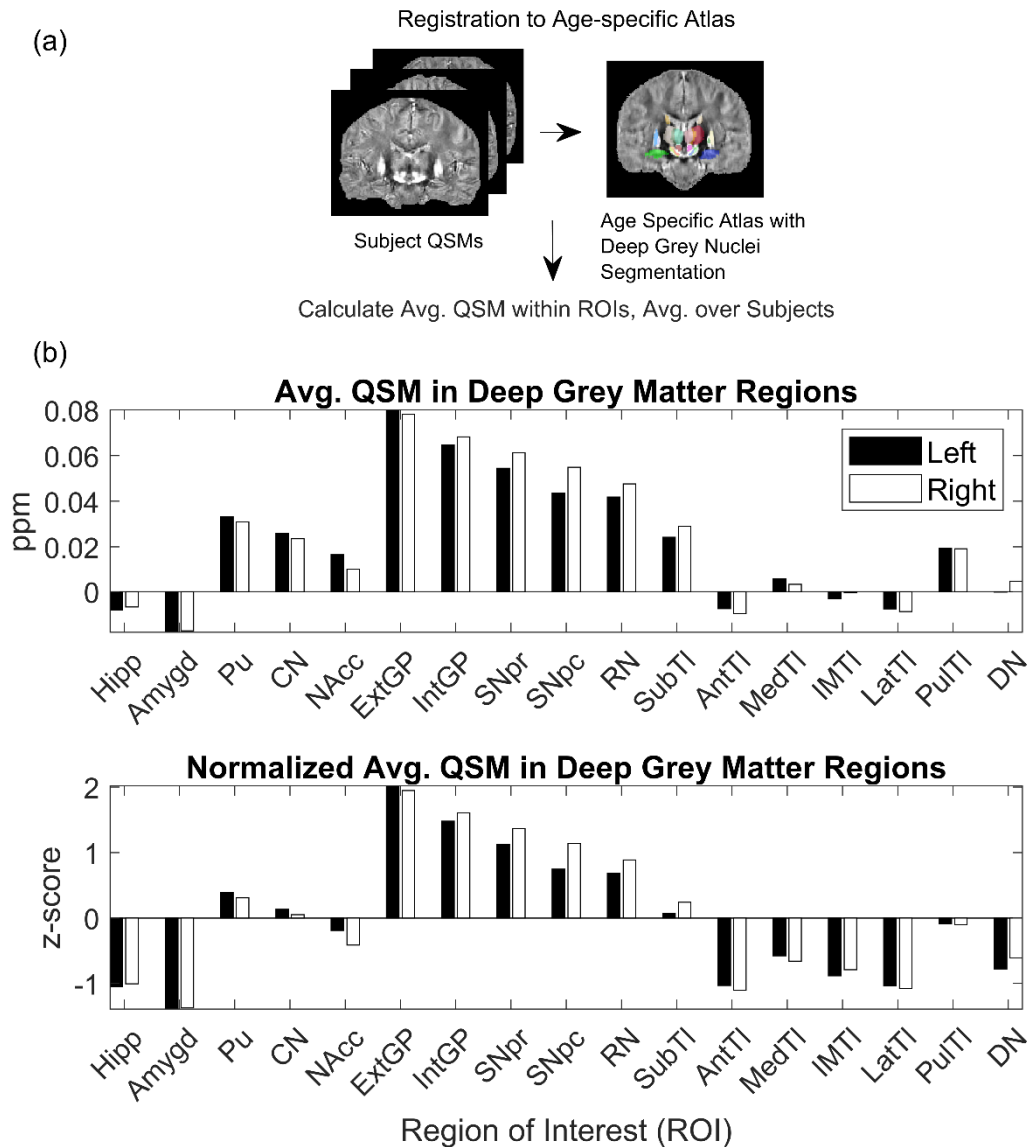
Figure 2.1: **Group QSM analysis pipeline.** (a) QSM registration and preprocessing. Advanced Normalization Tools (ANTs) was used to register nine healthy individual QSM brains, aged 41-49, to the age-specific QSM atlas constructed in Y. Zhang et al. [20]. Following registration, the segmentation associated with the atlas was used to calculate average QSM over all subjects across regions in the deep grey nuclei. (b) Average QSM across deep grey nuclei regions (ppm). (c) Normalized average QSM across deep grey nuclei regions (z-score). Regions of interest on the x-axis correspond to Left (L) and Right (R) Hippocampus (Hipp), Amygdala (Amygd), Putamen (Pu), Caudate Nucleus (CN), Nucleus Accumbens (NAcc), External Globus Pallidus (ExtGP), Internal Globus Pallidus (IntGP), Substantia Nigra pars reticulata (SNpr), Substantia Nigra pars compacta (SNpc), Red Nucleus (RN), Subthalamic nuclei (SubTl), Anterior nuclei of the Thalamus (AntTl), Median nuclei of the Thalamus (MedTl), Intermedullary nuclei of the Thalamus (IMTl), Lateral nuclei of the Thalamus (LatTl), Pulvinar nuclei of the Thalamus (PulTl), and Dentate Nucleus (DN).

	Legend
Abbreviation	**Region of Interest (ROI)**
L Hipp	Hippocampus (left)
R Hipp	Hippocampus (right)
L Amygd	Amygdala (left)
R Amygd	Amygdala (right)
L Pu	Putamen (left)
R Pu	Putamen (right)
L CN	Caudate nucleus (left)
R CN	Caudate nucleus (right)
L NAcc	Nucleus accumbens (left)
R NAcc	Nucleus accumbens (right)
L ExtGP	External globus pallidus (left)
R ExtGP	External globus pallidus (right)
L IntGP	Internal globus pallidus (left)
R IntGP	Internal globus pallidus (right)
L SNpr	Substantia nigra pars reticulata (left)
R SNpr	Substantia nigra pars reticulata (right)
L SNpc	Substantia nigra pars compacta (left)
R SNpc	Substantia nigra pars compacta (right)
L RN	Red nucleus (left)
R RN	Red nucleus (right)
L SubTl	Subthalamic nucleus (left)
R SubTl	Subthalamic nucleus (right)
L AntTl	Anterior nuclei of thalamus (left)
R AntTl	Anterior nuclei of thalamus (right)
L MedTl	Median nuclei of thalamus (left)
R MedTl	Median nuclei of thalamus (right)
L IMTl	Internal medullary lamina of thalamus (left)
R IMTl	Internal medullary lamina of thalamus (right)
L LatTl	Lateral nuclei of thalamus (left)
R LatTl	Lateral nuclei of thalamus (right)
L PulTl	Pulvinar nuclei of thalamus (left)
R PulTl	Pulvinar nuclei of thalamus (right)
L DN	Dentate nucleus (left)
R DN	Dentate nucleus (right)

Table 2.1: **Deep grey nuclei regions.** Regions used in comparative analysis between spatially-localized QSM and gene expression.

We used Advanced Normalization Tools (ANTs) [72] to perform nonlinear registration between each individual QSM and the age-specific QSM atlas constructed using group-wise registration in [20]. The inverse transform generated from the registration was used to warp the segmentation from atlas space back to subject space. The mean signal for each region of interest (ROI) was then calculated by applying the warped mask to the original QSM subject image and averaging all non-zero voxels. This analysis was repeated for all nine subjects, and the mean QSM values across subjects were then normalized using the z-score, yielding the distribution shown in Figure 2.1. The labeled ROIs are also listed in Table 2.1.

2.3.2 DNA microarray survey and post processing

The AHBA is a microarray profile of gene expression values collected from the autopsied normal brains of six individuals, median age 44 [62], [66], [67]. Before inclusion in the dataset, the brain tissue and case profile of each individual was subjected to various screening and evaluation, in order to ensure the integrity of the mRNA and the validity of using the individual

as a normal control, as described in [73]. Dissection of the brains into regions for subsequent processing and microarray analysis resulted in 58,692 gene expression measurements for each of 3,702 distinct tissue samples across the brain [74].

The processing pipeline in Figure 2.2 describes the method of preparation for the gene expression dataset, before it could be used in the regression analysis. This procedure largely follows that described in [75], which provides a thorough evaluation of the methods chosen for each step and the software used to execute these methods. We used Arnatkevičiūtė's software package [75] to perform gene-probe reannotation, probe filtering, and probe selection across all probes and all subjects. We relied on the probe-gene reannotation done by [75] using the National Center for Biotechnology Information (NCBI) human reference genome in March 2018 (Genome Reference Consortium Human Build 38 2013). We excluded probes with expression levels at or below background levels in at least fifty percent of all samples (this information is provided by AHBA for each probe). Of those remaining, we chose a representative probe for each gene by selecting the one with the most consistent pattern of expression across all six brains, as measured by differential stability [77].

Next, we matched samples within deep grey matter regions in the AHBA segmentation to the same regions defined by QSM-based brain atlases [20], [78]. Specifically, we chose Zhang's QSM age-specific atlas segmentation [20]. We chose to match samples by region name, rather than using the provided MNI coordinates of samples, as we focus only on deep grey regions which mostly map one-to-one with regions sampled in the AHBA. Additionally, we found that the MNI coordinates reported by AHBA for sampled regions did not match up to accurate regions in our segmentation, likely due to registration discrepancies in the mapping between subject and MNI space. Some regions in Zhang's atlas segmentation, like the Hippocampus and Amygdala, were found to be subdivided into multiple smaller regions in the AHBA ontology (see Fig. 2.3) [79], [80]. In these cases, we averaged across all smaller regions within the ROI in Zhang's segmentation which encompassed them. Table 2.2 summarizes the results of our assignment between AHBA sample regions and ROIs in Zhang's segmentation.

Finally, normalization was performed for all genes across all matched samples using z-score. This method was chosen due to its simplicity and demonstrated ability to minimize donor-specific effects when normalizing for each subject separately [75]. These z-scores were then averaged across subjects to yield a single set of normalized gene expression values across ROIs defined in Zhang's segmentation.

(a)

(b)
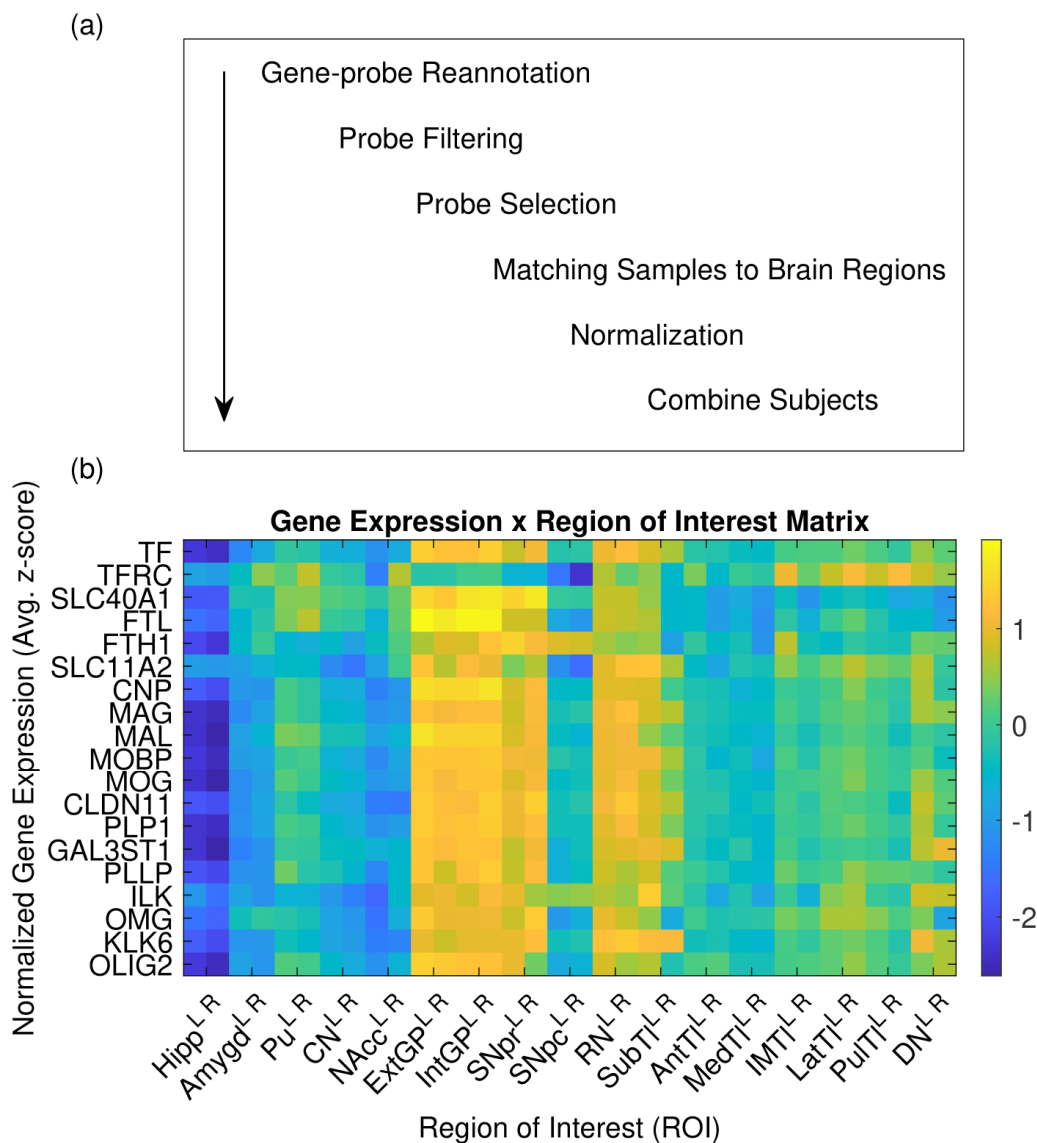
Figure 2.2: **Gene expression analysis pipeline.** (a) Processing pipeline for Allen Human Brain Atlas (AHBA) dataset. We used software developed in Arnatkevičiūtė et al. [75] for gene-probe reannotation, probe filtering, and probe selection of the AHBA dataset [62], [66], [67]. We filtered the probes to exclude those with expression levels at or below background levels in fifty percent or more of all samples. The probe with the highest differential stability across subjects was then selected. AHBA sampled regions were matched to the corresponding ROIs in the QSM atlas segmentation [20]. (b) Expression of genes involved in iron homeostasis and myelination across deep nuclei regions. The gene expression by ROI matrix depicts expression of a subset of genes across these ROIs, following normalization and averaging across subjects. Regions of interest on the x-axis correspond to those listed in Table 2.1.
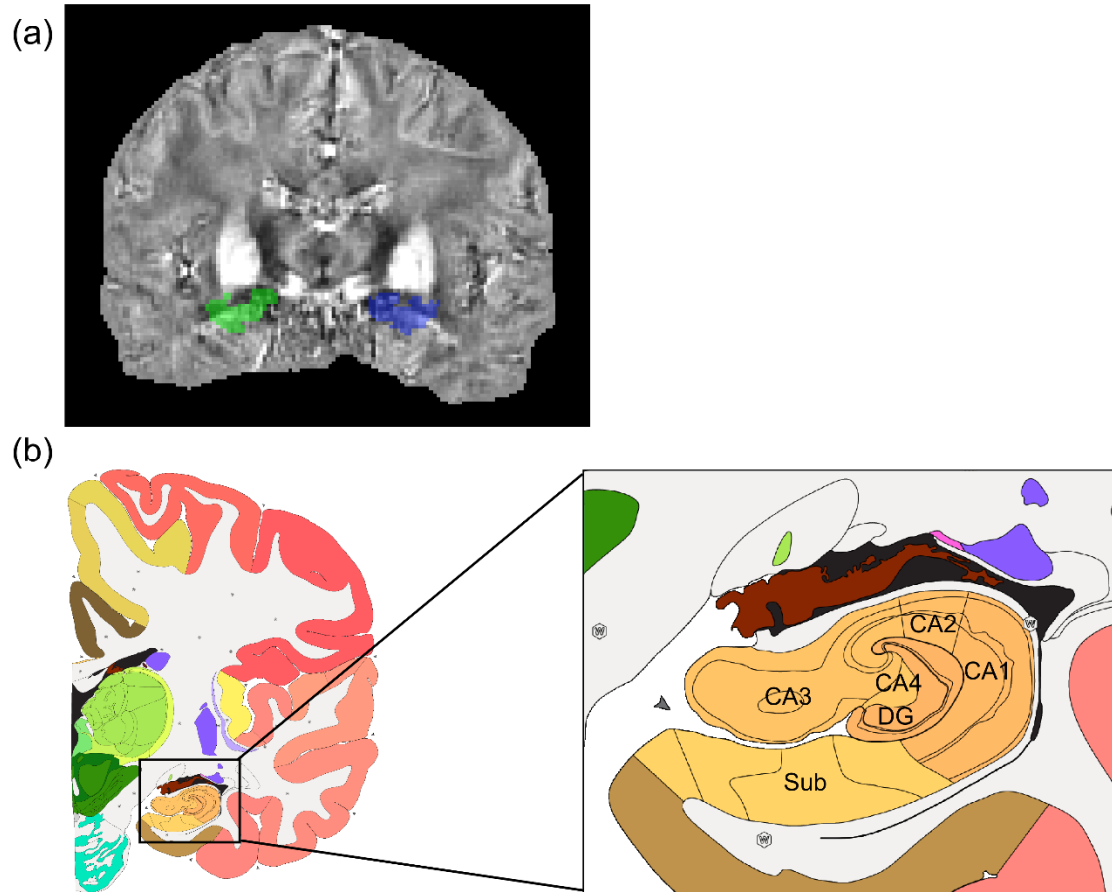
Figure 2.3: **Matching QSM and Allen Human Brain Atlas (AHBA) segmentations.** In some instances, like the hippocampus, we combined multiple AHBA samples if they fell within the same region, as defined in the QSM segmentation. (a) QSM with hippocampus region segmented. (b) AHBA subdivision of hippocampus [79], [80]. Note that the dentate gyrus (DG), CA1 field, CA2 field, CA3 field, CA4 field, and subiculum (Sub) are sampled in the AHBA segmentation, however, we only calculated the average QSM across the entire hippocampus.

ROI	QSM Atlas ROI	Corresponding AHBA ROI(s)
1	Hippocampus (left)	Dentate Gyrus (left), CA1 Field (left), CA2 Field (left), CA3 Field (left), CA4 Field (left), Subiculum (left)
2	Hippocampus (right)	Dentate Gyrus (right), CA1 Field (right), CA2 Field (right), CA3 Field (right), CA4 Field (right), Subiculum (right)
3	Amygdala (left)	Amygdalohippocampal Transition Zone (left), Basolateral Nucleus (left), Basomedial Nucleus (left), Central Nucleus (left), Cortico-medial Group (left), Lateral Nucleus (left)
4	Amygdala (right)	Amygdalohippocampal Transition Zone (right), Basolateral Nucleus (right), Basomedial Nucleus (right), Central Nucleus (right), Cortico-medial Group (right), Lateral Nucleus (right)
5	Putamen (left)	Putamen (left)
6	Putamen (right)	Putamen (right)
7	Caudate Nucleus (left)	Body of Caudate Nucleus (left), Head of Caudate Nucleus (left), Tail of Caudate Nucleus (left)
8	Caudate Nucleus (right)	Body of Caudate Nucleus (right), Head of Caudate Nucleus (right), Tail of Caudate Nucleus (right)
9	Nucleus Accumbens (left)	Nucleus Accumbens (left)
10	Nucleus Accumbens (right)	Nucleus Accumbens (right)
11	External Globus Pallidus (left)	Globus Pallidus, External Segment (left)
12	External Globus Pallidus (right)	Globus Pallidus, External Segment (right)
13	Internal Globus Pallidus (left)	Globus Pallidus, Internal Segment (left)
14	Internal Globus Pallidus (right)	Globus Pallidus, Internal Segment (right)
15	Pars Reticulata of Substantia Nigra (left)	Substantia Nigra, Pars Reticulata (left)
16	Pars Reticulate of Substantia Nigra (right)	Substantia Nigra, Pars Reticulata (right)
17	Pars Compacta of Substantia Nigra (left)	Substantia Nigra, Pars Compacta (left)
18	Pars Compacta of Substantia Nigra (right)	Substantia Nigra, Pars Compacta (right)
19	Red Nucleus (left)	Red Nucleus (left)
20	Red Nucleus (right)	Red Nucleus (right)
21	Subthalamic Nucleus (left)	Subthalamic Nucleus (left)
22	Subthalamic Nucleus (right)	Subthalamic Nucleus (right)
23	Anterior Nuclei of Thalamus (left)	Anterior Group of Nuclei (left)
24	Anterior Nuclei of Thalamus (right)	Anterior Group of Nuclei (right)
25	Median Nuclei of Thalamus (left)	Medial Group of Nuclei (left)
26	Median Nuclei of Thalamus (right)	Medial Group of Nuclei (right)
27	Internal Medullary Lamina of Thalmus (left)	Caudal Group of Intralaminar Nuclei (left), Rostral Group of Intralaminar Nuclei (left)
28	Internal Medullary Lamina of Thalmus (right)	Caudal Group of Intralaminar Nuclei (right), Rostral Group of Intralaminar Nuclei (right)
29	Lateral Nuclei of Thalamus (left)	Lateral Group of Nuclei (left), Medial Geniculate Complex (left)
30	Lateral Nuclei of Thalamus (right)	Lateral Group of Nuclei (right), Medial Geniculate Complex (right)
31	Pulvinar Nuclei of Thalamus (left)	Lateral Group of Nuclei (left), Posterior Group of Nuclei (left)
32	Pulvinar Nuclei of Thalamus (right)	Lateral Group of Nuclei (right), Posterior Group of Nuclei (right)
33	Dentate Nucleus (left)	Dentate Nucleus (left)
34	Dentate Nucleus (right)	Dentate Nucleus (right)

Table 2.2: **Labels for regions of interest (ROIs) in the deep grey nuclei used in our analysis.** The second column corresponds to regions from Zhang's QSM atlas segmentation [20], and the third column corresponds to regions from the Allen Human Brain Atlas (AHBA) [62], [66], [67].

Most ROIs from the two segmentations matched one-to-one, however there were some cases in which ROIs in the AHBA corresponded to subdivisions of an ROI from Zhang's segmentation. In these instances, all sub-regions are reported in the same row of the ROI which contains them.

2.3.3 Linear regression analysis

Following pre-processing using the methods of [75] as described above, we were left with a set of 15,627 gene expression vectors that measure the expression level of a unique gene averaged across all AHBA subjects, for each ROI defined in Zhang's segmentation. Let x_i denote the vector of normalized relative expression of gene i, averaged across all six subjects (avg. z-score), for all deep gray matter ROIs. Element j of x_i is the averaged z-score of gene i measured for ROI j, $j = 1, ..., J$, where J is the total number of ROIs. We define y as the vector of normalized QSM (z-score) averaged across nine separate subjects. Element j of y, denoted y_j, is the averaged QSM z-score across ROI j, $j = 1, ..., J$. For each gene i (from 1 to 15,627), we solved for the vector $\beta_i = [\beta_{0,i}, \quad \beta_{1,i}]^T$ that satisfies the following linear regression problem:

$$y = \begin{bmatrix} 1 & 1 & \cdots & 1 \\ x_{1,i} & x_{2,i} & \cdots & x_{J,i} \end{bmatrix}^T \begin{bmatrix} \beta_{0,i} \\ \beta_{1,i} \end{bmatrix} = [\mathbf{1} \quad x_i]\beta_i = \mathbf{X}_i\beta_i \tag{2.1}$$

After performing all 15,627 linear regressions, we calculated the p-value of the estimated slope using a two-tailed t-test. We then applied multi-comparison correction to the p-values using the Benjamini-Hochberg procedure [81]–[83], which allows us to threshold p-values by setting an upper bound on the false discovery rate (FDR), or the probability of falsely rejecting the null hypothesis. We chose FDR < .05, which is commonly used in microarray studies. We justify this method of multi-comparison correction in our case, since we are interested in identifying genes that potentially have a relationship to the QSM signal, and this choice provides vastly more statistical power than the more conservative Bonferroni correction, which instead controls the family-wise error rate (the probability of having at least one false positive). However, we also report results using the Bonferroni correction, and we use the genes passing this threshold to perform partial least-squares regression (PLSR) in order to examine their relative contributions. Since the QSM signal is known to be largely influenced from paramagnetic and diamagnetic species like iron-loaded ferritin and myelin, we chose to focus on only iron and myelination related genes (comprising a set of 23 genes identified from literature and listed in Tables 2.3 and 2.4). Of these, we determined whether any were significantly related to QSM following the Bonferroni correction. We chose the Bonferroni correction for this thresholding rather than 5% FDR as we are limited by a small sample size for the PLSR, and the Bonferroni correction is a more conservative criterion.

In PLSR, we find a representation for both the predictor variables, $\mathbf{X}$, and the response variable, $\boldsymbol{y}$, in terms of components $\boldsymbol{z}_k, k = 1, \dots, n$, where n is the total number of PLS components [84]–[86]. $\mathbf{X}$ is a matrix of gene expression z-scores for a set of I genes across J deep grey matter ROIs, such that column i of $\mathbf{X}$ is the vector of normalized expression of gene i, $\boldsymbol{x}_i$. We include a first column of all ones to solve for a y-intercept term in the PLSR. As before, $\boldsymbol{y}$ is a vector of normalized average QSM z-scores for all ROIs. This representation is designed to best explain the covariance of $\mathbf{X}$ and $\boldsymbol{y}$, rather than focusing on the variance of $\mathbf{X}$ alone as in other methods, like principal component analysis regression. The set-up of the PLSR problem is as follows:

$$\mathbf{X} = [\mathbf{1} \quad \boldsymbol{x}_1 \quad \cdots \quad \boldsymbol{x}_I] \tag{2.2}$$

$$\mathbf{X} = [\boldsymbol{z}_1 \quad \cdots \quad \boldsymbol{z}_n] \begin{bmatrix} \boldsymbol{v}_1^T \\ \vdots \\ \boldsymbol{v}_n^T \end{bmatrix} + \mathbf{E} = \mathbf{Z}\mathbf{V}^T + \mathbf{E} \tag{2.3}$$

$$\boldsymbol{y} = \mathbf{Z}\boldsymbol{u} + \boldsymbol{e} \tag{2.4}$$

$\mathbf{V}^T$ is a loading matrix that defines the predictors in terms of the PLS components that compose matrix $\mathbf{Z}$. Similarly, $\boldsymbol{u}$ is a vector of coefficients that relates $\mathbf{Z}$ to the response variable, $\boldsymbol{y}$. $\mathbf{E}$ and $\boldsymbol{e}$ are both residual terms. We can rearrange Equation 2.3 to express the PLS components in terms of the predictor variables. Let $\mathbf{W}$ be a matrix of PLS weights such that $\mathbf{Z} = \mathbf{X}\mathbf{W}$. Substituting the result into Equation 2.4 yields a representation of $\boldsymbol{y}$ in terms of the original predictors:

$$\mathbf{Z} = \mathbf{X}\mathbf{W} \tag{2.5}$$

$$\boldsymbol{y} = \mathbf{X}\mathbf{W}\boldsymbol{u} + \boldsymbol{e} = \mathbf{X}\boldsymbol{\beta} + \boldsymbol{e} \tag{2.6}$$

We used cross-validation to choose the number of components needed for the PLSR, ensuring the model is significantly predictive without over-fitting [86], [87]. For each model, we calculated the root mean squared error (RMSE) using a leave-one-out cross validation and using all samples. We chose the model yielding the smallest cross validation RMSE (RMSE-CV) that also wasn't more than 20% higher than RMSE, which would indicate overfitting [86]. Finally, we used the jack-knife bootstrap technique to calculate 95% confidence intervals on the PLS coefficients [86].

Iron Gene Set	
Gene	**Protein**
TF	Transferrin (Tf)
TFRC	Transferrin receptor (TFR)
SLC11A2	Divalent metal transporter 1 (DTM1)
FTL	Light-chain ferritin (L-Ft)
FTH1	Heavy-chain ferritin (H-Ft)
SLC40A1	Ferroportin (Fpn)

Table 2.3: **Full set of iron homeostasis genes used in linear regression analysis.** The regression results were reported for all of these genes. The abbreviation for each gene and the corresponding protein encoded by the gene are listed in the table above.

Myelination Gene Set	
Gene	**Protein**
CLDN11	Claudin11
GAL3ST1	Galactose-3-O-sulfotransferase-1
MAG	Myelin-associated glycoprotein
OMG	Oligodendrocyte myelin glycoprotein
MBP	Myelin basic protein
CNP	2',3'-cyclic nucleotide 3'-phosphodiesterase
ILK	Integrin-linked kinase
MAL	Myelin and lymphocyte protein
PLLP	Proteolipid plasmolipin
NRG1	Neuregulin 1
EIF2AK3	Eukaryotic translation initiation factor 2 alpha kinase 3
KLK6	Kallikrein-6
PLP1	Proteolipid protein
POU3F1	POU domain, class 3, transcription factor 1
OLIG2	Oligodendrocyte transcription factor 2
MOBP	Myelin-associated oligodendrocytic basic protein
MOG	Myelin oligodendrocyte glycoprotein

Table 2.4: **Full set of myelination related genes used in linear regression analysis**. The regression results were reported only for myelin genes significantly correlated with QSM, following the Benjamini-Hochberg procedure. The abbreviation for each gene and the corresponding protein encoded by the gene are listed in the table above.

2.4   Comparison of QSM and Expression of Genes Involved in Iron Transport and Myelination: Results

Figure 2.4: **Multiple regression of QSM vs. iron related genes**. Linear regression of QSM vs. normalized expression of (a) TF, (b) TFRC, (c) SLC40A1, (d) FTH1, (e) FTL, and (f) SLC11A2 in the deep grey nuclei regions. These refer to transferrin (TF), transferrin receptor (TFRC), ferroportin (SLC40A1), ferritin heavy chain (FTH1), ferritin light chain (FTL), and divalent metal transporter 1 (SLC11A2). QSM and gene expression were averaged across subjects. Regions of interest in the deep grey nuclei are listed in Table 2.1. See Fig. 2.6a-f for the results of linear regression with the iron gene set performed for each subject separately.

2.4.1 Linear Regression with Iron Transport and Storage Genes

We first focus on the results of the multiple linear regressions for genes encoding a set of proteins involved in iron homeostasis: Tf, TFR, Fpn, heavy-chain Ft (H-Ft), light-chain Ft (L-Ft), and DMT1. Figure 2.4 shows the results of the linear regression for each of the genes encoding these proteins, which are TF, TFRC, SLC40A1, FTH1, FTL, and SLC11A2, respectively. After conducting a two-tailed t-test (32 degrees of freedom), the regression models for Tf, H-Ft, L-Ft, Fpn, and DMT1 were found to be significant following the Benjamini-Hochberg procedure.

Among those significant, the L-Ft model had the smallest p-value, 1.32e-9, and then H-ferritin with a p-value of 8.66e-7. In all the significant cases, the correlation with the QSM signal is positive, and the value of the slope ranges from .46 to .85 (Fig. 2.4). TFR did not yield a regression model with a significant p-value following the Benjamini-Hochberg procedure, which is explained by the subject-level analysis. TFR shows much higher variability in the slopes and p-values across subjects, which ranged from 6.20e-3 to 4.52e-1 and -.53 to .31, respectively (Fig 2.6b). Conversely, Tf, H-Ft, L-Ft, Fpn, and DMT1 show good agreement in the linear regression on the subject level, with p-values ranging from 4.53e-5 to 1.81e-2 for Tf, from 4.84e-7 to 9.62e-4 for H-Ft, from 2.36e-8 to 2.07e-4 for L-Ft, from 4.33e-4 to 2.48e-1 for Fpn, and from 3.43e-2 to 1.93e-1 for DMT1. Additionally, the slope of the regression line fitted for each subject was found to range from .58 to .69 for Tf, from .58 to .81 for H-Ft, from .75 to .88 for L-Ft, from .30 to .76 for Fpn, and from .23 to .52 for DMT1. The results of the subject-level analysis are provided in Fig. 2.6a-f.

2.4.2 Linear Regression with Myelination Genes

We also report the results of the multiple linear regressions for a set of 17 genes implicated in myelination: CLDN11, GAL3ST1, MAG, OMG, MBP, CNP, ILK, MAL, PLLP, NRG1, EIF2AK3, KLK6, PLP1, POU3F1, OLIG2, MOBP, MOG [58]. The proteins encoded by these genes are provided in Table 2.4. We again performed two-tailed t-tests (32 df) for each regression. Of these regression models, 13 were found to be significant following the Benjamini-Hochberg procedure, including CNP, OLIG2, MAL, MOBP, MOG, CLDN11, PLP1, GAL3ST1, PLLP, ILK, OMG, KLK6, and MAG as shown in Figures 2.5a-m. The MAL model had the smallest p-value, 9.48e-7, and then CNP and MOBP with p-values of 3.40e-6 and 4.37e-6, respectively. All the significant regression models show a positive correlation between gene expression and QSM, with slopes varying from .55 to .76. The subject-level regression results are also reported for each model in Fig. 2.6g-s, and these show that regression models for CNP, OLIG2, MAL, MOBP, MOG, CLDN11, PLP1, GAL3ST1, PLLP, ILK, OMG, KLK6, and MAG are similar across subjects. The slopes for all of these range from .10 to .77 and the p-values range from 8.56e-6 to 5.91e-1.

2.4.3 Partial Least Squares Regression with Iron and Myelin Genes

Finally, we performed PLSR using the genes from both the iron and myelin sets found to have expression significantly correlated with QSM following Bonferroni correction. These genes include FTL, FTH1, and MAL. Cross validation supported using a two-component model, as this was found to achieve the optimal RMSE-CV and RMSE. The coefficients of the two-component PLSR model are shown in Figure 2.7a, and the cross validation for the selection of this model is shown in Figure 2.7b. The coefficients range from -.16 to .95, however, only FTL has a 95% confidence interval that doesn't include zero. FTL also has the highest positive coefficient.
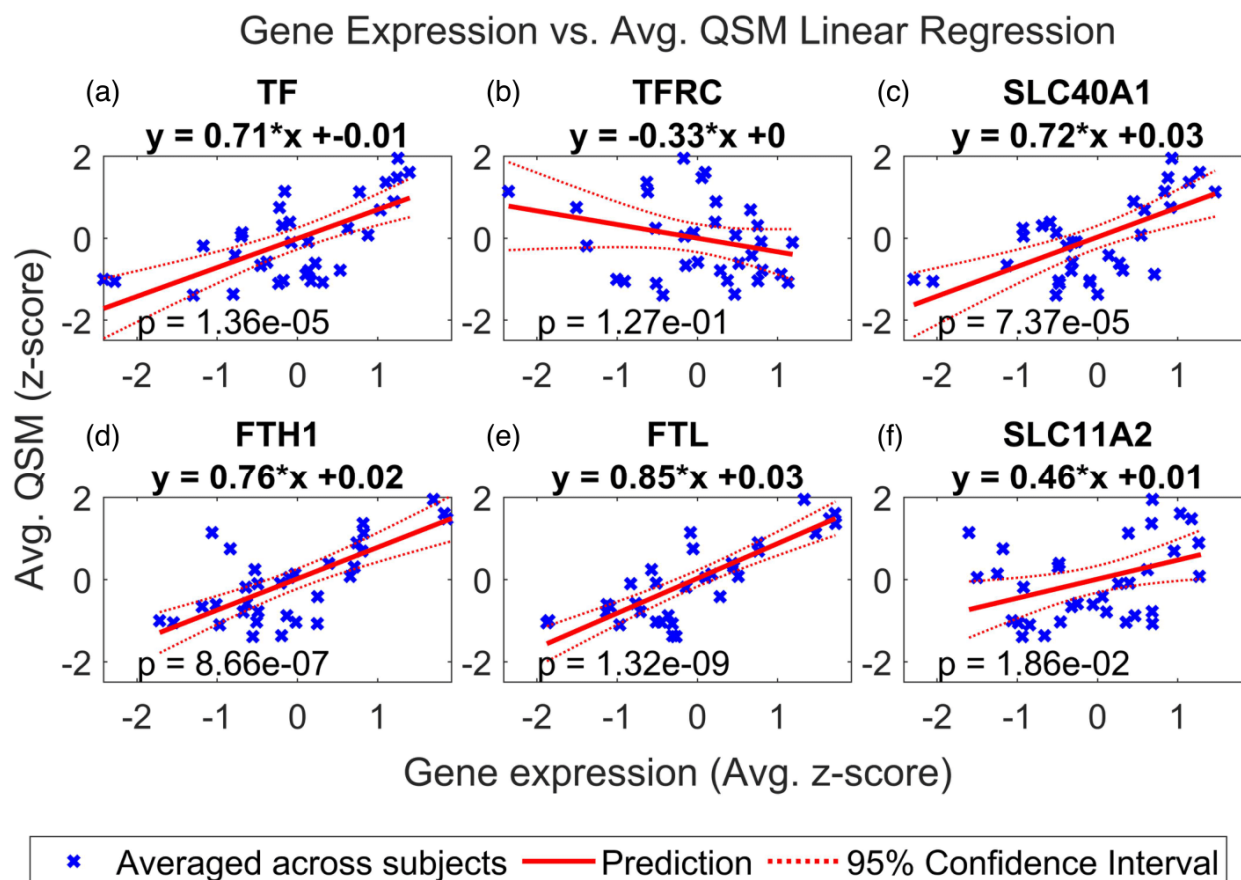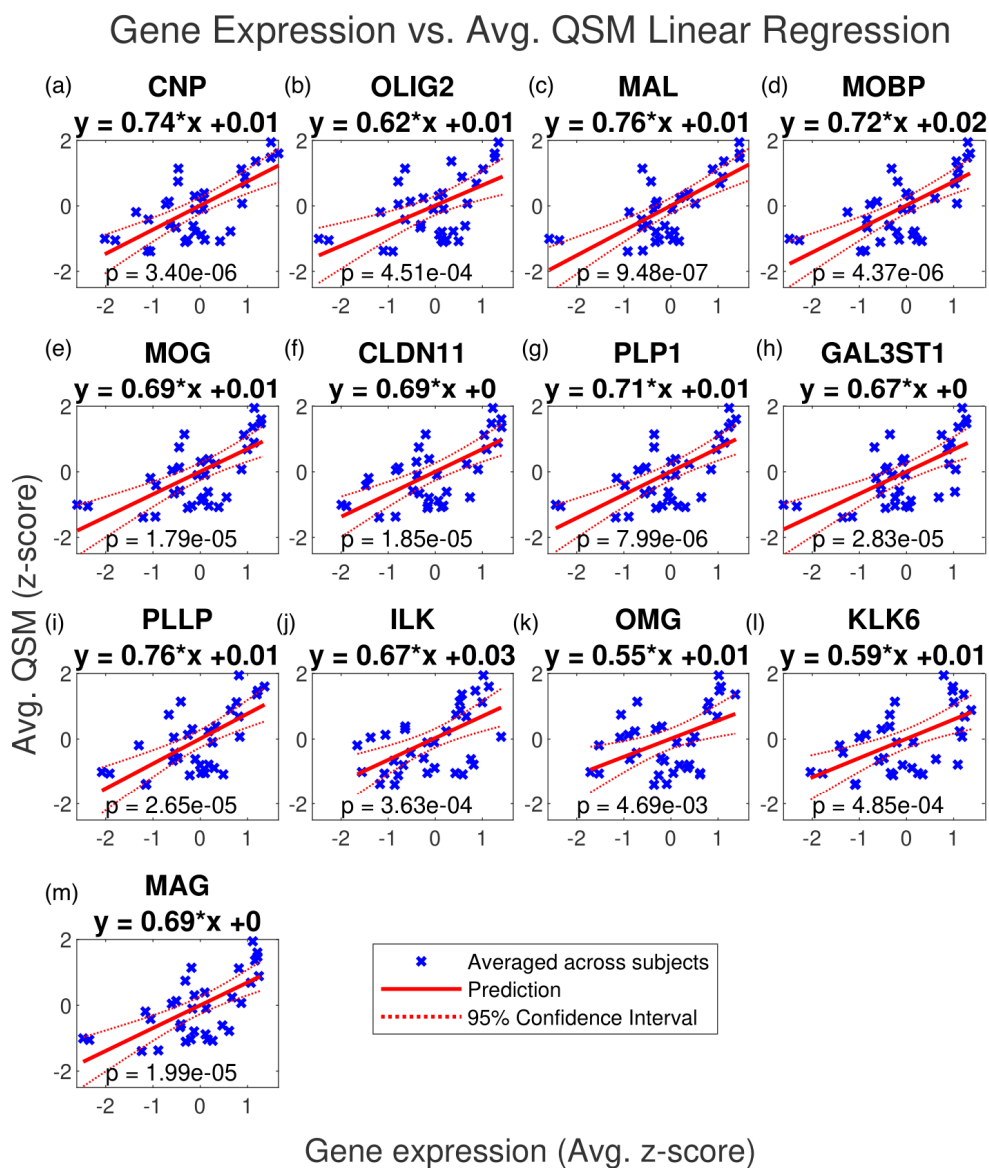
Figure 2.5: **Multiple regression of QSM vs. myelin related genes**. Linear regression of QSM vs. normalized expression of (a) CNP, (b) OLIG2, (c) MAL, (d) MOBP, (e) MOG, (f) CLDN11, (g) PLP1, (h) GAL3ST1, (i) PLLP, (j) ILK, (k) OMG, (l) KLK6 and (m) MAG in the deep grey nuclei regions. QSM and gene expression were averaged across subjects. Regions of interest in the deep grey nuclei are listed in Table 2.1. Only significant results are shown. These include 2',3'-cyclic nucleotide 3'-phosphodiesterase (CNP), oligodendrocyte transcription factor 2 (OLIG2), myelin and lymphocyte protein (MAL), myelin-associated oligodendrocytic basic protein (MOBP), myelin oligodendrocyte glycoprotein (MOG), claudin-11 (CLDN11), proteolipid protein (PLP1), galactose-3-O-sulfotransferase-1 (GAL3ST1), proteolipid plasmolipin (PLLP), integrin-linked kinase (ILK), oligodendrocyte-myelin glycoprotein (OMG), kallikrein-related peptidase 6 (KLK6) and myelin-associated glycoprotein (MAG). See Fig. 2.6g-s for the results of linear regression with the myelin gene set performed for each subject separately.

(a) **TF Regression**

Subject	Slope	P-Value
1	0.65	4.53E-05
2	0.59	2.61E-04
3	0.66	3.70E-03
4	0.58	1.81E-02
5	0.63	6.26E-03
6	0.69	2.21E-03

(b) **TFRC Regression**

Subject	Slope	P-Value
1	-0.14	4.41E-01
2	-0.46	6.20E-03
3	0.31	2.18E-01
4	0.22	4.18E-01
5	-0.53	2.79E-02
6	-0.20	4.52E-01

(c) **SLC11A2 Regression**

Subject	Slope	P-Value
1	0.23	1.93E-01
2	0.31	7.70E-02
3	0.43	8.86E-02
4	0.40	1.25E-01
5	0.39	1.20E-01
6	0.52	3.43E-02

(d) **SLC40A1 Regression**

Subject	Slope	P-Value
1	0.44	1.02E-02
2	0.57	4.33E-04
3	0.65	4.94E-03
4	0.76	5.98E-04
5	0.30	2.48E-01
6	0.56	1.85E-02

(e) **FTH1 Regression**

Subject	Slope	P-Value
1	0.75	4.84E-07
2	0.58	3.30E-04
3	0.75	4.66E-04
4	0.74	9.60E-04
5	0.73	9.62E-04
6	0.81	9.20E-05

(f) **FTL Regression**

Subject	Slope	P-Value
1	0.80	2.36E-08
2	0.75	4.04E-07
3	0.88	3.30E-06
4	0.87	1.30E-05
5	0.78	2.07E-04
6	0.83	4.33E-05

(g) **CNP Regression**

Subject	Slope	P-Value
1	0.62	1.24E-04
2	0.63	7.08E-05
3	0.70	1.92E-03
4	0.58	1.86E-02
5	0.68	2.50E-03
6	0.71	1.54E-03

(h) **OLIG2 Regression**

Subject	Slope	P-Value
1	0.27	1.30E-01
2	0.54	8.74E-04
3	0.73	9.24E-04
4	0.60	1.46E-02
5	0.64	5.21E-03
6	0.70	1.77E-03

(i) **MAL Regression**

Subject	Slope	P-Value
1	0.66	2.69E-05
2	0.66	1.90E-05
3	0.73	9.13E-04
4	0.74	1.13E-03
5	0.75	5.99E-04
6	0.77	3.20E-04

(j) **MOBP Regression**

Subject	Slope	P-Value
1	0.69	8.56E-06
2	0.64	4.76E-05
3	0.66	4.20E-03
4	0.62	1.06E-02
5	0.62	8.43E-03
6	0.67	3.25E-03

(k) **MOG Regression**

Subject	Slope	P-Value
1	0.59	2.70E-04
2	0.60	1.84E-04
3	0.66	4.20E-03
4	0.59	1.69E-02
5	0.68	2.73E-03
6	0.73	8.13E-04

(l) **CLDN11 Regression**

Subject	Slope	P-Value
1	0.61	1.68E-04
2	0.61	1.42E-04
3	0.60	1.11E-02
4	0.57	2.10E-02
5	0.65	4.94E-03
6	0.67	3.54E-03

(m) **PLP1 Regression**

Subject	Slope	P-Value
1	0.65	4.03E-05
2	0.62	8.72E-05
3	0.69	2.36E-03
4	0.57	2.19E-02
5	0.66	4.18E-03
6	0.70	1.91E-03

(n) **GAL3ST1 Regression**

Subject	Slope	P-Value
1	0.61	1.76E-04
2	0.58	2.81E-04
3	0.57	1.70E-02
4	0.64	7.19E-03
5	0.62	7.41E-03
6	0.66	4.18E-03

(o) **PLLP Regression**

Subject	Slope	P-Value
1	0.42	1.49E-02
2	0.52	1.73E-03
3	0.56	1.85E-02
4	0.58	1.98E-02
5	0.65	4.57E-03
6	0.77	3.21E-04

(p) **ILK Regression**

Subject	Slope	P-Value
1	0.28	1.15E-01
2	0.53	1.22E-03
3	0.68	2.51E-03
4	0.65	6.37E-03
5	0.17	5.13E-01
6	0.50	4.33E-02

(q) **OMG Regression**

Subject	Slope	P-Value
1	0.10	5.91E-01
2	0.47	5.35E-03
3	0.45	6.76E-02
4	0.50	5.07E-02
5	0.42	9.65E-02
6	0.59	1.26E-02

(r) **KLK6 Regression**

Subject	Slope	P-Value
1	0.48	4.81E-03
2	0.55	7.88E-04
3	0.53	2.84E-02
4	0.48	5.83E-02
5	0.53	3.01E-02
6	0.55	2.30E-02

(s) **MAG Regression**

| Subject	Slope	P-Value
1	0.57	5.16E-04
2	0.63	7.00E-05
3	0.63	6.90E-03
4	0.61	1.15E-02
5	0.64	5.85E-03
6	0.68	2.74E-03

Figure 2.6: **Subject-level multiple regression of QSM vs. iron and myelin related genes**. Linear regression of QSM vs. normalized expression of (a) TF, (b) TFRC, (c) SLC11A2, (d) SLC40A1, (e) FTH1, (f) FTL, (g) CNP, (h) OLIG2, (i) MAL, (j) MOBP, (k) MOG, (l) CLDN11, (m) PLP1, (n) GAL3ST1, (o) PLLP, (p) ILK, (q) OMG, (r) KLK6 and (s) MAG in the deep grey nuclei regions. These refer to transferrin (TF), transferrin receptor (TFRC), divalent metal transporter 1 (SLC11A2), ferroportin (SLC40A1), ferritin heavy chain (FTH1), ferritin light chain (FTL), 2',3'-cyclic nucleotide 3'-phosphodiesterase (CNP), oligodendrocyte transcription factor 2 (OLIG2), myelin and lymphocyte protein (MAL), myelin-associated oligodendrocytic basic protein (MOBP), myelin oligodendrocyte glycoprotein (MOG), claudin-11 (CLDN11), proteolipid protein (PLP1), galactose-3-O-sulfotransferase-1 (GAL3ST1), proteolipid plasmolipin (PLLP), integrin-linked kinase (ILK), oligodendrocyte-myelin glycoprotein (OMG), kallikrein-related peptidase 6 (KLK6) and myelin-associated glycoprotein (MAG). Regressions were performed for each subject in the Allen Human Brain Atlas (AHBA). QSM was averaged across subjects and across regions. Regions of interest in the deep grey nuclei are listed in Table 2.1.
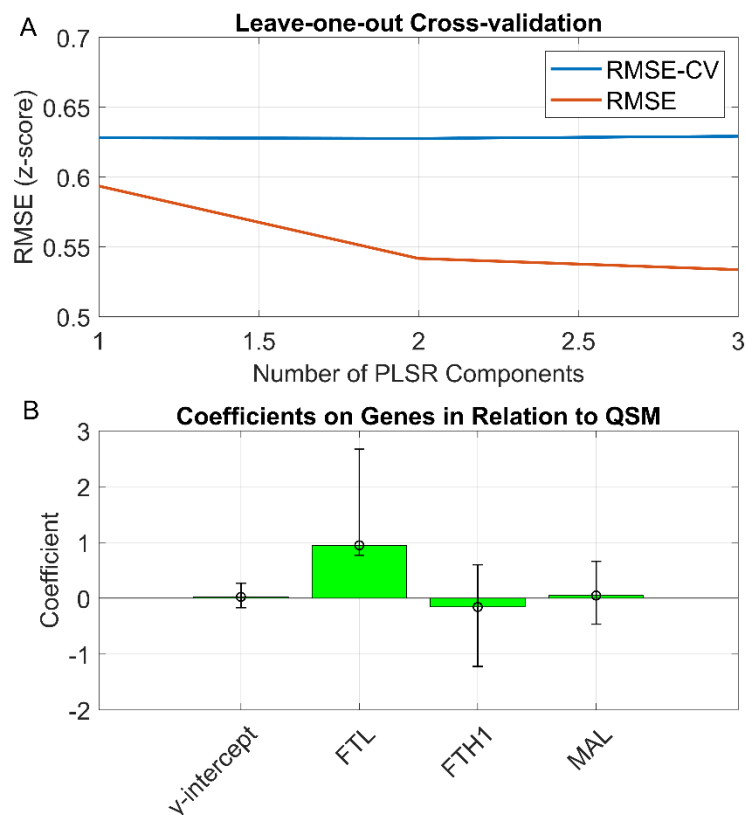
Figure 2.7: **Two-component partial least squares regression (PLSR) of QSM vs. a set of iron and myelin gene expression vectors.** (a) Coefficients of the 2-component PLSR between QSM and the iron and myelin gene set across deep grey nuclei regions. The genes are those from both the iron and myelin set that were found to have expression significantly correlated with QSM following the Bonferroni correction, including ferritin light chain (FTL), ferritin heavy chain (FTH1) and myelin and lymphocyte protein (MAL). 95% confidence intervals were calculated for the regression coefficients using the jack-knife procedure. (b) Root mean squared error (RMSE) calculated for all possible PLSR models, using all samples (RMSE) versus leave-one-out cross-validation (RMSE-CV). The model yielding the smallest RMSE-CV that also wasn't more than 20% higher than RMSE was chosen for the PLSR. This was the two-component model, as indicated on the plot.

2.5   Discussion

Our analysis revealed a spatial congruent relationship between tissue magnetic susceptibility and gene expression in the brain. We found significant positive correlations between expression of genes encoding both light and heavy chain Ft and several iron transporters, and the QSM signal across these regions. Interestingly, we also observed a positive correlation between QSM and several genes involved in myelination, expressed by oligodendrocytes. This reflects that the iron-loaded Ft is likely localized to mature oligodendrocytes. Indeed, oligodendrocytes have been found to outnumber neurons in regions of high iron, like the basal ganglia, and iron is localized mainly to oligodendrocytes and the neuropil within these regions [88], [89]. In addition, oligodendrocytes are known to require iron in large amounts for myelination [3], [9]. This iron can be acquired by oligodendrocytes via the H-ferritin receptor [56], [90].

2.5.1 Iron and myelin related genes are strongly correlated with QSM

We use PLSR in order to assess the relative contributions of genes relevant to iron homeostasis and myelination that were found to be significantly correlated with QSM, following Bonferroni correction. Our results confirm that Ft dominates the QSM signal over the contributions of other molecules. Interestingly, the PLSR analysis shows unequal contributions from H-Ft and L-Ft. These are known to exhibit different roles in iron homeostasis and to be differentially distributed across cell types and brain regions, with H-Ft largely out-numbering L-Ft [8]. In addition to serving as an iron transporter, H-Ft has the ferroxidase ability, which converts the reactive ferrous iron to more stable ferric iron [91]. L-Ft is more important for the formation of the iron core, which is what generates the molecule's strong paramagnetic susceptibility signal [91], [92]. Additionally, L-Ft is present in oligodendrocytes, supporting the hypothesis of their role in iron storage [93]. This is consistent with the results of our PLSR, which predicts a higher contribution from L-Ft than H-Ft.

       The 95% confidence intervals calculated using the jack-knife indicate that the PLSR coefficients for FTH1 and MAL may not be significant. We know that the major determinant of

the QSM signal is magnetic susceptibility. Although MAL and other myelination genes show a positive correlation with QSM in the deep grey nuclei, which we know to have positive susceptibility, the proteins encoded by these genes actually make up the myelin sheath, which itself has a negative susceptibility. It is possible these genes may be expressed by oligodendrocytes, either containing iron-loaded Ft or present in the same voxel as other iron-loaded cells. If the second case, there is a strong likelihood that oligodendrocytes are involved in the transport of iron either to or from these other iron-loaded cells. The correlation with QSM is gene expression, which reflects oligodendrocyte activity, not necessarily protein content.

2.5.2 Iron transporters are indicated by QSM

The positive correlation of QSM with the expression of Fpn, the only known iron exporter, suggests that the QSM signal reflects not only iron storage, but active transport. More specifically, this result indicates that Fpn must be expressed on cells loaded with iron, or at least, on cells co-localizing with iron-loaded cells within voxels of the QSM image. Oligodendrocytes, neurons, microglia, and astrocytes all express Fpn, however, oligodendrocytes accumulate iron in significantly larger amounts than any other cell [37], [94]. Microglia and astrocytes are also known to express Ft, particularly the light chain subunit which is associated with iron storage, and there is evidence that both cells may release iron loaded H-Ft for use by oligodendrocytes early in development [90], [95]. Astrocytes are also implicated in providing growth factors necessary for maturation of oligodendrocyte precursor cells [96], [97]. Although the density of microglia is particularly high in the basal ganglia, even accounting for 12% of cells in the substantia nigra of the adult mouse brain [98], microglia show significant variation in their transcriptome by brain region, particularly among the deep grey nuclei [99], [100]. Therefore, it seems unlikely that the positive correlation between gene expression of iron transporters and QSM across deep grey nuclei could be due to these cells. In fact, microglial cell number in the deep grey nuclei is not correlated with oligodendrocyte density, but rather, that of astrocytes [99]. Astrocytes, despite expressing TFR, DMT1, Fpn, and Ft, maintain a low level of cellular iron [9]. This evidence, taken together, again points to oligodendrocytes as the source of the QSM signal.

The positive correlation of Tf with QSM can also be explained by the presence of oligodendrocytes. Tf is a well-known marker of oligodendrocytes, as it is secreted by them and most Tf in the brain is thought to originate from these cells [101]–[103]. Despite this, mature oligodendrocytes don't express TFR, instead likely getting most of their iron via H-Ft [104]. In this context, the lack of correlation between TFR expression and the QSM signal makes sense and is consistent with the known distribution of TFR in the brain [104]. Although TFR is expressed in central neurons, the distribution, found from histology studies, doesn't reflect areas of high iron concentration [22], [104]. This supports the theory of H-Ft as the major route of iron transport for mature oligodendrocytes [56]. Indeed, receptors for H-Ft, specifically T-cell immunoglobulin and mucin domain (Tim-1), exist on myelinating oligodendrocytes [55], and these cells are known to contain the vast majority of iron in the brain [8]. This is likely because

iron is required in high concentrations for the synthesis of myelin [3], [9]. Additionally, it has been shown that neurons in regions of high TFR expression project to regions with high iron [104], [105]. Because of this, [106] have explored the possibility of axonal transport of iron between such regions and have identified two different pathways. The results of our study support the idea that the role of TFR is mainly one of iron uptake from the blood brain barrier, and that further iron transport between regions is responsible for iron accumulation in various deep grey nuclei.

With this information, it seems likely that TFR expression mainly reflects influx of iron across the BBB rather than iron transport between brain regions. This is supported by evidence showing that iron in the developing brain is first seen in oligodendrocyte progenitor cells near blood vessels, only later moving to sites of myelination [90]. DMT1 is another potential route of iron transport, found in both the glia and neurons, however it is not specific to iron [36]. Despite this, we found a significant positive correlation (FDR 5%) between DMT1 gene expression and QSM in the deep grey nuclei. Unlike TFR, DMT1 has been found to be present in higher amounts in the striatum than in the cortex in the rat brain, however, throughout the entire brain it is localized mainly to BMECs and ependymal cells [36], [107]. Within BMECs, DMT1 and TFR have been shown to co-localize, and DMT1 has also been found on the end-feet of astrocytes, which interface with BMECs [107]. This points to DMT1 being involved in the process of iron uptake, along with TFR. The presence of DMT1 in ependymal cells may indicate it plays a role in iron exchange between the brain interstitial fluid and the ventricles [107]. Interestingly, [108], [109] have shown that DMT1 also co-localizes with TFR in oligodendrocyte progenitor cells, and that both of these are upregulated during the beginning stages of oligodendrocyte progenitor cell maturation. Additionally, DMT1 and TFR appear to be required for the iron accumulation and morphological development of these cells, both of which are precursors to myelination [108], [109]. However, there is evidence that DMT1 is necessary for normal myelination even in the adult brain, while TFR may not influence mature oligodendrocytes or myelination [108], [109]. Therefore, it is possible that high expression of TFR is more reflective of oligodendrocyte progenitor cells, rather than mature, myelinating oligodendrocytes, which seem to be more relevant to the QSM signal, as discussed next.

2.5.3 QSM may reflect presence of mature oligodendrocytes

The myelination genes found to be significantly positively correlated with QSM at 5% FDR are markers of mature oligodendrocytes [58]. These include CNP, MAG, MAL, MOBP, MOG, CLDN11, PLP1, GAL3ST1, PLLP, ILK, OMG, KLK6, and OLIG2. However, when using the Bonferroni correction only MAL remains significantly correlated with QSM. Oligodendrocytes are mitotic cells, starting as simple, migratory cells then moving to various regions of the brain and changing to become morphologically more complex [7], [59]. This involves extending processes from the soma, down-regulating TFR, and accumulating iron in large amounts, potentially via the H-Ft receptor [56]. Various genes are expressed sequentially by oligodendrocytes to facilitate this process of development [59]. CNP encodes a protein that,

among other functions, is implicated in the formation of process outgrowths in oligodendrocyte progenitor cells [110]. It is also a major constituent of the myelin sheath, along with myelin basic protein (MBP) and PLP1 [110]. These proteins make up the largest structural contribution to the myelin sheath, and are expressed early on in myelination, along with ILK and OLIG2 which are required for oligodendrocyte maturation [111]–[113]. MAG is also expressed early in the process of myelination and continues to be expressed following oligodendrocyte maturation, indicating a potential role in myelin maintenance [114]. KLK6 may be involved in regulating oligodendrocyte differentiation [115]. PLLP is implicated in myelin synthesis, as well as remyelination, and has been found to co-localize with MAG [116], [117].

MAL, MOBP, MOG, and OMG are expressed later, and have various roles important for the compaction and stabilization of myelin [112], [118]–[120]. CLDN11 is essential for the formation of tight junctions between layers of the myelin sheath, which are necessary for the fast transmission of electrical signals down the axon [121], [122]. GAL3ST1 encodes an enzyme required for the maintenance of proper myelin sheath structure [123], [124]. All together, these genes typically reflect the presence of myelinating oligodendrocytes, however, they are also known to be expressed, but not translated, in nonmyelinating perineuronal oligodendrocytes [7]. These are implicated in remyelination and may be involved in mediating iron transport or other trophic factors for use by neurons, as they have much higher metabolic requirements than neurons despite not producing myelin [125], [126]. While biologically it is unclear why MAL is more significant than the other myelination genes in our statistical analysis, it is interesting to note that MAL is one of the last genes to be expressed in myelination and is located within the compact myelin [112]. Nonetheless, the result is consistent with the fact that MAL has the smallest p-value among all myelination genes as found in the multiple regression analyses.

2.6   Limitations

Our analysis is limited by a small subject pool, and the reliance upon two separate subject pools for the QSM and gene expression datasets. However, in the brain, many genes are known to exhibit differential expression throughout regions [62], and this specific expression pattern has been found to be highly conserved among individuals, with the vast majority of genes reflecting consistent spatially-determined patterns of expression between individual brains [127]. Differences between subjects, particularly age and post-mortem tissue collection in the formation of the AHBA dataset, may explain some discrepancies in the gene expression data. Only two out of the six subjects had regions sampled from both hemispheres of the brain, rather than just the left hemisphere. Notably, myelin basic protein (MBP) was not found to be significantly correlated with QSM. MBP is usually expressed by mature oligodendrocytes, around the time as other genes like CNP and PLP1, and it is typically used as a marker of oligodendrocytes reaching the last developmental stage [110], [112]. The reason for MBP's absence is unclear, potentially it is a result of differences in tissue collection between subjects, or it may be a result of the probe

chosen to measure MBP in the AHBA dataset. MBP is known to be a long gene with multiple transcripts, each encoding a different protein [110].

Additionally, the use of mRNA as a proxy for protein concentration comes with limitations. Various proteins, including Ft, are known to be post-transcriptionally regulated, meaning mRNA may not be representative of protein concentration [128]. Despite this, our results clearly show a correlation between the QSM signal, which has been found to be linearly related to Ft protein concentration in the deep grey nuclei, and Ft gene expression. Although the highly correlated nature of microarray data makes PLSR an attractive choice, we recognize several limitations with this method. Real correlations may be overlooked depending on the chosen predictor set, and results are particularly sensitive to the signal-to-noise ratio of the dataset [129]. Errors may also be introduced in the QSM registration process. Finally, we are limited by the set of genes included in the AHBA dataset. For instance, Tim-1 appears to be relevant to iron homeostasis, yet it is not present in the AHBA microarray survey [55].

We restricted our analysis to the deep grey nuclei because that is where the QSM signal most accurately reflects iron concentration. In other regions of the brain where iron is also stored but in smaller amounts, such as the cortex, the positive susceptibility of iron within a voxel may be cancelled out by negative susceptibilities of other molecules, like myelin. In future, using algorithms designed to separate out the sub-voxel positive and negative susceptibility contributions, like DECOMPOSE-QSM [130], would allow for a more accurate measurement of iron in the brain, and would allow us to extend our analysis to regions outside the deep grey nuclei. Even in the deep grey nuclei, the positive susceptibility of iron dominates over other species in QSM. It would be interesting to redo our analyses with paramagnetic and diamagnetic susceptibility maps, especially in light of our finding that the correlation between QSM and MAL is highly significant. MAL is known to be present in compact myelin which is diamagnetic, however, we are unable to measure the contributions of diamagnetic species in the deep grey nuclei with QSM alone.

2.7   Conclusion

Our results show a positive correlation between QSM and expression of genes important for iron transport and storage and myelination across regions of the deep grey nuclei. This seemingly contradictory result likely points to the presence of oligodendrocytes in voxels containing iron-loaded Ft. Our analysis verifies the work of previous studies showing a relationship between QSM and genes relevant to iron homeostasis and myelination in the deep grey nuclei and expands upon these studies by using spatially localized gene expression data from the AHBA [63]–[65]. It is clear QSM is an informative estimate of iron homeostasis and shows valuable promise for use in understanding the complex pattern of iron accumulation in the brain.

Chapter 3

Mathematical Model of Brain Iron Accumulation

3.1 Motivation for Mathematical Model of Brain Iron Transport

It is currently unknown how or why iron accumulates in the deep grey nuclei regions of the brain over the lifespan. This question has implications for the understanding of neurodegenerative disorders like Alzheimer's disease, which is hallmarked by alterations in the normal trajectory of brain iron deposition [30], [31]. Previous attempts to study iron in the brain have focused largely on the dynamics of iron crossing the blood brain barrier (BBB), the expression of iron transport proteins, iron homeostasis on the intracellular level and iron uptake by specific neural cells [22], [24], [35], [101], [131], [132]. QSM and histology studies, like Perl's staining, have also been used to localize iron to specific regions of the brain [6], [42]. On the whole brain level, the study of iron transport dynamics has been limited to autoradiographic experiments on animal models [105], [133].

Autoradiographic studies have been performed mostly on mice and rats and involve injecting radioactively labeled iron isotopes into specific brain regions, the ventricles, or elsewhere in the body, like the peritoneum [22]. After injection and a waiting period, the brains of the animals are dissected and measured with autoradiogram to visualize the evolving distribution of iron [105], [133]. The results of these studies show that injected iron ultimately ends up in the deep grey nuclei, as is seen with QSM [133], [134]. Observing the distribution of iron on a very short time scale following injection yields further insights, suggesting that possible iron transport routes in the brain include the cerebral spinal fluid (CSF) and axonal transmission [105]. Other experimental work supports the theory of iron transport along axons. In particular, [106] identified two specific axonal pathways by which iron is transported and also showed that this transport is synaptically mediated. Although these studies have allowed for the identification of possible iron transport routes, they are limited to animal models and scope of brain regions considered.

In humans, the study of iron accumulation on the whole brain level is limited to the analysis of post-mortem brains or non-invasive observation using QSM. However, these types of study aren't able to observe the transport of iron within the brain. Although iron transport dynamics have been studied on the cellular level, as described in Chapter 2, there has been no attempt to model the dynamics of iron transport in humans on the whole brain level. The [106] experiment, although performed on mice, is exciting in that it is able to definitively determine the path of iron transport between brain regions. However, this type of experiment is costly and requires killing the experimental animals. In addition, the experimenters only focused on a small set of regions thought to be involved in neuropsychiatric disorders. A mathematical model of

iron transport in the brain using non-invasive MRI data is an approach to predicting possible iron transport routes in the brain that doesn't require costly experiments on animal models. The goal of this mathematical model is to non-invasively describe the dynamics of iron transport in the brain on the system level, in both space and time. To do that, we propose using a discrete-time Markov chain model with an input term.

3.2   Introduction to Markov Models

A discrete-time Markov chain is a stochastic process in which the state of the system is completely characterized by the state of the system in the previous time step [135], [136]. In other words, the system is memoryless and its behavior at a given time in the future depends only on the current state, rather than the history of all past behavior. This is called the Markov property, and a discrete-time Markov chain over n timesteps can be represented as a sequence of random variables $X_0, X_1, X_2, \ldots, X_n$ satisfying the Markov property:

$$\Pr(X_{n+1} = x \mid X_0 = x_0, X_1 = x_1, \ldots, X_n = x_n) = \Pr(X_{n+1} = x \mid X_n = x_n) \qquad (3.1)$$

3.3   Proposed Model and Properties

We model the expected density of iron in the brain at time n as follows:

$$\boldsymbol{x}[n] = \mathbf{T}\boldsymbol{x}[n-1] + \boldsymbol{s} \qquad (3.2)$$

The expected density of iron in all regions defined as nodes in the Markov chain at time n, $\boldsymbol{x}[n]$, is modeled as the expected density of iron at the previous time step, $\boldsymbol{x}[n-1]$, times a Markov transition probability matrix, $\mathbf{T}$, plus input term $\boldsymbol{s}$. The Markov probability matrix $\mathbf{T}$
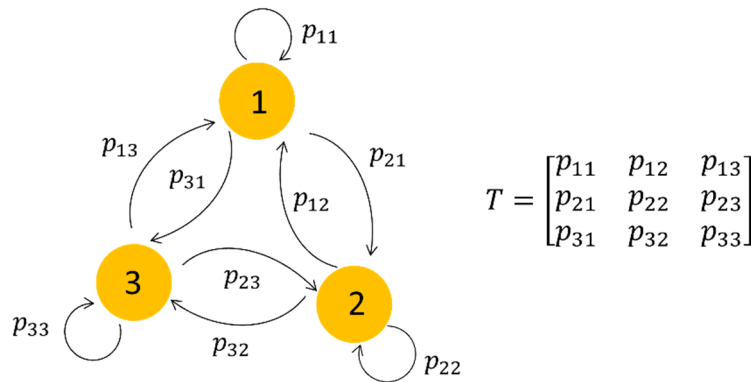

Figure 3.1: **Markov chain with three nodes**. The Markov transition probability matrix, T, is defined such that $T(i, j) = p_{ij} = probability\ of\ transmission\ from\ node\ j\ to\ node\ i$ ($i, j = 1,2,3$)

characterizes the probability of transitioning between all possible pairs of regions i and j over one time step for a discrete-time Markov chain with J possible regions, $i, j \in 1, 2, \ldots, J$:

$$\mathbf{T}(i,j) = p_{ij} = \Pr(X_{n+1} = i \mid X_n = j) \tag{3.3}$$

The size of $\mathbf{T}$ is determined by the number of regions defined as nodes in the Markov chain model, therefore, $\mathbf{T}$ is square. For a Markov chain with J regions, $\mathbf{T}$ has size J by J. $\mathbf{T}$ is also constrained to be non-negative and left-stochastic, as the values of $\mathbf{T}$ are well-defined conditional probabilities. Specifically, row i of $\mathbf{T}$ corresponds to the probability of transmission to region i from all other regions defined in the Markov chain, and column j of $\mathbf{T}$ corresponds to the probability of transmission from region j to all other regions in the Markov chain. Finally, we constrain $\mathbf{T}$ to be sparse, because from the perspective of the known distribution of iron in the brain, it makes sense that the number of allowable transitions of iron between regions would be relatively sparse compared to the number of regions in the Markov chain. Figure 3.1 illustrates an example of a Markov chain with three nodes ($J = 3$).

Equation 3.2 has the closed-form solution:

$$x[n] = \mathbf{T}^n x[0] + \left(\sum_{k=0}^{n-1} \mathbf{T}^k \right) s \tag{3.4}$$

Therefore, our model of the spatial and temporal dynamics of iron in the brain has the closed-form solution of exponential accumulation, which aligns with what has been observed in the deep grey nuclei regions of the brain with QSM [19].

3.4 Defining Source Input Term

The input term in the model, s, reflects the new iron being introduced into the brain each timestep across the BBB. Let the elements of s be $s_j, j = 1, 2, \ldots, J$. These are defined using values from literature including serum iron concentration, $C(Fe)$, cerebral blood volume measured in region j, CBV_j, and a hyperparameter to represent the fraction of iron crossing the BBB into region j, k_j:

$$s_j = C(Fe) \cdot CBV_j \cdot k_j \tag{3.5}$$

We set the constant $C(Fe)$ at $20 \ \mu M$, which has been found to be a healthy level of iron in the blood [35]. CBV_j is defined according to the tissue composition of region j:

$$CBV_j = \begin{cases} 4.6\dfrac{ml}{100g}, j \in grey\ matter \\ 1.3\dfrac{ml}{100g}, j \in white\ matter \end{cases} \qquad (3.6)$$

These values are from [137]. CBV was calculated using dynamic susceptibility contrast MRI collected from eighty healthy subjects, both male and female, aged 22 to 85 years [137]. We used the mean CBV across subjects found for grey matter regions (both cortical and deep grey nuclei regions) and white matter regions. Assuming a brain tissue density of $1\ g/cm^3$, we can convert s_j to units of iron concentration in the brain ($ng\ Fe/mm^3$) using the molar mass of iron:

$$\hat{s}_{j,grey} = \frac{20\ \mu mol\ Fe}{10^3\ ml\ blood} \cdot \frac{55.845\ g\ Fe}{10^6\ \mu mol\ Fe} \cdot \frac{4.6\ ml\ blood}{100\ g\ brain\ tissue} \cdot \frac{1\ g\ brain\ tissue}{10^3\ mm^3} \cdot k_j$$

$$\hat{s}_{j,grey} = .0514 \cdot k_j \left(\frac{ng\ Fe}{mm^3}\right) \qquad (3.7)$$

$$\hat{s}_{j,white} = \frac{20\ \mu mol\ Fe}{10^3\ ml\ blood} \cdot \frac{55.845\ g\ Fe}{10^6\ \mu mol\ Fe} \cdot \frac{1.3\ ml\ blood}{100\ g\ brain\ tissue} \cdot \frac{1\ g\ brain\ tissue}{10^3\ mm^3} \cdot k_j$$

$$\hat{s}_{j,white} = .0145 \cdot k_j \left(\frac{ng\ Fe}{mm^3}\right) \qquad (3.8)$$

These values are consistent with estimates of iron uptake across the BBB measured via autoradiographic studies [22].

3.5 Using QSM as an Estimate of Iron Concentration

In order to test our model and solve for the model parameters, we use QSM as an estimate of iron concentration in the brain, relying on the relationship between QSM and iron concentration found in the deep grey nuclei [25]. Assuming a brain tissue density of $1\ g/cm^3$, we can convert iron concentration estimated from QSM to units of $ng\ Fe/mm^3$:

$$\chi(ppm) = .00097 \cdot Fe \left(\frac{mg}{kg\ brain\ tissue}\right)$$

$$\widehat{qsm}\left(\frac{ng\ Fe}{mm^3}\right) = qsm(ppm) \cdot 1.308 \cdot 10^3 \qquad (3.9)$$

Substituting for iron density in our model yields:

$$x[n] = \widehat{qsm}[n] = \mathbf{T}\widehat{qsm}[n-1] + \mathbf{s} \qquad (3.10)$$

3.6   Limitations

We chose this model because it is interpretable and allows for identification of the transport pathways that result in the iron distribution seen in the brain over time and space. However, the model is limited in that we have chosen to make the Markov transition probability matrix and source input term time invariant. Making these time-variant would be significantly more difficult to define and would require a large dataset, although, there is biological evidence to support time-variance, particularly in the source term. The BBB is known to exhibit more leakage with age and likely plays a role in the iron accumulation seen in the ageing brain [138], [139]. Ageing-associated BBB dysfunction has been measured with DCE-MRI, and iron transport across the BBB has been mathematically modelled [131], [140], [141]. In the future, this could be used to better define our source term.

In addition, the use of QSM as an estimate for iron is limited in that the relationship between QSM and iron concentration (Eq. 3.9) has only been established for the deep grey nuclei regions, as mentioned in Chapter 2. The QSM signal in the cortex tends to be closer to zero because iron is stored in smaller amounts in these regions so there is more of a balance between positive and negative susceptibility contributions within voxels. The QSM signal is negative in white matter regions due to the presence of diamagnetic myelin, even though the cells which form the myelin sheath store the most iron in the brain, as discussed in Chapter 2. Algorithms have recently been developed to separate the sub-voxel positive and negative susceptibility contributions from the QSM signal. We improve upon our work by using paramagnetic component susceptibility maps calculated with DECOMPOSE-QSM [130] as a more accurate iron measurement estimate. This will be discussed in Chapter 7.

3.7   Conclusions

We have defined a mathematical model of iron transport in the brain on the system level and have proposed using QSM as a non-invasive estimate of iron in the brain. This work is novel in that it is the first effort to mathematically describe iron transport on the whole brain level. In addition, it is advantageous compared to previous attempts to study this problem using animal models in that it is non-invasive and comprehensively predicts iron transport between brain regions defined as nodes in the network model. This work has great potential to be used as a tool in tandem with more established autoradiographic experiments on animal models. Our model could be used to identify possible transport routes that could then be experimentally validated on an animal model as in [106]. A mathematical approach to this problem also opens up the possibility of non-invasively describing iron transport in humans, which is crucial for understanding aging-associated changes in the brain and neurodegeneration.

Chapter 4

Estimating Markov Transition Probabilities, Assuming Passive Diffusion

4.1   Introduction: Active vs. Passive Transport

We define two hypotheses to describe the driving factors of iron transport between brain regions defined as nodes in our Markov chain model. First, we consider that iron is transported primarily by passive diffusion in the brain. Passive diffusion refers to Brownian motion, or the random motion of particles due to thermal energy [142]. This is supported by evidence suggesting iron may be transported along axons, and diffusion in the brain largely follows the longitudinal direction of the white matter fibers which are highly anisotropic [142], [143]. Wang et al. [106] experimentally identified two distinct pathways by which iron is transported along axons, and, additionally found that this transport is synaptically modulated. Although this study demonstrates that passive diffusion along axons alone is not enough for the transport of iron in this specific pathway, other studies have provided evidence for larger-scale transport of iron along axons [37], [144]. Ferroportin, the iron exporter, has been found in synaptic vesicles, as well as axons and dendrites, and iron is found in the largest amounts in oligodendrocytes, the glial cells responsible for myelinating axons [9], [37], [105], [126], [144]. Ferritin, the iron storage protein, has also been localized to axons and may be partly secreted by oligodendrocytes, which wrap around axons forming the myelin sheath [145], [146].

Conversely, we consider that iron may be transported between regions largely by transporters and receptors. Chapter 2 discusses how iron import and export receptors are found in many cells of the brain, along with iron transport proteins. In addition, transferrin, the iron transporter, has been found in large amounts in the cerebral spinal fluid (CSF), which has also been suggested as a possible mechanism of iron transport between regions [22], [105]. Autoradiographic studies provide evidence that iron is translocated between brain regions, and this could be facilitated by active transport [22], [105], [133]. In order to make sense of these compounding mechanisms of iron transport, we consider each hypothesis individually. The focus of this chapter is the result of testing our first hypothesis, that iron is transported primarily by passive diffusion. We do this by estimating the transition probabilities of the Markov matrix using diffusion tensor imaging (DTI) MRI and then using these parameters in our model to predict the spatio-temporal evolution of iron in the brain over time.

4.2 Measurement for Passive Diffusion Hypothesis of Brain Iron Transport: DTI

Passive diffusion can be measured in the brain with DTI. DTI involves applying gradient pulses that cause a random phase shift in diffusing water molecules, resulting in a loss of signal in these voxels [142], [147]. The Stejskal-Tanner equation relates the signal loss to the diffusion of water in 3D space, as represented by a diffusion tensor [147]:

$$\frac{S_{k,i}}{S_{0,i}} = e^{-b\hat{g}_k^T \mathbf{D_i} \hat{g}_k} \tag{4.1}$$

The signal intensity measured per voxel, $S_{0,i}$, is compared to $S_{k,i}$, the signal intensity measured in voxel i after applying the kth diffusion-sensitizing gradient in direction $\hat{g}_k$ [147]. The constant b is calculated from the applied gradient field strength, the gradient duration, the time between gradient applications, and the gyromagnetic ratio constant [147]. The diffusion tensor can be found for each voxel by solving the Stejskal-Tanner equation backwards from the measured signal loss [147]. The diffusion tensor is a positive definite matrix defined for each voxel measured in the brain:

$$\mathbf{D_i} = \begin{bmatrix} D_{xx} & D_{xy} & D_{xz} \\ D_{yx} & D_{yy} & D_{yz} \\ D_{zx} & D_{zy} & D_{zz} \end{bmatrix} = \mathbf{D_i^T} > 0 \tag{4.2}$$

We used the measurement from one subject of a set of 16 subjects comprising the DTI Multiple Atlas Set, available online from the Center of Magnetic Resonance Microimaging at the Johns Hopkins Medical Institute (https://cmrm.med.jhmi.edu/). The collection of the DTI measurement is described in [148]. Subjects were scanned at the Montreal Neurological Institute and University of California Los Angeles on a 1.5T Siemens scanner using a single-shot echo-planar imaging sequence with sensitivity encoding gradient (matrix = 96 x 96, FOV = 240 x 240 mm, resolution 2.5 mm, b-value = 1000 s/mm^2). In addition, parallel imaging with an acceleration factor of two was used to reduce acquisition time. Five images were acquired without diffusion weighting, used for calculating the signal loss due to diffusion. DtiStudio was used to calculate the diffusion tensor for each voxel. The DTI images were then registered to the ICBM-152 template using Automated Image Registration and the diffusion tensors were transformed to this template using Landmarker software. Finally, interpolation was performed to yield DTI measurements with the same matrix size and voxel resolution as the ICBM-152 template (181x217x181, 1 mm^3 voxel resolution).

4.3 Methodologies

Since we measure a diffusion tensor (Eq. 4.2) for each voxel, we can use voxels as nodes in the Markov network model. The measured diffusion tensor is proportional to the covariance matrix of a Gaussian diffusion process, defined below [149]:

$$\rho(x|x_0, \tau) = \frac{1}{\sqrt{(2\pi)^3 det\ (\mathbf{\Sigma_i})}} e^{-\frac{1}{2}(x-x_0)^T \mathbf{\Sigma_i}^{-1}(x-x_0)}, \mathbf{\Sigma_i} = 2 \cdot \mathbf{D_i} \cdot \tau \qquad (4.3)$$

$\rho(x|x_0, \tau)$ is the probability density function of a three-dimensional Gaussian distribution characterized by the covariance matrix $\mathbf{\Sigma_i}$, where x and x_0 are vectors representing the starting and ending positions of the diffused particles in three-dimensional space. This matrix is defined using the measured diffusion tensor $\mathbf{D_i}$ (Eq. 4.2) and τ, the duration of diffusion. The diffusion tensor $\mathbf{D_i}$ is symmetric and positive-definite, therefore it has three orthogonal eigenvectors and three positive eigenvalues. The principal eigenvector describes the direction of the highest rate of diffusion, which follows the longitudinal axis of the white matter fibers in the brain, in regions where the structure of the fibers is organized [147]. $\rho(x|x_0, \tau)$ represents the probability of diffusion in three dimensions by an ellipse whose axes are the eigenvectors of $\mathbf{D_i}$ and whose lengths are $\sqrt{2\tau\lambda_i}$, where $\lambda_i, i = 1, 2, 3$ are the eigenvalues of $\mathbf{D_i}$. Let $x_i = (x_i, y_i, z_i)$ be the position of voxel i and $x_j = (x_j, y_j, z_j)$ be the position of voxel j. We can calculate the probability of diffusion between voxels i and j over timestep τ by integrating the Gaussian pdf defined for a pair of voxels (Eq. 4.3) over the area of one voxel:

$$\mathbf{T}(i, j) = \iiint\limits_{(x_i,y_i,z_i)-\frac{1}{2}}^{(x_i,y_i,z_i)+\frac{1}{2}} \rho(x|x_j, \tau)\ dxdydz \qquad (4.4)$$

After defining the elements of $\mathbf{T}$ for all voxels in the brain, we can estimate the density of iron in the brain by using our model to forward simulate from an initial distribution set by QSM (Eq. 3.10):

$$x[\tau] = \mathbf{T}\widehat{qsm}[\tau - 1] + s \qquad (4.5)$$

For this, we initially set the source hyperparameter term k equal to 1. Also, since we include voxels in the CSF in addition to grey and white matter as nodes in our Markov model relying on the assumption of passive diffusion, we define a source value for these as well. However, we make these negative due to evidence indicating iron is excreted from the CSF [22], [105]. We use grey matter, white matter, and CSF parcellations provided by (https://cmrm.med.jhmi.edu/), accompanying the DTI measurement to define voxels as belonging to grey matter, white matter, or CSF for the purpose of defining the source term for each voxel (see Eqs. 3.7 and 3.8 for the source definition of grey and white matter voxels) [150], [150], [151]. We estimate the CSF source term using iron measurements taken from the CSF described in [152], that observed iron concentrations in the CSF at 20.14 ng/dl. Using the rate of CSF production observed in humans,

.3-.6 ml/min, we can estimate the iron efflux from the CSF as follows (we use the mean of the range of CSF production reported in [153]):

$$\hat{s}_{j,CSF} = -1 \cdot \frac{20.14 \ ng \ Fe}{10^{-1} \ L \ CSF} \cdot \frac{1 \ L}{10^6 \ mm^3} \cdot \frac{1000 \ mm^3}{1 \ ml} \cdot .5ml$$

$$\hat{s}_{j,CSF} = -.101 \cdot \left(\frac{ng \ Fe}{mm^3}\right) \tag{4.6}$$

We choose a time step τ of 1 minute, so that we can reasonably make the assumption that diffusion is limited to nearest neighboring voxels only. The diffusion defined by $\mathbf{D_i}$ can be thought of as an ellipse with lengths $\sqrt{2\tau\lambda_i}$, therefore, the maximum range of diffusion can be defined by the principal eigenvalue of $\mathbf{D_i}$, $\lambda_{max} = .0047 \ ^{mm^2}/_S$, and τ:

$$Max \ Diffusion = \sqrt{2 \cdot \tau \cdot \lambda_{max}} = \sqrt{2 \cdot 60 \ s \cdot 0047 \ ^{mm^2}/_S} = .75 \ mm \tag{4.7}$$

This limits the Markov transition probability matrix to be sparse and makes the problem much more computationally feasible.

4.4   Results: Passive Diffusion Model

After using DTI to define the transition probabilities in our model and then forward simulating from an initial distribution set by QSM, we see that the predicted distribution of iron in the brain ends up uniform over time. This pattern is observed even though the initial distribution set by QSM is non-uniform and reflects iron accumulation in the deep grey nuclei. These experimental results do not reflect the actual distribution of iron in the brain seen over the lifespan. From this, we conclude that passive diffusion alone cannot explain the iron accumulation seen in the deep grey nuclei with aging.
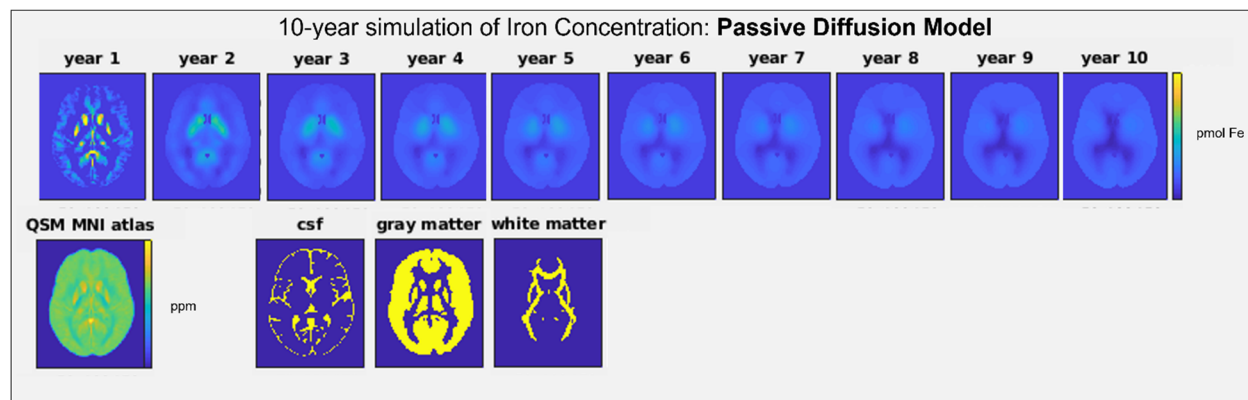
Figure 4.1: **10-year simulation of iron concentration: passive diffusion model**. The results predicted by our model, after defining the Markov transition probabilities using DTI under the passive diffusion hypothesis, indicate that passive diffusion alone is not sufficient to describe the transport of iron in the brain. We used our model to forward simulate from an initial distribution set by QSM (see QSM MNI atlas) by 10 years. All voxels were defined as nodes in the model, and the source term for each voxel was defined by Eqs. 3.7, 3.8, and 4.6. The CSF, Gray matter, and White matter segmentations were used to classify voxels by type in order to define the source term.

4.5   Discussion and Conclusions

Our results show that passive diffusion is not sufficient to describe brain iron transport. Relying on the passive diffusion hypothesis to estimate the parameters of our model results in a model prediction of uniform distribution of iron in the brain, which is contrary to the observed accumulation of iron in the deep grey nuclei regions of the brain [19]–[21]. Although evidence for axonal transport of iron supports the hypothesis of passive diffusion, this result isn't surprising as there are other mechanisms known to govern iron homeostasis in the brain, namely several transporters and storage proteins that are highly regulated in response to brain iron levels, as discussed in Chapter 2. Likely, iron is transported in the brain through a combination of passive and active processes. In future, it would be interesting to expand our model by accounting for this.

It makes sense that iron homeostasis is controlled by such a robust process, rather than the randomness of passive diffusion, as excess iron is harmful to neural cells [32], [33], [42]. Despite the harm posed by its accumulation, iron is required for several neural processes, discussed in Chapter 1. In order to manage this balance, the brain has developed a way to regionally control iron intake to ensure critical levels are met. This is done by iron-responsive elements that are found on the mRNA transcripts of several iron transporters, making them reactive to iron levels in the cellular environment [154]. The molecule hepcidin acts as a further control on active transport of iron in the brain as it directly affects the expression of the iron

exporter ferroportin [155]. These control mechanisms cannot be accounted for under our passive diffusion hypothesis.

We conclude that the active transport hypothesis is a likelier explanation for iron homeostasis in the brain and describe testing this hypothesis in the next chapter. Passive diffusion alone cannot provide the level of control and specificity required for brain iron transport. Instead, we hypothesize that the brain relies on active transport proteins to control cellular levels of iron and to ensure it is stored and transported in a regulated manner. Although there is much work that has been done to describe iron homeostasis in the brain on the cellular level involving these proteins, it is unclear how these systems result in the accumulation seen in the deep grey nuclei [131], [140]. We attempt to bridge this gap by describing the transport of iron in the brain with our Markov model and solving for the transition probabilities under the assumption of active transport using QSM.

Chapter 5

Estimating Markov Transition Probabilities, Assuming Active Transport

5.1 Introduction

The results of the previous chapter indicate that passive diffusion alone can't explain the spatial and temporal pattern of iron seen in the aging brain. In this chapter, we consider our second hypothesis, that iron transport in the brain is facilitated largely by active transport. In Chapters 1 and 2, we discussed how the proteins transferrin (Tf), ferroportin (Fpn), divalent metal transporter 1 (DMT1), and ferritin (Ftn) are involved in the active transport of iron within the brain. The distribution of these transporters among various cell types in the brain suggests that glial cells like oligodendrocytes and microglia are likely involved in these pathways [156]. Both glial cells are found in high numbers in deep grey nuclei regions that accumulate iron and have been shown to highly express ferritin [88], [89], [156]. The results from our comparative analysis of QSM and the expression of iron homeostasis and myelin genes in Chapter 2 also support the theory that iron loaded ferritin in the deep grey nuclei is localized to oligodendrocytes. We are interested in using our model to predict the network of iron transmission that results in the accumulation of iron in these cells.

Autoradiographic studies indicate that iron may be translocated between distant regions in the brain, and the presence of Fpn in synaptic vesicles suggests that the wide-scale transport of iron along axons may play a role in this [37], [105]. In particular, [106] have identified two axonal pathways of iron transport in the mouse brain: from the ventral hippocampus (vHip) to the medial prefrontal cortex (mPFC) to the substantia nigra (SN), and from the thalamus (Tl) to the amygdala (Amygd) to the mPFC. Interestingly, these results suggest that the SN, a brain region known to accumulate iron over the lifespan, may act as an iron sink for excess iron from the mPFC. It's likely that iron transporters are involved in these pathways. This is supported by the presence of Fpn and Ftn in axons [144], [145]. Also, receptors for Tf are dense in the vHip, Aymgd, mPFC, and Tl, but not in the SN [22]. This suggests that the translocation of iron between regions, facilitated by active transport, could ultimately explain the accumulation seen in the deep grey nuclei.

In conclusion, there are multiple possible mechanisms by which the active transport of iron may facilitate the accumulation of iron in the deep grey nuclei. In Chapter 2, we reported a positive relationship between QSM and the expression of multiple genes involved in the active transport of iron. In order to evaluate our second hypothesis, that iron is largely moved

throughout the brain by transport proteins and receptors, we solve for the transition probabilities of our Markov model by setting up a regression problem using QSM measurements taken across regions of the brain at different time points.

5.2   Methodology: Optimization Problem Set-up and QSM Datasets

5.2.1 QSM acquisition and post processing

It would be prohibitive to obtain QSM measurements for a single person over the lifespan, so we rely on an average of healthy QSM subjects, aged 30-80, from two distinct datasets. The collection of the first dataset by Yuyao Zhang is described in Chapter 2. The collection of the second dataset is described in [31]. Subjects were scanned on a 3T scanner (Siemens Prisma VE11C at Mayo Clinic) as part of the Mayo Clinic Study of Aging, which had the approval of the institutional review board and written informed consent from participants. Images were acquired using a three-dimensional multi-echo gradient echo sequence (TE1/spacing/TE5 = 6.7/3.9/22.4 ms, TR = 28 ms, original spatial resolution .52 x .52 x 1 mm^3 resampled to 1 x 1 x 1.8 mm^3), and STI suite was used to reconstruct the QSM for each subject. The brain mask was generated using FSL's BET. Masking, Laplacian-based phase unwrapping and background phase removal were performed using V-SHARP [53], [68]–[70]. The radius of the spherical mean value filter was set to 1 pixel at the boundary of the brain and 12 pixels at the center of the brain. Finally, QSM images were calculated from the filtered phase using the Improved Sparse Linear Equation and Least-squares (iLSQR) algorithm [71], [157]. Susceptibility values were again referenced relative to the mean susceptibility across the whole brain.

For both datasets, Advanced Normalization Tools (ANTs) is used to perform nonlinear registration between each subject QSM and the age-specific QSM atlas constructed using group-wise registration in [20], as described in Chapter 2. This atlas includes regions defined in the AAL3 atlas, which distinguishes functionally distinct regions in the cortex, cerebellum, white matter, and deep grey nuclei, plus additional deep grey nuclei regions segmented from QSM images [20], [158]. Average QSM values in these regions are calculated in the same way as described in Chapter 2. These are then converted to iron concentration estimates using Eq. 3.9.
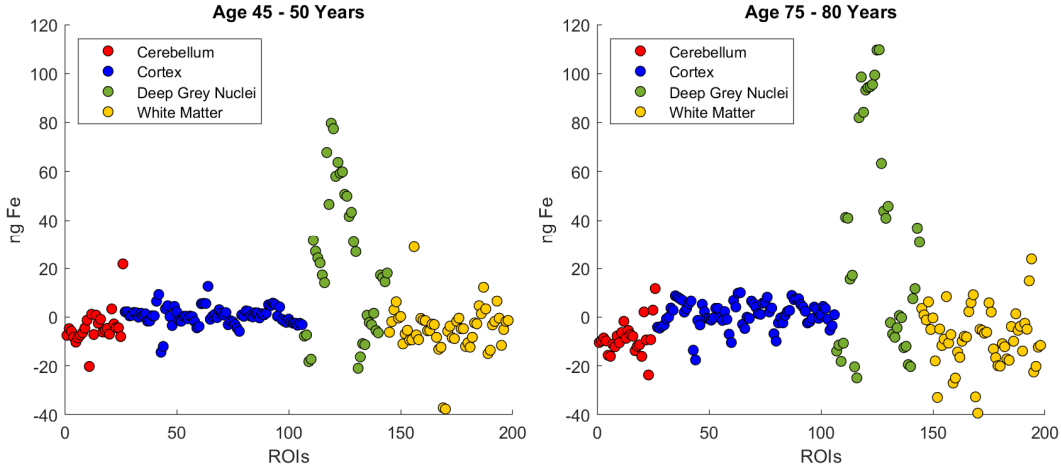
Figure 5.1: **Iron estimates calculated from QSM**. These figures show iron estimates from QSM images collected by Y. Zhang et al. [20], following the processing described in 5.2.1. This estimate accurately captures the accumulation of iron in the deep grey nuclei, as seen in the comparison between the two age groups. The negative iron estimate in many cerebellar and white matter regions reflects the limitations of QSM in estimating iron in these regions.

Finally, we resample the two populations so their age distributions are comparable. First, each population is partitioned into bins of 5 years and then we identify which population has fewer subjects for each age bin. We randomly draw the minimum number of subjects from the total collection of subjects in the age bin for each population and then average these together. We repeat this for each 5-year bin. We then linearly interpolate between the age bins to yield time points every year. This is done to make the time resolution more uniform between the two populations.

5.2.2 Regression problem and optimization

Figure 5.1 shows the iron estimate calculated from the average QSM across regions in the brain, demonstrating iron accumulation in deep grey nuclei regions and increasing accumulation over time. The cerebellum and white matter show large numbers of negative iron density estimates, indicating the presence of diamagnetic species dominating over the paramagnetic iron signal [51]. For this reason, we only use grey matter regions as nodes in our Markov model (See Tables 5.1 and 5.2). Also, we threshold the iron density estimates to be positive. Using these iron estimates, we set up the following regression problem for both datasets separately to solve for the transition probabilities of the Markov matrix. For region $i \in 1, \ldots, N,$ source input $s_i,$ and iron estimates $\widehat{qsm}_i[1], \ldots, \widehat{qsm}_i[M]$ we can define the following relationship using our model of iron density in the brain:

$$\widehat{qsm}_i[n] = \sum_{j}^{N} p_{ij} \cdot \widehat{qsm}_j[n-1] + s_i \tag{5.1}$$

$$\begin{pmatrix} \widehat{qsm}_i[2] \\ \vdots \\ \widehat{qsm}_i[M] \end{pmatrix} = \begin{pmatrix} \widehat{qsm}_1[1] & \cdots & \widehat{qsm}_N[1] \\ \vdots & \ddots & \vdots \\ \widehat{qsm}_1[M-1] & \cdots & \widehat{qsm}_N[M-1] \end{pmatrix} \cdot \begin{pmatrix} p_{i1} \\ \vdots \\ p_{iN} \end{pmatrix} + \begin{pmatrix} s_i \\ s_i \\ s_i \end{pmatrix}$$

$$\widehat{qsm}_i = Q_i p_i + s_i \tag{5.2}$$

Solving for p_i across regions in the brain:

$$\min_{p_i} \frac{1}{2M} \|(\widehat{qsm}_i - s_i) - Q_i p_i\|_2^2 + \lambda \|p_i\|_1, \quad s.t. \quad p_i \geq 0, \; \textstyle\sum_{j\epsilon column} p_{ij} = 1 \tag{5.3}$$

We use this optimization problem to find the Markov transition probabilities that minimize the difference between the left side of Eq. 5.2 and the right side. The regularization term will drive the solution to be sparse, and the constraints of the Markov matrix are also included. We use Mosek and CVX, a package for constructing and solving convex optimization models, to solve this problem [159]–[161]. The input term for region i, s_i, is equal to a constant multiplied by a hyperparameter term k (See Eqs. 3.7, 3.8).

The optimal hyperparameters are found for each training dataset using grid search. The values of λ and k are selected that minimize the prediction error term in the cost function, defined as $\|(\widehat{qsm}_i - s_i) - Q_i p_i\|_2^2$. These are $(\lambda, k) = (.1, 1e\text{-}4)$ for Control Population 1, yielding an L-2 norm of 1.19. For Control Population 2, $(\lambda, k) = (1000, 1e\text{-}14)$, giving an L-2 norm of .83. After finding the optimal hyperparameters using grid search, we use these hyperparameters to solve for the Markov transition probability matrix of each control population following bootstrapping resampling. We leave one subject out of each age bin at random for each bootstrap run and perform 1000 leave-one-out bootstrap runs. As discussed in the next section, this formulation yields a Markov transition probability matrix that can predict the distribution of iron in the brain quite accurately.

Region of Interest	Brain Area	Abbreviation
Precentral Gyrus	Primary Motor Cortex	PMC
Superior Frontal Gyrus, Lateral	Dorsolateral Prefrontal Cortex	dlPFC
Middle Frontal Gyrus	Dorsolateral Prefrontal Cortex	dlPFC
Inferior Frontal Gyrus, Opercular	Ventrolateral Prefrontal Cortex	vlPFC
Inferior Frontal Gyrus, Triangular	Ventrolateral Prefrontal Cortex	vlPFC
Inferior Frontal Gyrus, Orbital	Ventrolateral Prefrontal Cortex	vlPFC
Rolandic Operculum	Operculum	Oper
Supplementary Motor Area	Supplementary Motor Area	SMA
Parolfactory Gyri	Medial Prefrontal Cortex	mPFC
Superior Frontal Gyrus	Medial Prefrontal Cortex	mPFC
Inferior Rostral Gyrus	Orbitofrontal Cortex	OFC
Gyrus Rectus	Orbitofrontal Cortex	OFC
Medial Orbital Gyrus	Orbitofrontal Cortex	OFC
Anterior Orbital Gyrus	Orbitofrontal Cortex	OFC
Posterior Orbital Gyrus	Orbitofrontal Cortex	OFC
Lateral Orbital Gyrus	Orbitofrontal Cortex	OFC
Insula	Insula	Ins
Cingulate Gyrus, Parietal	Medial Prefrontal Cortex	mPFC
Cingulate Gyrus, Retrosplenial	Posteromedial Cortex	PC
ParaHippocampal Gyrus	Ventral Temporal Cortex	VTC
Calcarine	Primary Visual Cortex	PVC
Left Cuneus	Cuneus	Cun
Lingual Gyrus	Lingual	Ling
Superior Occipital Gyrus	Occipital Gyri	Occ
Occipito-Temporal Gyrus	Occipital Gyri	Occ
Inferior Occipital Gyrus	Occipital Gyri	Occ
Fusiform Gyrus	Ventral Temporal Cortex	VTC
Postcentral Gyrus	Primary Somatosensory Cortex	PSC
Superior Parietal Lobule, Superior	Superior Parietal Lobule	SPL
Superior Parietal Lobule, Inferior	Superior Parietal Lobule	SPL
SupraMarginal Gyrus	Inferior Parietal Lobule	IPL
Angular Gyrus	Inferior Parietal Lobule	IPL
Precuneus	Precuneus	Precun
Paracentral Lobule, Posterior	Paracentral Lobule	PCL
Heschl's Gyrus	Primary Auditory Cortex	PAC
Superior Temporal Gyrus	Primary Auditory Cortex	PAC
Planum Polare	Temporal Pole	Temp
Middle Temporal Gyrus	Inferior Temporal Cortex	ITC
Temporal Pole	Temporal Pole	Temp
Inferior Temporal Gyrus	Inferior Temporal Cortex	ITC

Table 5.1: **Cortical regions used as nodes in the Markov model**. The regions of interest were used from both the left and right hemispheres. These regions were grouped into larger brain areas in order to better interpret the results of the model prediction.

Region of Interest	Abbreviation
Hippocampus	Hipp
Amygdala	Amygd
Putamen	Pu
Caudate nucleus	CN
Nucleus accumbens	NAcc
Extended amygdala	ExtAmygd
External globus pallidus	ExtGP
Internal globus pallidus	IntGP
Pars reticulata of substantia nigra	SNpr
Pars compacta of substantia nigra	SNpc
Red nucleus	RN
Subthalamic nucleus	SubTl
Ventral pallidum	VP
Anterior nuclei of thalamus	AntTl
Median nuclei of thalamus	MedTl
Internal medullary lamina of thalamus	IMTl
Lateral nuclei of thalamus	LatTl
Pulvinar nuclei of thalamus	PuTl
Dentate nucleus	DN

Table 5.2: **Deep grey matter regions used as nodes in the Markov model**. The regions of interest were used from both the left and right hemispheres.

5.3   Results: Comparison Among Control Populations

In order to see how the solver performs under this problem, we define a ground truth Markov probability matrix, **T**, of random values, and then use this to forward simulate iron density measurements with our model. We then solve for the predicted **T** from the simulated data. The results of this analysis show that the solver is able to recover the ground truth with minimal error, for a range of sparsity levels and number of timepoints used for training. As shown in Fig. 5.3, the error between the solver prediction and the ground truth is extremely low, and it is fairly consistent across sparsity levels and the number of measurements used for training. The range of sparsity levels used to test the solver reflects the sparsity of the Markov probability matrix solved from QSM iron estimates. This indicates that the solver is able to correctly recover a solution for our optimization problem. We now move on to reporting the results when the regression problem is solved using QSM iron estimates from two distinct healthy populations.
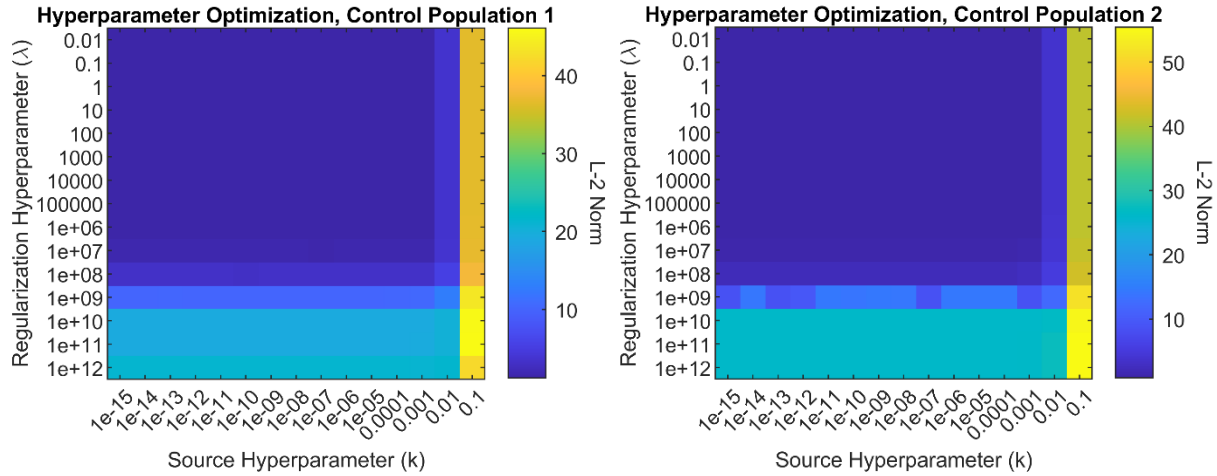
Figure 5.2: **Hyperparameter Optimization**. We define a logarithmic grid of the hyperparameters k and λ to include the values that yield a nil solution, set up the optimization problem for each pair of values and then solve for the Markov probability transition matrix. The optimal hyperparameters are the values of k and λ that minimize the L-2 norm term in the cost function of the optimization problem.
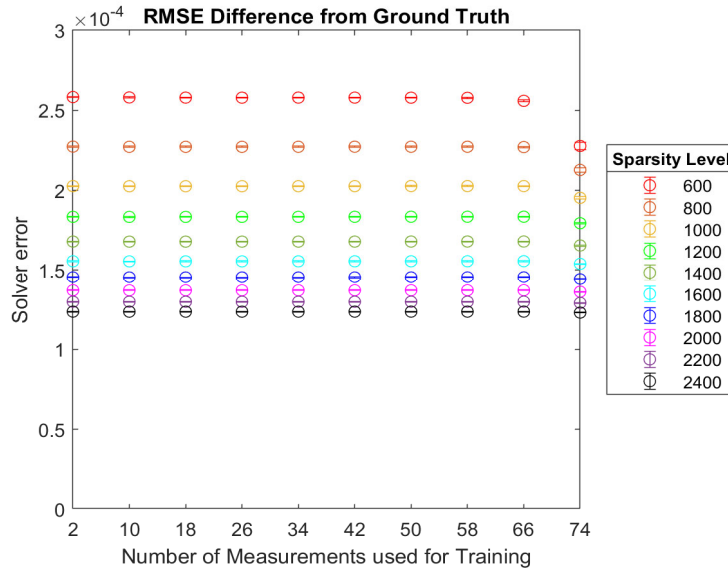
Figure 5.3: **Testing Solver with Ground Truth**. Solver error is defined as the root mean square error (RMSE) between the predicted Markov transition probability matrix and the ground truth matrix, **T**. The x-axis refers to the number of measurements that were used to solve for the predicted **T**. The number of non-zeros of **T** is indicated by the color of the points on the plot.

The predicted Markov transition probabilities can be visualized as edges in a network, where nodes are gray matter regions in the brain. The weight of the connections between regions represents the value of the estimated probability of transmission between those regions.

- Left External globus pallidus
- Left Internal globus pallidus
- Right Internal globus pallidus
- Left Pars reticulata of substantia nigra
- Left Pars compacta of substantia nigra
- Right Pars compacta of substantia nigra
- Left Red nucleus
- Left Subthalamic nucleus
- Right Extended amygdala
- Left Anterior nuclei of thalamus
- Right Orbitofrontal Cx
- Left Internal medullary lamina of thalamus
- Left Median nuclei of thalamus
- Left Posterior Cingular Cx
- Right External globus pallidus
- Left Dentate nucleus

- Left Hippocampus
- Right Primary Motor Cx
- Left Insula
- Left Ventral pallidum
- Left Lateral nuclei of thalamus
- Left Amygdala
- Right Insula
- Right Hippocampus
- Right Amygdala
- Right Internal medullary lamina of thalamus
- Left Putamen
- Left Caudate nucleus
- Left Nucleus accumbens
- Left Pulvinar nuclei of thalamus
- Right Pulvinar nuclei of thalamus
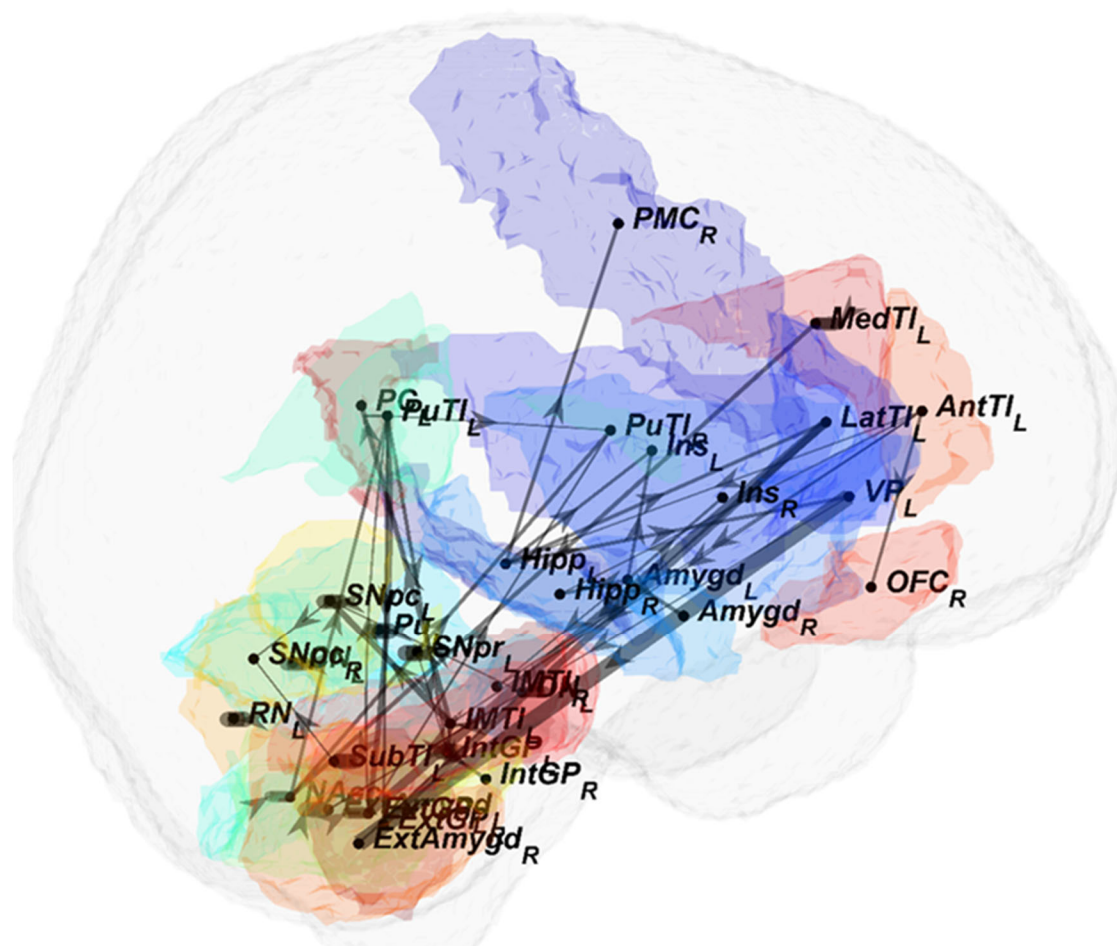- Left Extended amygdala

(a)

(b)

Figure 5.4: **Predicted Markov network transmission of iron**. Visualization of the Markov transition probability matrix found for Control Population 1 (averaged over 1000 bootstrap runs), (a) axial and (b) sagittal view. The Markov transition probability matrix was thresholded at .08, and only connections originating from the deep grey nuclei regions of the left hemisphere are displayed, for better visualization. Legend at the top of the figure.

Figure 5.4 is a visualization of the predicted Markov transition probability network for Control Population 1 (averaged over 1000 bootstrap runs). For better visualization, this figure only shows connections above a threshold of .08 and originating from deep grey matter regions of the left hemisphere. Interestingly, the model is predicting connections between the thalamus (Tl) and multiple deep grey nuclei like the amygdala (Amygd), hippocampus (Hipp) and globus pallidus (GP), as well as connections between the amygdala of both hemispheres, which could reflect transmission of iron through the CSF as the amygdala is directly adjacent to the lateral ventricle. The model is also predicting high probability of self-transmission in regions like the substantia nigra (SN), GP, dentate nucleus (DN), red nucleus (RN), external amygdala (ExtAmygd) and other deep grey nuclei.

(a)

Control
Population 1

(b)

Control
Population 2

Figure 5.5: **Predicted Markov network transmission of iron, two healthy populations**.
Visualization of the predicted Markov probability matrix, averaged over 1000 bootstrap runs and
thresholded at .03, for (a) Control Population 1, and (b) Control Population 2. Line weights
indicate connection strength and colors indicate the node of origin. Self-transmission is not
displayed. The full names of all nodes are listed in Tables 5.1 and 5.2.

Figure 5.5 provides another representation of the predicted Markov transition probability
matrix for both healthy populations, showing connections between all distinct nodes, above the
threshold of .03 (chosen to be the smallest value with reasonable visibility of the network
structure). This figure does not display self-transmission. The weights of the lines indicate
connection strength, and the colors indicate the node from which the connection originated. The
predicted networks for both healthy populations appear similar, however, the probability values
for control population 1 are larger than those for control population 2, as evidenced by the
increased thickness of the connections in the figure. Both models predict high connectivity in the
DN, SN, ExtAmygd, GP, and other deep grey nuclei, as well as multiple connections between
thalamic nuclei and several deep grey nuclei. See Tables 5.3 and 5.4 which list the connections
for both populations above a threshold of .05.

The comparison between the transition probabilities predicted for both populations is
further explored by performing linear regression between the two, across all nodes in the Markov
model. Before regression, the transition probabilities were thresholded at .008 (one divided by
the total number of nodes (124)). The result of this analysis, given in Figure 5.6, shows that the
predicted Markov transition probabilities of Control Population 1 and Control Population 2 are
significantly positively correlated (p value = 0., degree of freedom = 15374). However, the R-
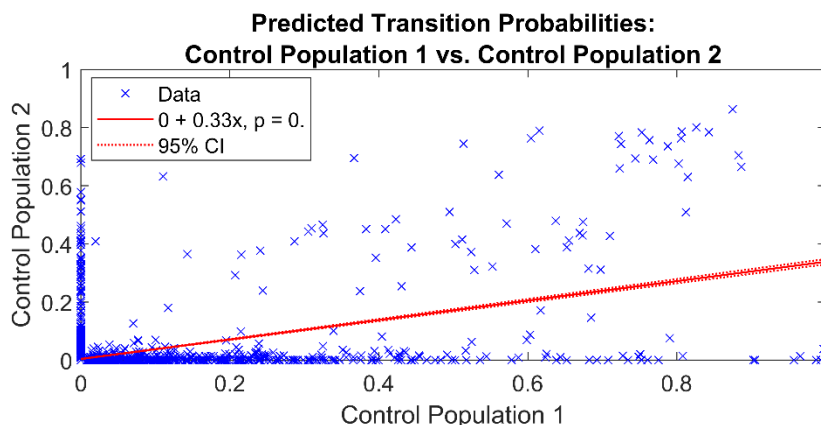squared term was reasonably low at .249, which may indicate possible overfitting.

Figure 5.6 **Predicted transition probabilities: control population 1 vs. control population 2**.
Linear regression between Markov transition probabilities predicted for both control populations
shows that the two predictions are significantly positively correlated.

This model is able to accurately predict the distribution of iron, as compared to a separate
healthy population, as shown in Fig. 5.7. The model prediction when trained on control

population 1 is overlaid onto the iron measurement, as estimated from QSM, for control population 2 at the same age. This prediction was obtained by forward simulated to age 80 starting from an initial distribution set by QSM iron estimates from control population 2, age 30. This figure also shows the model prediction and test set measurement on separate plots, with the nodes of the network color-coded for either cortical or deep grey regions. These results show that our model is robust to training on QSM iron estimates from distinct healthy populations.

The training error for control population 1, averaged over the 1000 bootstrap runs, was determined to be 2.38 ng Fe, and the testing error was 4.87 ng Fe. The training error was calculated as the root mean square error difference between the model prediction, $Q_i p_i^{Cntrl1}$, and the training data, $\widehat{qsm}^{Cntrl1}_i$. The testing error was calculated as the root mean square error difference between the model prediction, when trained on control population 1, $Q_i p_i^{Cntrl1}$, and the testing set, $\widehat{qsm}^{Cntrl2}_i$ (QSM iron estimates from control population 2):

$$Training\ Error = \ RMSE\{Q_i p_i^{Cntrl1} - \left(\widehat{qsm}^{Cntrl1}_i - s_i\right)\} \qquad (5.4)$$

$$Testing\ Error = \ RMSE\{Q_i p_i^{Cntrl1} - \left(\widehat{qsm}^{Cntrl2}_i - s_i\right)\} \qquad (5.5)$$

This result, reported in Table 5.5, further illustrates that our model is able to predict transmission of iron in a healthy population distinct from the training dataset.

Transmission of Iron To/From Deep Grey Nuclei, $p > .05$
Control Population 1

ROI	From x to ROI	To x From ROI
$NAcc_L$	$NAcc_L(0.618)$, $PCL_L(0.148)$, $mPFC_R(0.105)$, $MedTl_L(0.091)$, $MedTl_R(0.056)$, $dlPFC_R(0.055)$, $mPFC_L(0.051)$, $PSC_R(0.051)$	$NAcc_L(0.618)$, $ExtGP_R(0.058)$, $ExtGP_L(0.051)$
$NAcc_R$	$NAcc_R(0.58)$, $PCL_R(0.109)$, $mPFC_R(0.078)$, $PSC_R(0.064)$, $MedTl_R(0.061)$	$NAcc_R(0.58)$
$ExtAmygd_L$	$ExtAmygd_L(0.673)$, $dlPFC_R(0.133)$, $mPFC_R(0.123)$, $VTC_L(0.12)$, $LatTl_L(0.09)$, $mPFC_R(0.081)$, $ExtAmygd_R(0.079)$, $VTC_R(0.071)$, $IMTl_R(0.071)$, $AntTl_R(0.071)$, $VP_L(0.068)$, $AntTl_L(0.068)$, $mPFC_R(0.065)$, $MedTl_R(0.063)$, $PMC_R(0.063)$, $LatTl_R(0.062)$, $mPFC_R(0.062)$, $mPFC_L(0.059)$, $PC_R(0.055)$, $VP_R(0.055)$, $Ling_L(0.052)$	$ExtAmygd_L(0.673)$
$ExtAmygd_R$	$ExtAmygd_R(0.747)$, $OFC_R(0.102)$, $mPFC_R(0.086)$, $mPFC_L(0.08)$, $LatTl_L(0.072)$, $mPFC_R(0.071)$, $LatTl_R(0.069)$, $IMTl_R(0.067)$, $PAC_L(0.067)$, $PuTl_R(0.064)$, $VP_L(0.061)$, $PAC_R(0.06)$, $mPFC_R(0.059)$, $AntTl_R(0.058)$, $PMC_R(0.053)$, $VP_R(0.051)$	$ExtAmygd_R(0.747)$, $ExtAmygd_L(0.079)$
$ExtGP_L$	$ExtGP_L(0.712)$, $mPFC_R(0.163)$, $mPFC_L(0.162)$, $LatTl_L(0.154)$, $VTC_R(0.153)$, $LatTl_L(0.152)$, $IMTl_R(0.147)$, $PuTl_R(0.111)$, $AntTl_R(0.11)$, $Ins_L(0.107)$, $IMTl_L(0.107)$, $AntTl_L(0.103)$, $VP_L(0.101)$, $Ins_R(0.091)$, $mPFC_R(0.09)$, $Hipp_R(0.083)$, $VP_R(0.081)$, $PMC_R(0.073)$, $mPFC_R(0.073)$, $ExtGP_R(0.069)$, $OFC_R(0.065)$, $VTC_L(0.064)$, $Hipp_L(0.055)$, $PAC_L(0.052)$, $PMC_L(0.052)$, $NAcc_L(0.051)$, $mPFC_L(0.051)$	$ExtGP_L(0.712)$, $ExtGP_R(0.053)$, $IntGP_L(0.053)$
$ExtGP_R$	$ExtGP_R(0.708)$, $LatTl_L(0.157)$, $mPFC_R(0.151)$, $VTC_R(0.143)$, $IMTl_R(0.142)$, $mPFC_L(0.142)$, $LatTl_R(0.129)$, $VP_L(0.127)$, $PuTl_R(0.124)$, $AntTl_R(0.115)$, $Ins_L(0.115)$, $IMTl_L(0.109)$, $Ins_R(0.109)$, $AntTl_L(0.107)$, $PMC_R(0.086)$, $VP_R(0.083)$, $Hipp_R(0.073)$, $PMC_L(0.07)$, $NAcc_L(0.058)$, $OFC_R(0.058)$, $OFC_R(0.054)$, $mPFC_R(0.054)$, $Hipp_L(0.054)$, $ExtGP_L(0.053)$	$ExtGP_R(0.708)$, $ExtGP_L(0.069)$, $IntGP_R(0.064)$
$IntGP_L$	$IntGP_L(0.721)$, $VTC_L(0.142)$, $mPFC_R(0.121)$, $LatTl_R(0.12)$, $OFC_R(0.117)$, $LatTl_L(0.112)$, $mPFC_L(0.098)$, $mPFC_L(0.094)$, $OFC_R(0.08)$, $IMTl_R(0.078)$, $AntTl_L(0.076)$, $VTC_R(0.074)$, $AntTl_R(0.073)$, $Ins_R(0.072)$, $IMTl_L(0.071)$, $VTC_L(0.068)$, $mPFC_R(0.066)$, $Ins_L(0.063)$, $VTC_R(0.061)$, $VP_L(0.055)$, $ExtGP_L(0.053)$, $VP_R(0.051)$	$IntGP_L(0.721)$, $IntGP_R(0.057)$
$IntGP_R$	$IntGP_R(0.699)$, $LatTl_R(0.138)$, $VTC_R(0.138)$, $mPFC_R(0.132)$, $mPFC_L(0.131)$, $Ins_R(0.121)$, $LatTl_L(0.119)$, $IMTl_R(0.118)$, $VTC_L(0.101)$, $OFC_R(0.099)$, $Ins_L(0.097)$, $IMTl_L(0.097)$, $AntTl_L(0.095)$, $AntTl_R(0.093)$, $VP_R(0.077)$, $mPFC_L(0.066)$, $ExtGP_R(0.064)$, $Hipp_L(0.058)$, $IntGP_L(0.057)$, $PuTl_R(0.057)$, $OFC_R(0.052)$, $VP_L(0.05)$	$IntGP_R(0.699)$
$SNpr_L$	$SNpr_L(0.764)$, $PAC_R(0.095)$, $OFC_R(0.084)$, $PuTl_R(0.077)$, $OFC_L(0.069)$, $OFC_R(0.068)$, $OFC_R(0.057)$, $VTC_L(0.05)$	$SNpr_L(0.764)$
$SNpr_R$	$SNpr_R(0.727)$, $VP_R(0.077)$, $PAC_L(0.069)$, $PMC_R(0.061)$, $OFC_R(0.059)$, $PC_R(0.058)$, $mPFC_R(0.058)$, $OFC_R(0.057)$, $PAC_R(0.057)$, $PMC_L(0.055)$, $OFC_L(0.053)$	$SNpr_R(0.727)$
$SNpc_L$	$SNpc_L(0.781)$, $OFC_R(0.135)$, $OFC_L(0.099)$, $PCL_R(0.076)$, $Ling_L(0.063)$, $VTC_L(0.06)$, $mPFC_L(0.06)$, $PC_L(0.054)$, $OFC_L(0.053)$, $PMC_R(0.053)$, $LatTl_L(0.051)$, $OFC_R(0.05)$	$SNpc_L(0.781)$
$SNpc_R$	$SNpc_R(0.754)$, $Ling_L(0.065)$, $mPFC_L(0.059)$, $mPFC_R(0.058)$, $OFC_R(0.057)$, $mPFC_R(0.057)$, $LatTl_L(0.056)$, $LatTl_R(0.056)$, $PMC_R(0.053)$, $mPFC_L(0.052)$	$SNpc_R(0.754)$
RN_L	$RN_L(0.768)$, $OFC_R(0.203)$, $mPFC_R(0.159)$, $Ling_L(0.105)$, $PVC_L(0.091)$, $mPFC_L(0.072)$, $Oper_L(0.062)$, $OFC_L(0.058)$, $PC_L(0.053)$, $mPFC_R(0.052)$	$RN_L(0.768)$, $RN_R(0.054)$
RN_R	$RN_R(0.765)$, $mPFC_L(0.114)$, $Ling_L(0.102)$, $mPFC_R(0.098)$, $mPFC_R(0.089)$, $mPFC_L(0.084)$, $Oper_L(0.082)$, $OFC_R(0.073)$, $VTC_R(0.06)$, $RN_L(0.054)$	$RN_R(0.765)$
DN_L	$DN_L(0.753)$, $OFC_L(0.108)$, $OFC_L(0.095)$, $Ling_R(0.075)$, $Oper_R(0.051)$, $OFC_L(0.051)$	$DN_L(0.753)$, $DN_R(0.099)$
DN_R	$DN_R(0.665)$, $DN_L(0.099)$, $OFC_L(0.075)$, $Ling_R(0.066)$, $OFC_L(0.062)$, $PVC_L(0.055)$, $Occ_L(0.051)$	$DN_R(0.665)$

Table 5.3: **Transmission of iron to/from deep grey nuclei, control population 1**. Predicted connections to and from deep grey nuclei regions for control population 1. Only connections greater than .05 are included.

Transmission of Iron To/From Deep Grey Nuclei, $p > .05$
Control Population 2

ROI	From x to ROI	To x From ROI
$NAcc_L$	$NAcc_L(.638), LatTl_R(.067)$	$NAcc_L(.638)$
$NAcc_R$	$NAcc_R(.693), Ling_R(.154), AntTl_L(.099), PC_L(.082), PC_R(.075),$ $mPFC_R(.059)$	$NAcc_R(.693),$ $ExtAmygd_R(.065)$
$ExtAmygd_L$	$ExtAmygd_L(.801), VTC_L(.118), SMA_R(.115), Temp_R(.103),$ $mPFC_R(.103), mPFC_L(.092), Occ_L(.089), IMTl_R(.086), PC_L(.062),$ $Amygd_L(.050)$	$ExtAmygd_L(.801)$
$ExtAmygd_R$	$ExtAmygd_R(.863), mPFC(.167), Amygd_L(.146), Ling_R(.140),$ $LatTl_L(.127), AntTl_L(.117), mPFC_R(.099), PC_L(.098), SMA_R(.089),$ $MedTl_R(.083), MedTl_L(.074), vlPFC_L(.069), IMTl_R(.068),$ $Amygd_R(.068), NAcc_R(.065), PVC_R(.062), Ling_L(.060), VTC_L(.051)$	$ExtAmygd_R(.863)$
$ExtGP_L$	$ExtGP_L(.790), Ins_L(.076), Amygd_L(.067), LaTl_L(.062), MedTl_R(.060),$ $Occ_R(.058), mPFC_R(.057), Amygd_R(.053), SMA_R(.052)$	$ExtGP_L(.790),$ $ExtGP_R(.060)$
$ExtGP_R$	$ExtGP_R(.743), MedTl_R(.114), LatTl_L(.081), Amygd_L(.077), SMA_R(.073),$ $mPFC_R(.070), Ling_L(.068), mPFC_L(.064), ExtGP_L(.060), OFC_L(.058),$ $Amygd_R(.057)$	$ExtGP_R(.743)$
$IntGP_L$	$IntGP_L(.757), CN_L(.061)$	$IntGP_L(.757),$ $IntGP_R(.099)$
$IntGP_R$	$IntGP_R(.695), IntGP_L(.099)$	$IntGP_R(.695)$
$SNpr_L$	$SNpr_L(.784), \quad VTC_L(.100), \quad SMA_R(.073), \quad VP_R(.071), \quad Ling_R(.059),$ $OFC_R(.052)$	$SNpr_L(.784)$
$SNpr_R$	$SNpr_R(.763), mPFC_R(.060)$	$SNpr_R(.763)$
$SNpc_L$	$SNpc_L(.783), LatTl_L(.091), Temp_R(.062), SMA_R(.061), Amygd_L(.058),$ $OFC_L(.057), VTC_L(.057), MedTl_L(.054)$	$SNpc_L(.783)$
$SNpc_R$	$SNpc_R(.744), LatTl_L(.091), Temp_R(.068), Hipp_L(.053), SMA_R(.053)$	$SNpc_R(.744)$
RN_L	$RN_L(.630), RN_R(.062)$	$RN_L(.630)$
RN_R	$RN_R(.690), DN_L(.061), mPFC_L(.053), OFC_L(.052)$	$RN_R(.690),$ $RN_L(.062)$
DN_L	$DN_L(.763), PC_L(.069)$	$DN_L(.763),$ $RN_R(.061)$
DN_R	$DN_R(.786), PVC_R(.065), PC_L(.061), OFC_L(.058)$	$DN_R(.786)$

Table 5.4: **Transmission of iron to/from deep grey nuclei, control population 2**. Predicted connections to and from deep grey nuclei regions for control population 2. Only connections greater than .05 are included.

(a)

(b)
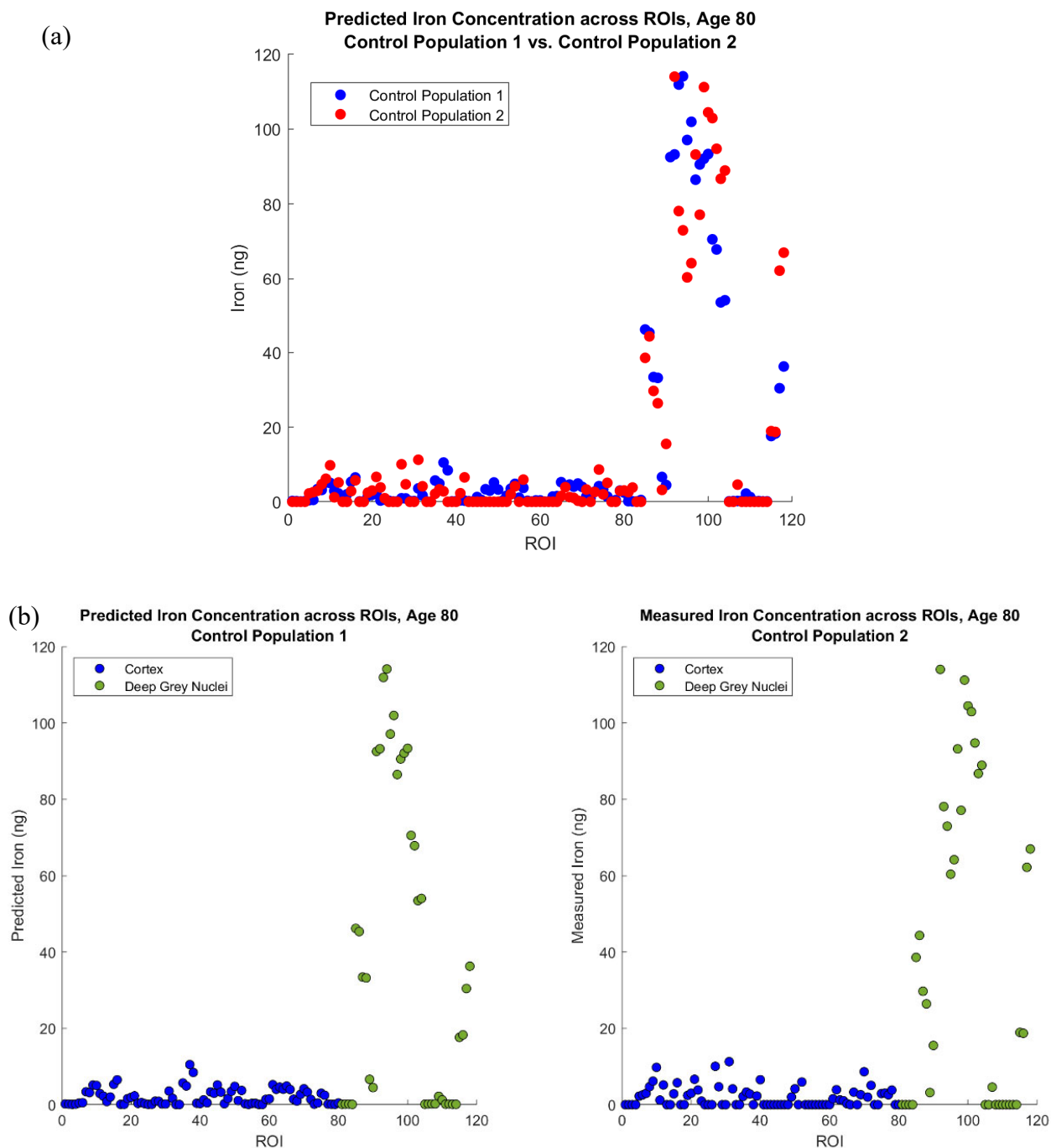
Figure 5.7: **Model prediction, comparison between two control populations**. The model prediction, when trained on QSM iron estimates from control population 1, is compared to QSM iron estimates taken from control population 2, distinct from the training dataset. The model prediction is (a) overlayed onto the testing dataset, and (b) side-by-side with the testing dataset, with cortical and grey matter nodes color-coded. The model prediction is the result of using the model and predicted Markov probability matrix to forward simulate to age 80 from an initial distribution set by the test set, age 30.

Training vs. Testing Error (ng Fe)
(1000 Bootstrap Resamples)

	Training	Testing
Mean	2.38	4.87
Standard Error	.080	.13

Table 5.5: **Training vs. testing error**. The training error for control population 1 was determined to be 2.38, and the testing error, when control population 2 was used as the test set, was found to be 4.87.

(a)
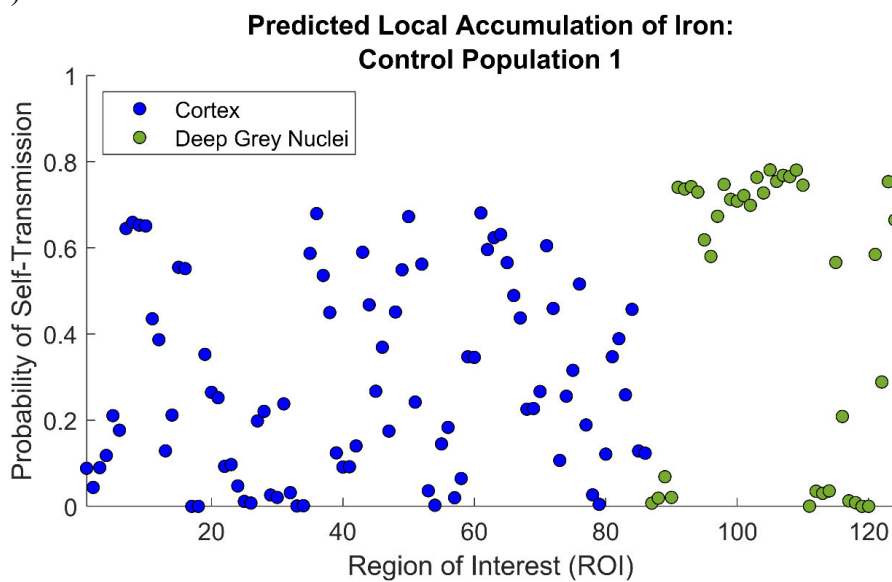
(b)
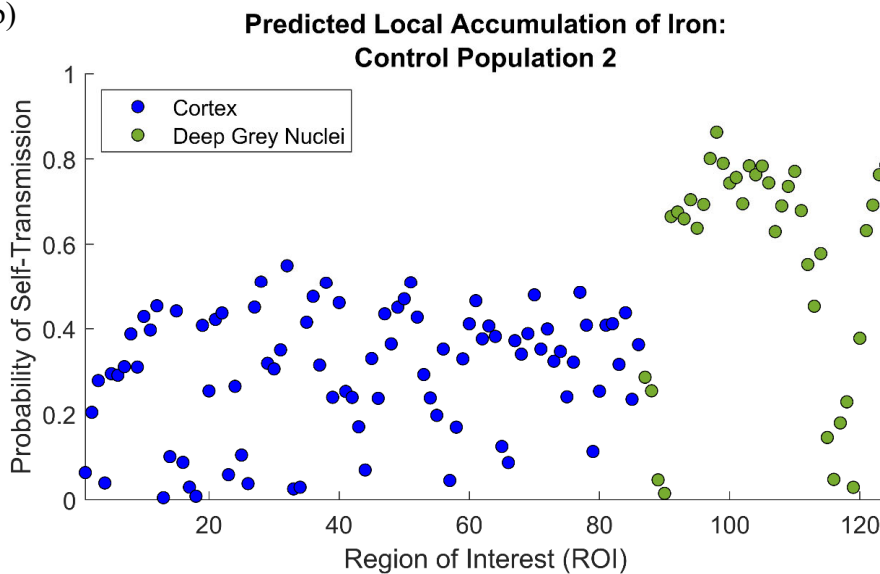
Figure 5.8: **Predicted local accumulation of iron**. Probability of self-transmission of iron to cortical and deep grey nuclei regions predicted for (a) Control Population 1, and (b) Control Population 2. For population 1, the mean local accumulation is .287 for cortical regions and .468 for deep grey nuclei regions. The standard deviation is .220 and .330, respectively. For population 2, the mean local accumulation is .301 for cortical regions and .561 for deep grey nuclei regions. The standard deviation is .146 and .261, respectively.

Figure 5.9: **Graph metrics for two control populations**. Number of in and out connections to cortical and deep grey nuclei regions predicted for (a) Control Population 1, and (b) Control Population 2. For population 1, the mean in-degree is 3.86 in the cortex and 6.63 in the deep grey nuclei. The standard deviation is 1.81 and 4.83, respectively. The mean out-degree is 4.30 in the cortex and 5.63 in the deep grey nuclei. The standard deviation is 2.31 and 4.62, respectively. For population 2, the mean in-degree is 15.57 in the cortex and 38.16 in the deep grey nuclei. The standard deviation is 4.72 and 20.82, respectively. The mean out-degree is 26.01 in the cortex and 14.53 in the deep grey nuclei. The standard deviation is 6.25 and 7.87, respectively.

Finally, we analyzed the similarities of the models trained on two distinct healthy populations by comparing graph metrics between the two. We focused on the predicted local accumulation of iron, or self-transmission, (See Fig. 5.8) and the predicted in-degree and out-

degree of nodes in the network (Fig. 5.9). In-degree refers to the number of connections pointing to a given node, and out-degree refers to the number of connections originating from a given node. These were determined after thresholding the Markov transition probability matrices at .008, which is equal to one divided by the total number of nodes (124). These analyses show that both models predict higher local accumulation in the deep grey nuclei than the cortex. They also both predict higher in-degree in the deep grey nuclei than the cortex. There are large differences in the mean values of the metrics between the two populations, which likely reflects high variability in the QSM data.

In order to assess the effect of reconstruction algorithm on the result, we retrained the model using QSM images from control population 2 reconstructed using the STAR-QSM algorithm. As described in 5.2, this was also used to reconstruct the QSM images for control population 1. We then repeated our analysis of graph metrics on this model. The results show that the reconstruction algorithm doesn't have much of an effect on the model prediction. The predicted local accumulation (Fig. 5.10) and degree (Fig. 5.11) across nodes is similar to that predicted for the same dataset reconstructed using the iLSQR algorithm (Fig. 5.8 and 5.9). This shows that our model is robust to the algorithm used for QSM reconstruction.

Figure 5.10: **Predicted local accumulation of iron: control population 2, STAR-QSM**. Probability of self-transmission of iron to cortical and deep grey nuclei regions predicted for control population 2, reconstructed with STAR-QSM. The mean local accumulation is .219 for cortical regions and .514 for deep grey nuclei regions. The standard deviation is .162 and .298, respectively.
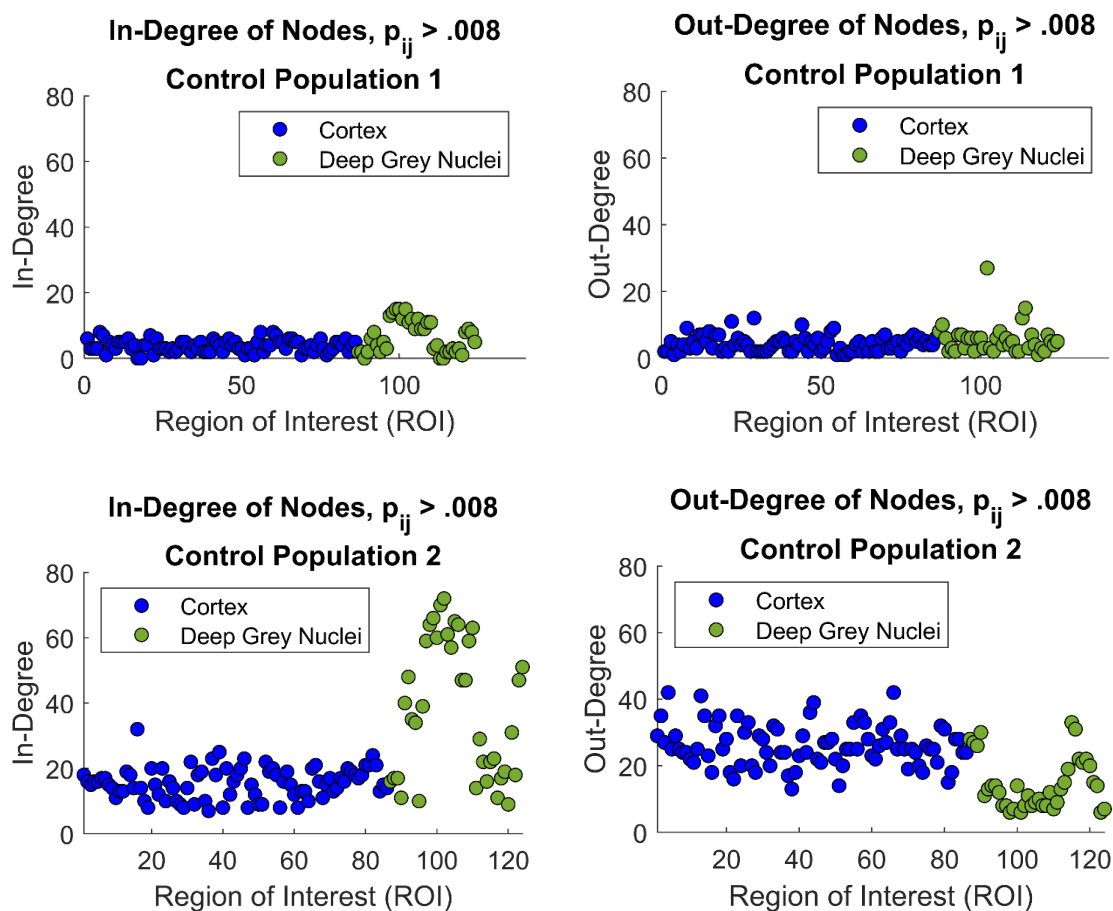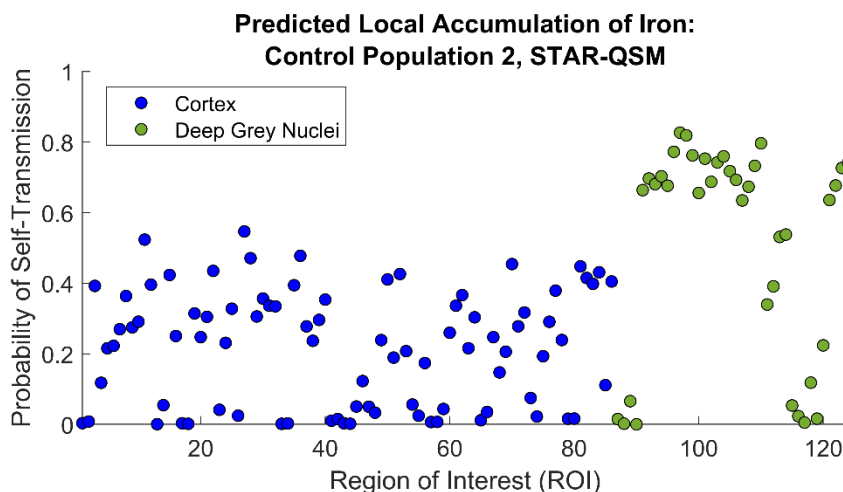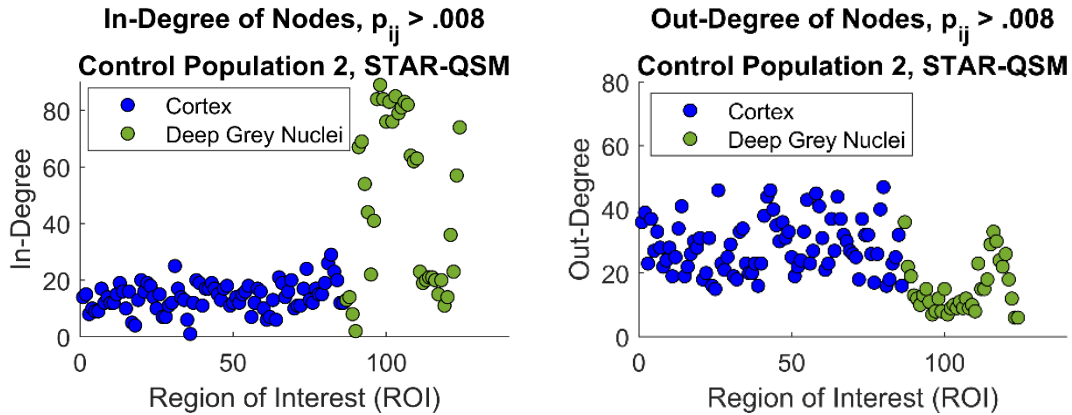
Figure 5.11: **Graph metrics for control population 2, STAR-QSM**. Number of in and out connections to cortical and deep grey nuclei regions predicted for control population 2, reconstructed with STAR-QSM. The mean in-degree is 14.16 in the cortex and 47.34 in the deep grey nuclei. The standard deviation is 5.05 and 29.23, respectively. The mean out-degree is 28.43 in the cortex and 15.05 in the deep grey nuclei. The standard deviation is 8.36 and 7.91, respectively.

5.4   Discussion

Our results show that our Markov model is able to accurately predict the spatial-temporal dynamics of iron in the brain, when model parameters are estimated from QSM iron estimates following the active transport hypothesis. The model prediction is accurate even when compared to QSM iron estimates taken from a population separate from the training dataset. Additionally, the results of our comparison analysis between two control populations show that our model prediction is robust. The network figures illustrate that the predicted transmission of iron between regions is similar between the two populations. Particularly, both networks predict connections between deep grey nuclei regions like the ExtAmygd, GP, SN, RN, and nucleus accumbens (NAcc) and the same cortical regions. Also, both networks predict connections between the DN and multiple similar cortical regions, as well as connections of high probability between the same deep grey nuclei (NAcc, ExtAmygd, GP and SN) and the Tl. We further examined the predicted network and found many of the connections to be supported by previous experimental results.

The primary mechanisms by which the model explains iron accumulation in the deep grey nuclei are local accumulation and degree of connections. The model predicts a higher probability of self-transmission, or local iron accumulation, in the deep grey nuclei than in the cortex. There are several processes which could account for this. First, oligodendrocytes and microglia are known to be present in higher numbers in the deep grey nuclei than the cortex and both of these have been implicated in iron storage and homeostasis [89], [98], [156]. The results from our analysis in Chapter 2 show that oligodendrocytes may be the source of the increased

positive QSM signal in regions of high iron. This is supported by histology studies in rats [156] which show that the increased ferritin and iron in the SN of aging rats is localized to oligodendrocytes and microglia, not neurons. Microglia highly express Ftn and are thought to uptake iron via Ftn or DMT1, potentially releasing iron for uptake by oligodendrocytes [94], [156]. This may be a pathway of ageing-associated local accumulation of iron, as predicted by our mathematical model.

Another source of local accumulation of iron may be changes in iron transporter expression. Lu et al. [162] have found that aging alters the expression of several iron transporters in specific regions of the rat brain, including the striatum, Hipp, SN, and cortex. Additionally, the blood brain barrier (BBB) shows an increased permeability with age, and this has been linked to brain iron deposits through the upregulation of hepcidin, an iron regulatory protein [163]. Increased hepcidin expression has been observed in the brain of aging mice and has been shown to be correlated with decreased levels of Fpn [163]. There are regional differences in BBB permeability seen in aging, as well as various disorders [139]. Both of these inter-dependent mechanisms could result in alterations to the local accumulation of iron or to the iron transport dynamics between regions.

Our model predicts deep grey nodes to have more connections to them and fewer connections outside of them, which could explain iron accumulation. The deep grey nuclei are highly connected by axons to the cortex and among each other [164], [165]. It is possible that iron may be transported into the deep grey nuclei along these routes, and studies demonstrating axonal transmission of iron and the presence of Fpn in synaptic vesicles have bolstered this claim [37], [106], [144]. It's unclear why the node degrees is so different between the two healthy populations. Possibly the model is predicting a lot of smaller, spurious connections contributing to this difference.

We analyzed some of the predicted connections and found several that are consistent with previous experimental results. Specifically, [106] found two axonal pathways of iron transport in the mouse brain: vHip to mPFC to SN, and Tl to Amygd to mPFC. Our results predict transmission of iron along both of these pathways. In terms of the first pathway, our model predicts iron transmission from the mPFC to both the left and right SN pars reticulata (SNpr) with relatively high probability compared to other predicted pathways, as well as transmission from the Hip to the SN pars compacta (SNpc). Finally, there is also a predicted connection from the ventral pallidum (VP), which is an intermediary connection between the mPFC and SN in certain neural pathways in the mouse brain and was not analyzed in the [106] experiment, to the SNpr. Our model predicts connections that support the second pathway as well, predicting transmission of iron from the Tl (lateral and medial) to the Amygd and the Amygd to the mPFC. This indicates that the network predicted by our model is plausible.

Finally, our model predicts transmission that suggests transport of iron through the CSF. The Amygd is directly adjacent to the lateral ventricle on either hemisphere of the brain [5]. Interestingly, our model predicts transmission of iron between the right and left Amygd, which could be explained physically by CSF transport. We also see predicted transmission between the

left and right of other deep grey matter regions. Autoradiographic experiments have been done that inject radio-labelled iron into the ventricle on only one side of the brain and the resulting iron is seen to accumulate in the typical deep grey matter regions of both hemispheres [105]. This points to iron being transported across hemispheres through the CSF and could explain the results we're seeing in our model's predictions. This may be facilitated by Tf, which has been found to be fully saturated with iron in the CSF [22]. That our model's predictions can be plausibly explained by pathways involving iron transporters corroborates our active transport hypothesis.

5.5 Limitations

Although our results are promising, there are several limitations of our modeling approach. In Ch. 4, we determined that passive diffusion alone is not sufficient to explain iron accumulation in the aging brain, however, several studies support the theory of iron transport along axons, which follows passive diffusion gradients in the brain [106], [143], [144]. A passive diffusion term could be added to our model, in addition to the Markov transition probability matrix resting on the assumption of active transport. We also didn't make the source term time-dependent although there is evidence for age-associated BBB leakage, so the model may be compensating for this by predicting spurious connections between nodes [141], [166]. Potentially incorporating time-dependency into the source term could change the predicted network. We didn't consider alternative segmentations for defining nodes in the network, and registration errors are likely contributing to the variability of our results. Although these changes may improve our model's performance and interpretability, we acknowledge a tradeoff between model complexity and data availability that must be navigated.

        We are also limited by the QSM measurement, which is not real-time. The two healthy QSM datasets are reconstructed using different algorithms. We used STAR-QSM to reconstruct the QSMs for control population 1, which may result in underestimated values [71], [157]. However, we showed that the model prediction is similar for control population 2 when reconstructed with both iLSQR and STAR-QSM. Finally, QSM is only an accurate estimate of iron in regions where iron dominates the susceptibility signal. We address this in the next chapter by using an algorithm to decompose the QSM signal into positive and negative susceptibility components.

5.6 Conclusion

In conclusion, we've shown that our Markov model of iron transport, when transition probabilities are estimated from QSM following the active transport hypothesis, accurately predicts the distribution of iron across time and space in the brain. These results support the active transport hypothesis of brain iron transport. Our model not only offers insights into the

basic biological mechanisms of iron homeostasis in the brain, but also holds significant promise for understanding neurodegenerative disorders like Alzheimer's, which are hallmarked by altered iron transport dynamics.

Chapter 6

Estimating Markov Transition Probabilities using QSM-DECOMPOSE

6.1   Introduction to DECOMPOSE

QSM is limited as a measurement of iron in that its relationship to iron concentration is only established in the deep grey nuclei [25]. Other regions of the brain, particularly the white matter and cerebellum, contain diamagnetic species that contribute negative susceptibility to the QSM signal, obscuring the positive susceptibility signal from iron [6], [19], [51]. Iron in the cortex may also be obscured by diamagnetic species, as it is not present in as high amounts as in the deep grey nuclei [19], [88]. Myelin is diamagnetic and therefore can drown out the positive susceptibility signal from iron in the cortex [61]. Changing levels of diamagnetic species may further compromise the use of QSM as an estimate of iron. For instance, demyelination that can be seen in aging results in a higher QSM signal, inaccurately drawing the conclusion of a higher iron estimate [167]. For these reasons, QSM as an iron estimate has several limitations, and it would be beneficial to consider an alternative iron estimate for use in our model. For this, we turn to paramagnetic component susceptibility (PCS) maps calculated by separating the QSM signal into its positive and negative susceptibility contributions.

We use diamagnetic component and paramagnetic component separation, or DECOMPOSE-QSM, an algorithm developed by Jingjia Chen et al., to break the QSM signal in each voxel into its positive and negative susceptibility components [130]. PCS is an improvement on the iron estimation from QSM since it maps the paramagnetic species only, of which iron is the major contributor [51], [130]. In addition, this allows us to expand the network in our model to include regions in the cerebellum and white matter as nodes. After training our model with PCS, we observed higher accuracy in terms of the training error, and the effect is improved when cerebellar and white matter regions are used as nodes in addition to grey matter regions. This exciting result points to the potential of PCS as an estimate of iron in the brain that overcomes several of the limitations of QSM.

6.2   Methodology

We reconstruct paramagnetic component susceptibility (PCS) maps for a healthy QSM dataset (the second healthy control population described in Ch. 5) using the DECOMPOSE-QSM algorithm described in [130]. The multi-echo gradient echo signal is modeled as a weighted sum of three signal sources, resulting from paramagnetic, diamagnetic, and magnetically neutral species. Here, neutral refers to susceptibility signal that is equal to the reference susceptibility of the image. Each signal source is modeled as a complex exponential characterized by the R2* decay and frequency shift resulting from the susceptibility species within each voxel. These parameters, and the weights on each component, are solved from the QSM and magnitude measurement of each echo. From there, the PCS maps can be constructed by substituting the parameters into the complex exponential model for the paramagnetic component.

We compare the results for our model when trained using both the PCS and QSM iron estimates calculated for the same set of healthy subjects, labelled Control Population 2 in Chapter 5. Chapter 5 describes the QSM reconstruction, registration, and calculation of average QSM across regions of interest (ROIs) for this population. We use the same registrations and method to calculate the average PCS across ROIs, and these values are converted to iron concentration estimates using the relationship from [25], reported in equation 3.9. The subjects are partitioned into bins of 5 years based on age, and then averaged together to yield an estimate of the PCS over time. Finally, this pseudo-real-time signal is then interpolated to a time scale of one year. This procedure is the same as that used in Ch. 5 for the QSM subjects. The set up of the optimization problem is also identical to that described in Ch. 5, however, we use regions in the white matter and cerebellum as nodes, in addition to grey matter regions. We again perform hyperparameter optimization using grid search before solving for the Markov transition probability matrix with 1000 bootstrap resamples. As in Ch. 5, one subject is left out of each age bin at random for each bootstrap run, and then the predicted Markov matrices are averaged across all runs.

6.3   Results

We see a decrease in some regions and an increase in others when comparing the PCS iron estimate to the QSM iron estimate. In particular, the iron estimate is increased in the cerebellum, cortex, and white matter when using PCS. However, the iron estimate is decreased in the deep grey matter areas compared to the QSM estimate, which likely indicates registration errors. Despite this, we see an increased performance in our model prediction accuracy, as measured by training error (Eq. 5.4), when using the PCS iron estimate, compared to the QSM iron estimate. Additionally, the accuracy is further improved when using cerebellar and white matter regions as nodes, in addition to grey matter regions.
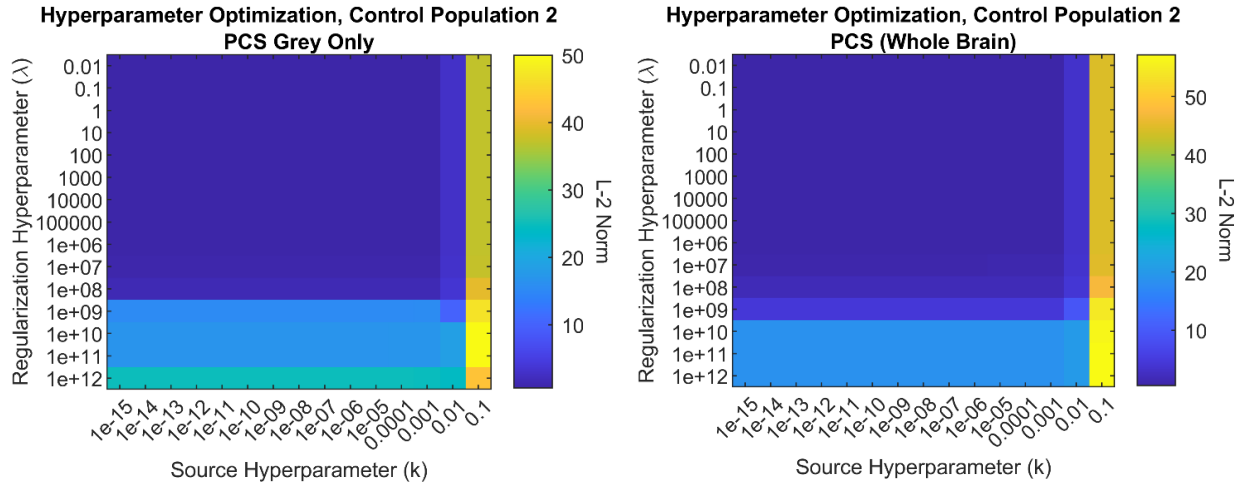
Figure 6.1: **Hyperparameter Optimization**. We define a logarithmic grid of the hyperparameters k and λ to include the values that yield a nil solution, set up the optimization problem for each pair of values and then solve for the Markov probability transition matrix. The optimal hyperparameters are the values of k and λ that minimize the L-2 norm term in the cost function of the optimization problem.

We performed a one-way analysis of variance (ANOVA) comparing the mean training error calculated over 1000 bootstrap runs for three training datasets: QSM (grey matter nodes only), PCS (grey matter nodes only), and PCS (whole brain). There are two degrees of freedom between groups and 2997 degrees of freedom within groups. The F-statistic is 14,595 and the resulting p-value is .000, indicating that the difference between means is significant (Fig. 6.3). These results show that the model prediction is more accurate when PCS is used as an iron estimate, and even more so when cerebellar and white matter regions are used as nodes in addition to grey matter regions.

We calculated the same graph metrics considered in Ch. 5, predicted local accumulation of iron and the number of connections entering and leaving each node (calculated for the average Markov probability matrix of 1000 bootstrap resamples, thresholded at .008). We report the results for the model trained using PCS iron estimates and cerebellar and white matter regions as nodes in addition to grey matter regions, as this was the model with the lowest training error. As with the model trained using QSM iron estimates, we again see higher in-degree (20.74) and lower out-degree (9.68) of deep grey nuclei regions, compared to other regions of the brain. We observed in-degrees of 9.31, 10.76, and 9.06 and out-degrees of 12.08, 12.47, and 13.25 for nodes in the cerebellum, cortex, and white matter, respectively. There is also slightly higher local accumulation predicted in the deep grey nuclei (.678) than other regions (.615, .622, and .549 in the cerebellum, cortex, and white matter). Interestingly, the predicted local accumulation of all regions is high, including the white matter, although there is a lot of variation among nodes. The means and standard deviations of these metrics are reported in Tables 6.1 and 6.2.
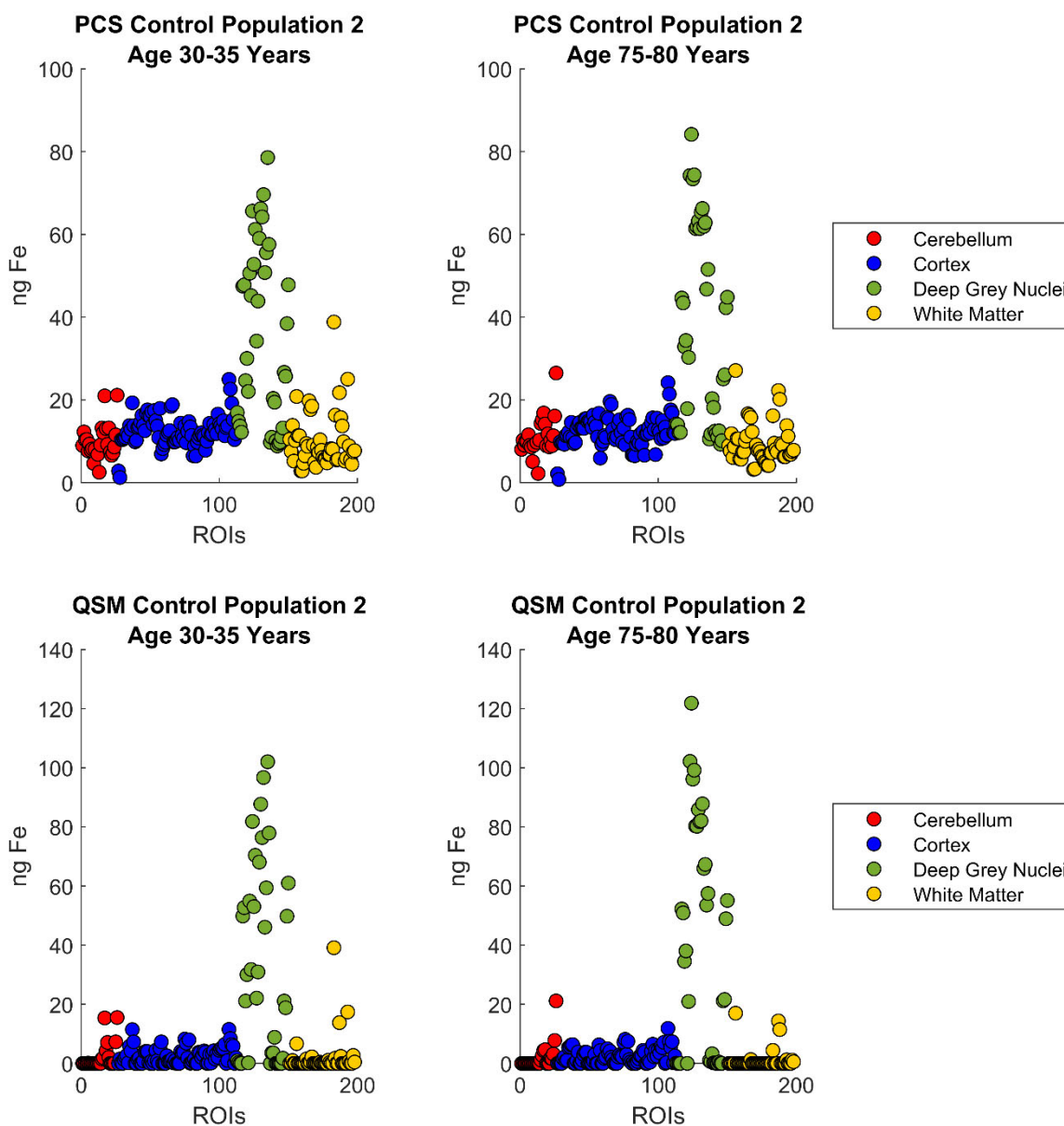
Figure 6.2: **PCS iron estimate vs. QSM iron estimate**. Iron estimates calculated from PCS and QSM reconstructed for the same set of healthy subjects (control population 2, described in Ch. 5). Note that PCS in the cerebellum, cortex, and white matter is larger than QSM in those same regions, illustrating that PCS can discern the positive susceptibility contributions of species in those regions, an improvement over QSM.
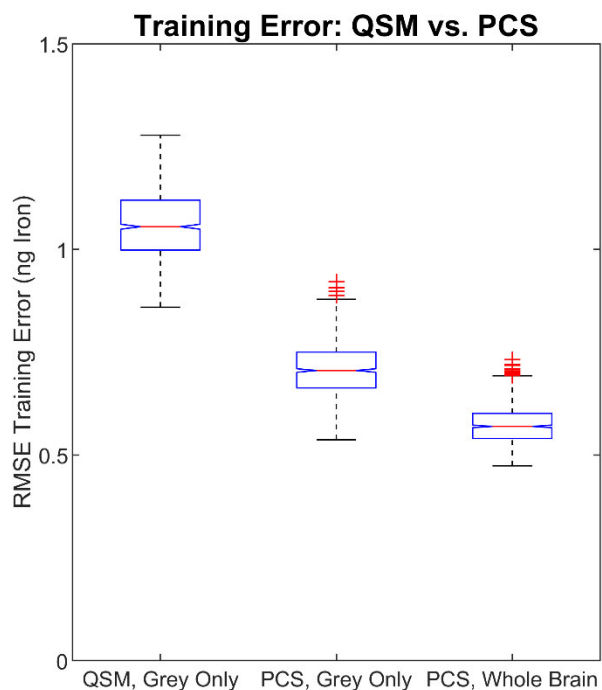
Figure 6.3: **Training error: QSM vs. PCS**. One-way analysis of variance (ANOVA) comparing the mean training error over 1000 bootstrap runs between three training datasets: QSM (grey matter nodes only), PCS (grey matter nodes only), and PCS (whole brain). The degree of freedom is two between groups and 2997 within groups. The F-statistic is 14,595 and the resulting p-value is .000, indicating that the difference between means is significant.
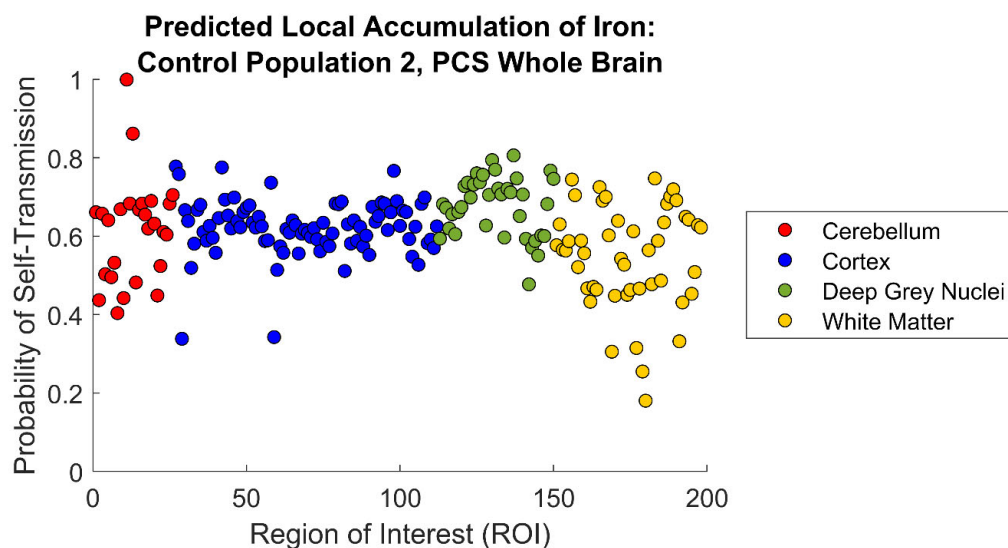
Figure 6.4: **Predicted local accumulation of iron: control population 2, PCS whole brain**. Our model, when trained using PCS iron estimates with all brain regions as nodes, predicts slightly higher local accumulation of iron in the deep grey nuclei.
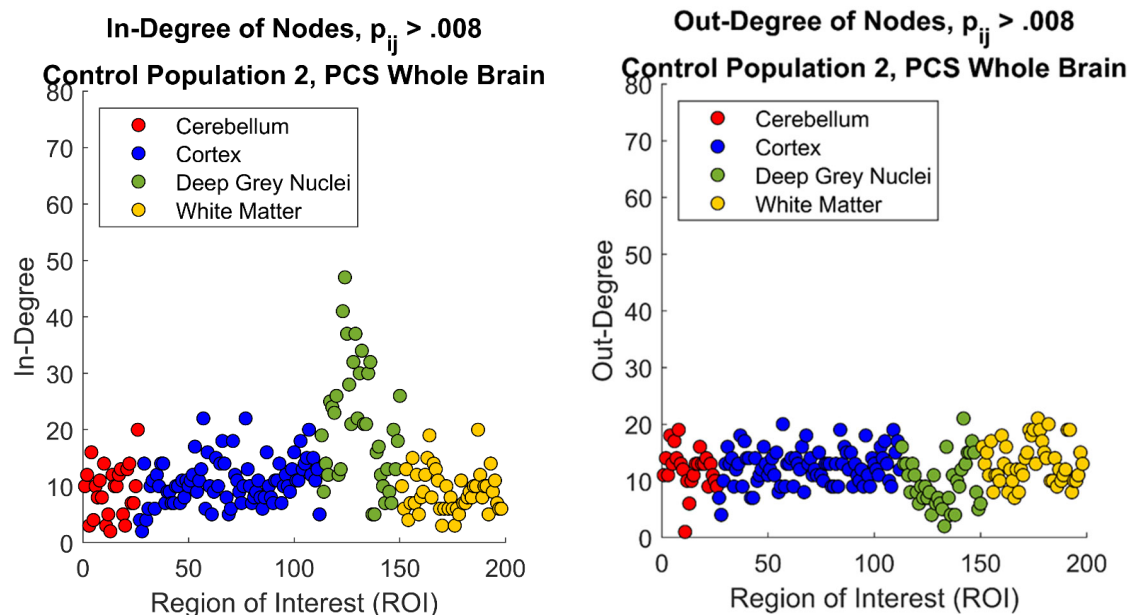
Figure 6.5: **Degree of nodes: control population 2, PCS whole brain**. Our model, when trained using PCS iron estimates with all brain regions as nodes, predicts higher in-degree and lower out-degree of nodes in the deep grey nuclei.

Degree of Nodes:
Control Population 2, PCS Whole Brain

In-Degree				
	Cerebellum	**Cortex**	**Deep Grey**	**White Matter**
Mean	9.31	10.76	20.74	9.06
Standard Dev	4.52	3.98	10.58	3.76
Out Degree				
	Cerebellum	**Cortex**	**Deep Grey**	**White Matter**
Mean	12.08	12.47	9.68	13.25
Standard Dev	3.67	3.10	4.34	3.73

Table 6.1: **Degree of nodes: control population 2, PCS whole brain**. In-degree and out-degree calculated for nodes in the cerebellum, cortex, deep grey nuclei, and white matter.

Local Accumulation of Iron:
Control Population 2, PCS Whole Brain

	Cerebellum	**Cortex**	**Deep Grey**	**White Matter**
Mean	.615	.622	.678	.549
Standard Dev	.133	.071	.075	.132

Table 6.2: **Local accumulation of iron: control population 2, PCS whole brain**. Predicted probability of self-transmission for nodes in the cerebellum, cortex, deep grey nuclei, and white matter.

6.4 Discussion

Our results show a decrease in the training error when our Markov model is trained using PCS, and a further decrease when using all regions in the brain as nodes. This increase in accuracy may indicate that PCS is an improved iron estimate over QSM, and this is supported by comparing the distributions of the corresponding iron estimates of the two modalities across the whole brain. Using QSM as iron estimate results in near-zero levels of iron in the cortex, which is not supported by dissection and histology studies showing iron in these regions [6], [42], [88]. This discrepancy is because we are fundamentally limited in extrapolating QSM as an estimate of iron in the whole brain as the relationship between the susceptibility signal and iron concentration is only significant in the deep grey regions [25]. Several other studies have bolstered the claim that this relationship is due to the high levels of iron dominating over susceptibility contributions from other sources [6], [42], [46], [51]. Additionally, the QSM signal is negative in many regions of the cerebellum and white matter, which would result in a nonsensical iron estimate in these regions using the [25] relationship. The PCS signal is most certainly an improvement over QSM in these regions as it predicts non-zero concentrations of iron, which is consistent with histology studies [6], [88], [156].

The use of PCS to expand the network model to include cerebellum and white matter as nodes leads to some interesting insights. We observe our model to be predicting white matter nodes to have higher out-degree and lower accumulation of iron than other regions. This seems to support the axonal transport theory of iron, as it indicates our model is predicting higher turnover of iron in these regions, as well as high connectivity of the white matter to other nodes [37], [106], [144]. Also, our results show that the model again explains iron accumulation in the deep grey matter by predicting higher self-transmission of iron and more connections to these regions, even when the cerebellum and white matter are included as nodes. This is consistent with our results from Ch. 5, when the model was trained with QSM iron estimates.

Our results support the findings that PCS is a reliable estimate of iron in the brain [130]. This is especially applicable for situations where the QSM signal is known to be compromised by disease pathology, as in Alzheimer's disease (AD). For instance, two hallmarks of AD pathology, tau protein aggregation and amyloid beta plaque deposition, are diamagnetic and their accumulation can lead to a reduction of the QSM signal, obscuring the paramagnetic susceptibility signal from iron [30], [31], [168]. This is further complicated by evidence that implicates excess brain iron and altered iron transport dynamics in the progression of AD [30], [42], [168], [169]. In the next chapter, we explore using our model to predict altered iron transport dynamics in AD using both QSM and PCS as iron estimates.

6.5   Limitations

We are limited in this analysis by the availability of PCS data. One possible interpretation of our results is that the use of PCS and regions outside the grey matter as nodes can be explained by overfitting. It would be interesting to examine this further by testing the model prediction against a second population, as we did in Chapter 5 for the QSM-trained model. Also, our calculations of the average PCS across regions in the brin show that registration errors are affecting our iron estimates. This can be seen in the deep grey nuclei, which shows lower iron estimates from PCS than from QSM, which cannot be explained biologically. A more thorough survey of registration methods is needed to address this problem.

6.5   Conclusions

We have shown PCS to be an improvement over QSM as an iron estimate in our model, in that it allows us to expand our model to include cerebellar and white matter regions as nodes, resulting in better model performance. This is especially promising for studying altered iron transport dynamics in AD, which is hallmarked by proteins that complicate the use of QSM as an estimate of iron in the brain. We explore this application of our model in the next chapter.

Chapter 7

Application of Markov Model to Understanding Altered Iron Transport Dynamics in Alzheimer's Disease

7.1   Iron Transport and Implications for Alzheimer's Disease

Alzheimer's disease is a devastating neurodegenerative disorder that causes dementia and progressive loss of cognition [169]. Altered iron homeostasis is well-documented in Alzheimer's disease and other neurodegenerative disorders [30], [33], [42], [169], [170]. Excess iron, when unbound in the cell, is highly reactive and can lead to the proliferation of cytotoxic reactive oxygen species in a molecular cascade known as the Fenton reaction [29], [42]. Many of the deep nuclei regions that accumulate iron in normal aging are hallmarked by neurodegenerative damage in disorders like AD and PD, and they show even further elevated levels of iron beyond what is normal for healthy aging [29], [30], [42], [171]. Various studies have proposed using elevated iron levels in the basal ganglia as a potential diagnostic biomarker for AD, particularly in the early stages of the disease [30], [31], [171]. There is also evidence for increased iron accumulation in the hippocampus and the cortex in AD, and iron-overload associated oxidative stress is thought to be involved in the neurodegenerative cascade [169].

The involvement of iron in AD extends beyond the Fenton reaction. Iron is thought to be involved in the formation of both pathologies characterizing AD, amyloid beta plaques and tau neurofibrillary tangles [30], [168], [172], [173]. The deposition of these proteins is implicated in the neuronal damage seen in the progression of the disease [31], [168], [169]. Iron has been found to co-localize with sites of amyloid beta plaque deposition in AD and is also likely involved in the aggregation of tau [30], [173]. Increased iron deposition in these areas has also been found to correlate with disease severity [30]. This excess iron is thought to be implicated in the process of neurodegeneration itself.

All of this points to the importance of understanding iron transport dynamics for both the diagnosis and treatment of AD. Our Markov model of brain iron transport has shown promise in predicting iron transport dynamics when trained on both QSM and PCS iron estimates from a healthy population. We attempt to explore the relationship between altered iron transport dynamics and AD disease progression by training our Markov model of iron transport using QSM and PCS iron estimates measured for subjects with AD.

7.2 Methodology

The AD dataset consists of QSM and PCS maps for 125 subjects, both male and female, aged 46 to 90, collected by [31]. 56 of these were diagnosed with AD and 69 with mild cognitive impairment (MCI). The QSMs were collected and reconstructed in the same manner as for control population 2 (described in Ch. 5). The AD subjects were registered using Advanced Normalization Tools (ANTs) to the same age-specific QSM group atlases used in Chapters 5 and 6, and the calculation of the iron estimate from the QSM is the same as described in these chapters [20]. Similarly, PCS maps and the average PCS across brain regions were calculated as described in Ch. 6.

The problem set up is the same as in Chapter 5. We use the iron estimates for control population 2, described in Chapter 5, and for the AD population processed in the same manner. We again use only grey matter regions as nodes for the model trained from the QSM iron estimate, as the QSM signal is limited for other regions. However, we expand the model to include cerebellar and white matter regions as nodes when using the PCS iron estimate. As in Ch. 5, the AD subjects are partitioned into 5 year age bins, averaged, and then the resulting signal interpolated to a temporal resolution of one year. Next, we resample both populations, randomly selecting the same number of subjects from each age bin in order to make the two age distributions comparable. This means the number of measurements and the age range used from control population 2 in our analysis in this chapter is different than those used in Ch. 5, which were matched to control population 1.

We then set up the same optimization problem (Eq. 5.3) for the resampled control population 2 and AD iron estimates and solve for the optimal hyperparameters for each population using grid search. Finally, we solve for the Markov transition probability matrix of each population with 1000 leave-one-out bootstrap resamples, as in Ch. 5. The predicted Markov matrices are then averaged over all bootstrap runs. We repeat this process using PCS iron estimates for both populations, however, using cerebellar and white matter regions as nodes, in addition to grey matter regions.
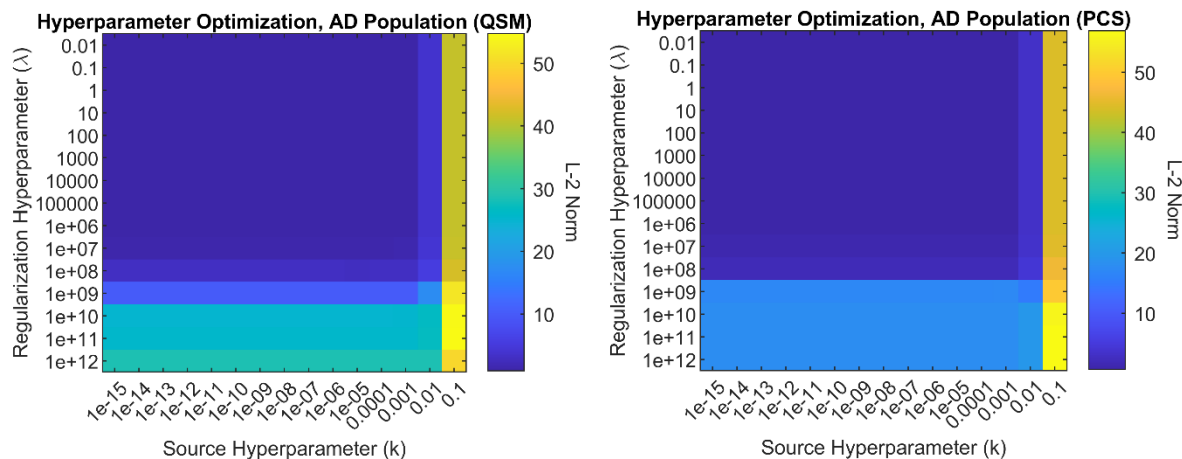
Figure 7.1: **Hyperparameter Optimization**. We define a logarithmic grid of the hyperparameters k and λ to include the values that yield a nil solution, set up the optimization problem for each pair of values and then solve for the Markov probability transition matrix. The optimal hyperparameters are the values of k and λ that minimize the L-2 norm term in the cost function of the optimization problem.

7.3   Results: Changing Iron Dynamics in AD

Our results show that our model is successful in predicting altered iron transport dynamics for the AD population, using both the QSM and PCS iron estimates. This is evident by the low training error observed for each model over 1000 bootstrap resamples, 1.20 ng Fe (standard error .018) and .61 ng Fe (standard error .0029), respectively.

7.3.1 QSM iron estimate

Focusing on the basal ganglia regions, we see lower iron levels in the globus pallidus (GP) and caudate nucleus (CN), and higher iron in the putamen (Pu) at age 80 in the AD population, as compared to the healthy controls. This is again observed in our model prediction. Figure 7.2 depicts the model prediction and the QSM iron estimate used as training data in the left basal ganglia regions for both the healthy population (control population 2) and the AD population. The model prediction is the result of forward simulating 35 years from an initial distribution set by the training data at age 45 (Eq. 4.5).
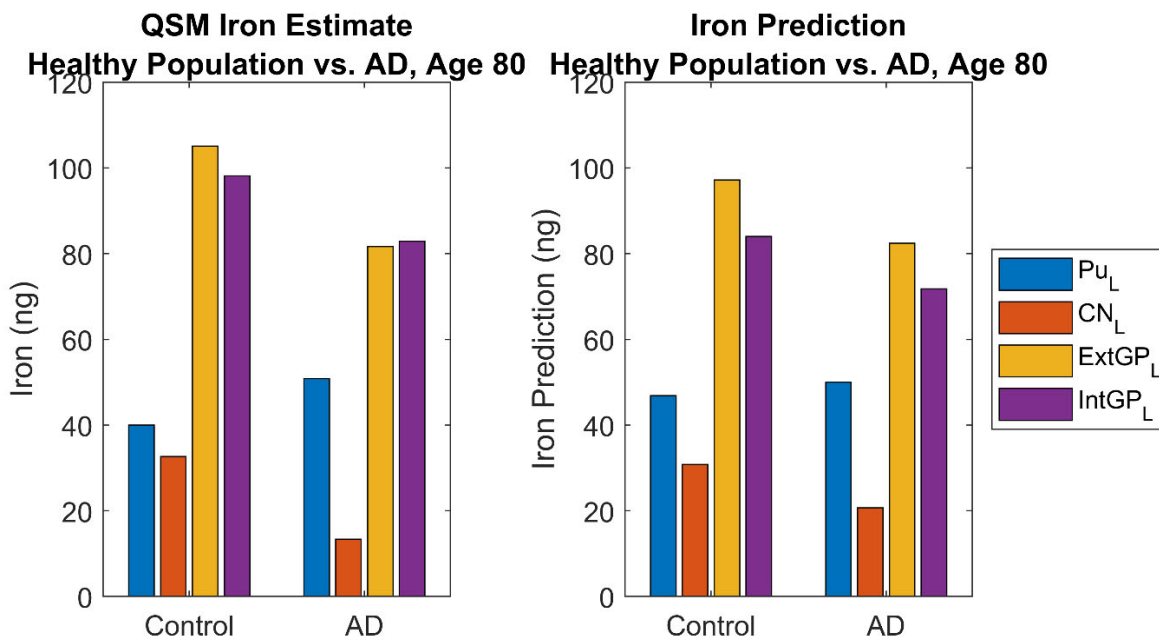
Figure 7.2: **Model prediction of altered iron deposition in the basal ganglia in AD**. The observed iron concentrations in basal ganglia regions in AD brains are different than in those of normal controls. The model prediction is determined by forward simulating 35 years from an initial distribution set by the training dataset at age 45. Our model successfully predicts altered iron transport dynamics in these regions.

Interestingly, our model predicts different transmission pathways to and from the basal ganglia when trained on QSM iron estimates from the AD population, compared to the model trained with the control dataset. The transmission pathways predicted for these regions with probability greater than .05 in both models are reported in Tables 7.1 and 7.2, respectively. Further study is required to untangle the specific differences between the predicted pathways.

Finally, we assess the graph characteristics of each predicted model using the same procedure as described in Ch. 5 and 6. There doesn't appear to be much change in the predicted local accumulation (probability of self-transmission) between the two populations: mean values of .198 and .544 in the cortex and deep grey nuclei for the control population and .181 and .540 for the AD population (see Fig. 7.3 and Table 7.3). The node degree for each population is summarized in Fig. 7.4 and Table 7.4. The grey matter regions show higher in-degree for the AD population than the control population (33.11 vs. 26.30) however, this difference was not found to be statistically significant. The out-degree of deep grey regions is comparable for both populations (9.29 for control and 9.87 for AD), as is the in-degree and out-degree of cortical regions (5.72 and 13.23 in-degree and out-degree, respectively, for control and 5.65 and 15.92 for AD).

Transmission of Iron To/From Deep Grey Nuclei, $p > .05$
Control Population 2

ROI	From x to ROI	To x From ROI
Pu_L	$Pu_L(0.746)$, $IPL_L(0.166)$, $PAC_R(0.162)$, $OFC_R(0.088)$, $mPFC_L(0.069)$, $PuTl_R(0.06)$, $OFC_L(0.054)$, $RN_R(0.042)$, $NAcc_R(0.033)$, $IPL_L(0.029)$, $mPFC_R(0.02)$, $mPFC_R(0.019)$, $Temp_R(0.018)$, $mPFC_R(0.016)$, $PuTl_L(0.016)$	$Pu_L(0.746)$, $Pu_R(0.085)$, $CN_L(0.032)$, $ExtAmygd_R(0.03)$, $CN_R(0.017)$, $PAC_R(0.013)$, $mPFC_R(0.012)$
Pu_R	$Pu_R(0.706)$, $mPFC_R(0.134)$, $OFC_R(0.123)$, $Temp_R(0.093)$, $Pu_L(0.085)$, $PAC_R(0.071)$, $PuTl_R(0.057)$, $IPL_L(0.044)$, $mPFC_L(0.04)$, $NAcc_R(0.028)$, $CN_R(0.017)$, $ITC_R(0.017)$, $VTC_L(0.017)$, $VTC_L(0.017)$, $PuTl_L(0.016)$	$Pu_R(0.706)$, $Occ_L(0.027)$, $CN_R(0.022)$, $SubTl_R(0.021)$, $CN_L(0.021)$, $ITC_L(0.02)$, $ITC_R(0.015)$, $Pu_L(0.012)$, $SubTl_L(0.012)$, $Occ_R(0.011)$, $PuTl_L(0.011)$, $Temp_R(0.01)$, $vlPFC_R(0.009)$
CN_L	$CN_L(0.729)$, $CN_R(0.05)$, $ITC_R(0.038)$, $PAC_R(0.036)$, $Pu_L(0.032)$, $OFC_R(0.028)$, $Pu_R(0.021)$, $mPFC_L(0.018)$, $RN_R(0.014)$, $Occ_R(0.012)$, $ExtGP_R(0.009)$	$CN_L(0.729)$, $SubTl_R(0.051)$, $vlPFC_L(0.021)$, $SubTl_L(0.02)$, $ITC_R(0.019)$, $IntGP_L(0.016)$, $ExtGP_L(0.015)$, $CN_R(0.01)$, $IntGP_R(0.01)$, $Occ_R(0.009)$, $IPL_R(0.009)$
CN_R	$CN_R(0.758)$, $OFC_R(0.032)$, $ITC_R(0.025)$, $PuTl_R(0.025)$, $Pu_R(0.022)$, $mPFC_R(0.02)$, $RN_R(0.02)$, $PuTl_L(0.019)$, $Pu_L(0.017)$, $SNpr_L(0.014)$, $OFC_L(0.013)$, $IPL_L(0.012)$, $VTC_L(0.01)$, $CN_L(0.01)$, $OFC_R(0.009)$	$CN_R(0.758)$, $CN_L(0.05)$, $ITC_R(0.022)$, $Pu_R(0.017)$, $vlPFC_L(0.015)$, $ExtGP_L(0.015)$, $Pu_L(0.013)$, $ITC_L(0.012)$, $ExtGP_R(0.011)$, $ExtAmygd_L(0.01)$, $PAC_R(0.01)$
$ExtGP_L$	$ExtGP_L(0.859)$, $Occ_L(0.128)$, $Occ_R(0.124)$, $ITC_R(0.122)$, $ITC_L(0.115)$, $Occ_R(0.098)$, $mPFC_R(0.082)$, $vlPFC_R(0.068)$, $mPFC_L(0.047)$, $SubTl_L(0.026)$, $SPL_L(0.023)$, $IPL_L(0.021)$, $PMC_R(0.019)$, $vlPFC_L(0.019)$, $PAC_R(0.016)$	$ExtGP_L(0.859)$, $IntGP_R(0.037)$, $ExtGP_R(0.015)$, $Occ_R(0.012)$, $SNpr_L(0.011)$, $Occ_L(0.01)$
$ExtGP_R$	$ExtGP_R(0.888)$, $mPFC_R(0.244)$, $OFC_R(0.11)$, $vlPFC_R(0.074)$, $mPFC_R(0.073)$, $Ling_L(0.067)$, $dlPFC_R(0.057)$, $ITC_L(0.04)$, $SPL_L(0.039)$, $mPFC_L(0.039)$, $IPL_L(0.032)$, $IPL_L(0.029)$, $SubTl_L(0.028)$, $MedTl_L(0.027)$, $Occ_L(0.027)$	$ExtGP_R(0.888)$, $SNpr_L(0.016)$, $ExtGP_L(0.015)$, $PAC_R(0.011)$, $Pu_L(0.011)$, $CN_L(0.009)$
$IntGP_L$	$IntGP_L(0.747)$, $Hipp_L(0.353)$, $Occ_L(0.29)$, $SPL_R(0.232)$, $PVC_L(0.213)$, $ITC_L(0.186)$, $IPL_R(0.181)$, $MedTl_L(0.18)$, $dlPFC_L(0.164)$, $SMA_R(0.158)$, $vlPFC_R(0.153)$, $Occ_L(0.14)$, $Precun_R(0.133)$, $PCL_L(0.126)$, $OFC_L(0.119)$	$IntGP_L(0.747)$, $IntGP_R(0.077)$, $SubTl_R(0.021)$, $SubTl_L(0.018)$, $SNpc_R(0.018)$, $SNpr_L(0.008)$
$IntGP_R$	$IntGP_R(0.745)$, $Occ_L(0.142)$, $dlPFC_R(0.128)$, $Occ_L(0.113)$, $IPL_R(0.087)$, $IntGP_L(0.077)$, $Occ_R(0.065)$, $Hipp_L(0.06)$, $mPFC_L(0.052)$, $Occ_R(0.051)$, $OFC_L(0.048)$, $PAC_L(0.048)$, $mPFC_L(0.047)$, $OFC_R(0.047)$, $PSC_R(0.045)$	$IntGP_R(0.745)$, $IntGP_L(0.059)$, $ExtGP_R(0.014)$, $SNpr_L(0.012)$, $ExtGP_L(0.01)$, $Occ_R(0.008)$

Table 7.1: **Transmission of iron to/from deep grey nuclei, control population 2.** Predicted connections to and from deep grey nuclei regions for control population 2. Only connections greater than .05 are included.

<div align="center">

Transmission of Iron To/From Deep Grey Nuclei, $p > .05$
AD Population

</div>

ROI	From x to ROI	To x From ROI
Pu_L	$Pu_L(0.728)$, $PAC_L(0.09)$, $vlPFC_L(0.089)$, $OFC_R(0.08)$, $ITC_L(0.073)$, $Occ_L(0.065)$, $OFC_L(0.053)$, $vlPFC_R(0.048)$, $IPL_R(0.042)$, $DN_L(0.037)$, $Temp_L(0.029)$, $vlPFC_R(0.026)$, $OFC_L(0.025)$, $dlPFC_L(0.023)$, $Pu_R(0.022)$	$Pu_L(0.728)$, $SNpr_R(0.027)$, $ExtAmygd_R(0.023)$, $OFC_R(0.022)$, $mPFC_L(0.019)$, $SNpr_L(0.018)$, $IntGP_R(0.017)$, $OFC_L(0.012)$, $PuTl_L(0.01)$, $vlPFC_L(0.009)$, $Temp_R(0.009)$, $Pu_R(0.008)$, $Occ_L(0.008)$
Pu_R	$Pu_R(0.722)$, $ITC_R(0.216)$, $ITC_L(0.07)$, $Occ_L(0.064)$, $IPL_L(0.05)$, $Occ_R(0.045)$, $mPFC_R(0.045)$, $PAC_R(0.033)$, $CN_R(0.031)$, $vlPFC_R(0.029)$, $RN_L(0.028)$, $vlPFC_R(0.024)$, $PAC_L(0.023)$, $SNpc_L(0.018)$, $dlPFC_R(0.017)$	$Pu_R(0.722)$, $ExtGP_R(0.08)$, $ExtGP_L(0.042)$, $SNpr_L(0.031)$, $Pu_L(0.022)$, $SNpc_R(0.015)$
CN_L	$CN_L(0.646)$, $SMA_R(0.057)$, $PAC_R(0.052)$, $CN_R(0.041)$, $SPL_L(0.039)$, $IPL_L(0.037)$, $PAC_R(0.034)$, $PAC_L(0.031)$, $mPFC_R(0.03)$, $PCL_L(0.029)$, $Temp_L(0.026)$, $OFC_R(0.019)$, $SMA_L(0.019)$, $ITC_R(0.018)$, $mPFC_R(0.017)$	$CN_L(0.646)$, $ExtGP_L(0.093)$, $SNpc_L(0.043)$, $IntGP_L(0.028)$, $SubTl_L(0.026)$, $ExtGP_R(0.022)$, $SNpc_R(0.018)$, $DN_L(0.015)$, $ExtAmygd_L(0.013)$, $DN_R(0.012)$, $ExtAmygd_R(0.01)$
CN_R	$CN_R(0.674)$, $PAC_R(0.107)$, $mPFC_R(0.078)$, $VTC_L(0.07)$, $ITC_R(0.068)$, $Hipp_L(0.06)$, $PMC_R(0.054)$, $IPL_L(0.038)$, $Occ_R(0.037)$, $PAC_R(0.032)$, $PAC_L(0.029)$, $IPL_L(0.024)$, $PAC_L(0.023)$, $PC_L(0.018)$, $SPL_R(0.018)$	$CN_R(0.674)$, $ExtGP_R(0.05)$, $CN_L(0.041)$, $Pu_R(0.031)$, $ExtGP_L(0.027)$, $SNpc_R(0.026)$, $DN_R(0.023)$, $SNpc_L(0.02)$, $SubTl_R(0.015)$, $SubTl_L(0.013)$, $DN_L(0.012)$, $IntGP_L(0.009)$, $Pu_L(0.009)$
$ExtGP_L$	$ExtGP_L(0.78)$, $PAC_R(0.163)$, $PC_R(0.14)$, $dlPFC_L(0.121)$, $OFC_R(0.098)$, $CN_L(0.093)$, $Temp_L(0.09)$, $vlPFC_L(0.088)$, $SMA_L(0.079)$, $Temp_R(0.07)$, $mPFC_L(0.063)$, $dlPFC_R(0.059)$, $Ling_L(0.056)$, $IPL_R(0.048)$, $IPL_L(0.044)$	$ExtGP_L(0.78)$, $IntGP_L(0.042)$, $ExtGP_R(0.04)$, $IntGP_R(0.026)$, $SNpr_L(0.023)$, $SNpr_R(0.019)$, $SNpc_R(0.013)$
$ExtGP_R$	$ExtGP_R(0.744)$, $dlPFC_L(0.147)$, $PC_R(0.092)$, $Pu_R(0.08)$, $IPL_R(0.07)$, $ITC_R(0.067)$, $IPL_L(0.066)$, $Temp_L(0.064)$, $IPL_L(0.063)$, $PAC_R(0.057)$, $mPFC_R(0.056)$, $Occ_R(0.055)$, $OFC_R(0.055)$, $PAC_L(0.054)$, $VTC_L(0.053)$	$ExtGP_R(0.744)$, $SNpr_L(0.047)$, $IntGP_R(0.016)$, $SNpc_R(0.016)$, $PuTl_L(0.015)$, $SNpr_R(0.015)$, $PAC_R(0.012)$, $PuTl_R(0.01)$, $RN_R(0.01)$, $ExtGP_L(0.01)$
$IntGP_L$	$IntGP_L(0.807)$, $SMA_L(0.173)$, $vlPFC_L(0.142)$, $mPFC_L(0.139)$, $vlPFC_R(0.108)$, $Temp_R(0.092)$, $IPL_R(0.055)$, $OFC_L(0.055)$, $Ling_L(0.054)$, $VTC_R(0.053)$, $SMA_R(0.051)$, $SPL_R(0.049)$, $dlPFC_L(0.048)$, $OFC_R(0.046)$, $dlPFC_R(0.045)$	$IntGP_L(0.807)$, $IntGP_R(0.054)$, $ExtGP_R(0.017)$, $Pu_L(0.016)$, $ExtGP_L(0.015)$, $ExtAmygd_R(0.009)$, $SNpr_R(0.009)$
$IntGP_R$	$IntGP_R(0.773)$, $mPFC_L(0.099)$, $IPL_R(0.084)$, $OFC_L(0.062)$, $PCL_R(0.055)$, $IPL_R(0.054)$, $IntGP_L(0.054)$, $OFC_L(0.053)$, $MedTl_L(0.034)$, $vlPFC_R(0.033)$, $PSC_L(0.029)$, $SPL_R(0.028)$, $PuTl_R(0.027)$, $ExtGP_L(0.026)$, $OFC_R(0.025)$	$IntGP_R(0.773)$, $SNpc_R(0.019)$, $RN_R(0.017)$, $RN_L(0.014)$, $SNpr_R(0.014)$, $mPFC_L(0.01)$, $ExtAmygd_L(0.009)$, $Temp_L(0.009)$, $vlPFC_R(0.009)$

Table 7.2: **Transmission of iron to/from deep grey nuclei, AD population.** Predicted connections to and from deep grey nuclei regions for AD population. Only connections greater than .05 are included.

Predicted Local Accumulation of Iron: AD Population

Predicted Local Accumulation of Iron: Control Population 2

Figure 7.3: **Predicted local accumulation of iron (QSM), AD vs. control**. Our model, when trained using QSM iron estimates with cortical and deep grey matter as nodes, predicts slightly higher local accumulation of iron in the deep grey nuclei for both the control and AD population.

Local Accumulation of Iron:
AD Population (QSM)

	Cortex	Deep Grey
Mean	.181	.540
Standard Dev	.180	.312

Control Population 2 (QSM)

	Cortex	Deep Grey
Mean	.198	.544
Standard Dev	.187	.334

Table 7.3: **Predicted local accumulation of iron (QSM), AD vs. control summary statistics**. Predicted probability of self-transmission for nodes in the cortex and deep grey nuclei for both the AD and control population.
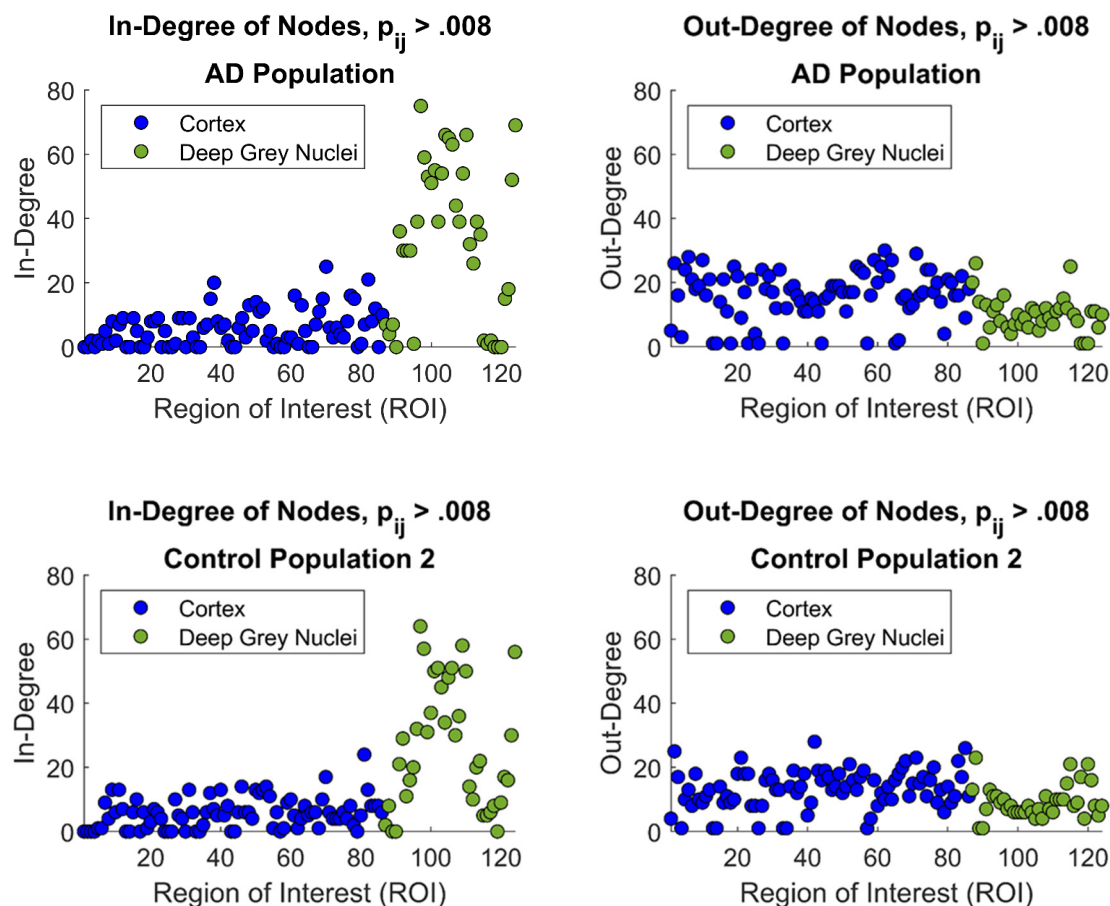
Figure 7.4: **Degree of nodes: AD vs. control population (QSM)**. Our model, when trained using QSM iron estimates with grey matter regions as nodes, predicts higher in-degree and lower out-degree of nodes in the deep grey nuclei for both the AD and control population.

Degree of Nodes (QSM):
AD Population

	In-Degree		Out-Degree	
	Cortex	**Deep Grey**	**Cortex**	**Deep Grey**
Mean	5.65	33.11	15.92	9.87
Std Dev	5.64	24.22	7.77	5.66
	Control Population 2			
Mean	5.72	26.29	13.23	9.29
Std Dev	4.83	19.31	6.07	5.13

Table 7.4: **Degree of nodes (QSM), AD vs. control summary statistics**. In-degree and out-degree calculated for nodes in grey matter regions for both the control and AD population.

7.3.2 PCS iron estimate

We repeat the preceding analyses using PCS iron estimates for the AD and control populations, using regions in the cerebellum, cortex, deep grey nuclei, and white matter as nodes. Our results again show that the model is able to successfully predict altered iron transport dynamics in the basal ganglia when trained with PCS iron estimates.
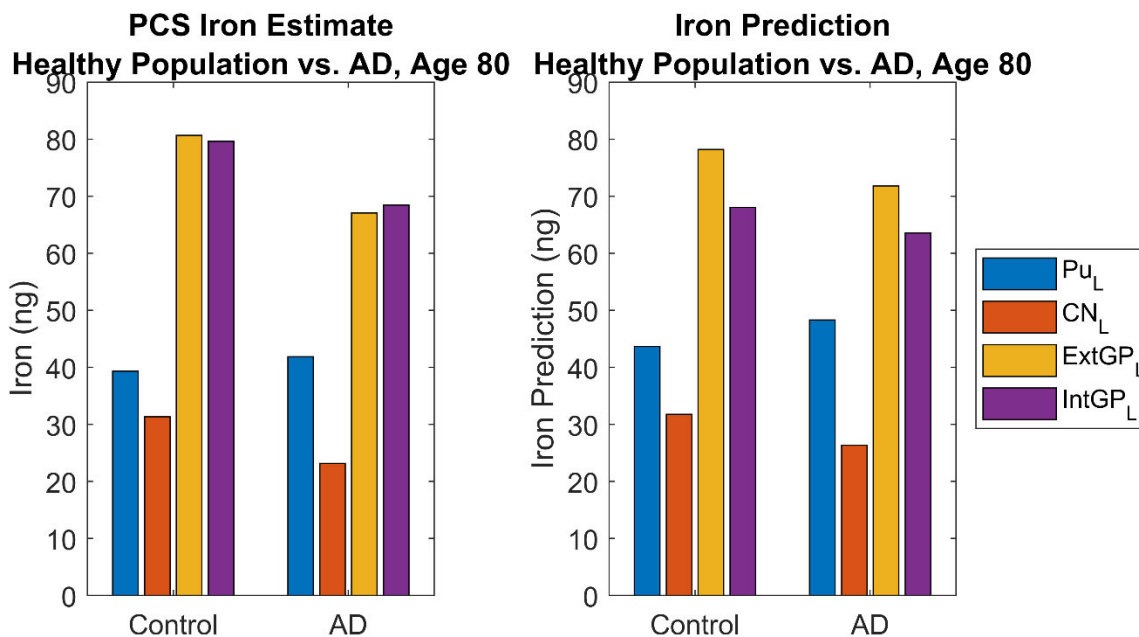
Figure 7.5: **Model prediction of altered iron deposition in the basal ganglia in AD (PCS)**. The observed iron concentrations, estimated with PCS, in basal ganglia regions in AD brains are different than in those of normal controls. The model prediction is determined by forward simulating 35 years from an initial distribution set by the training dataset at age 45. Our model successfully predicts altered iron transport dynamics in these regions.
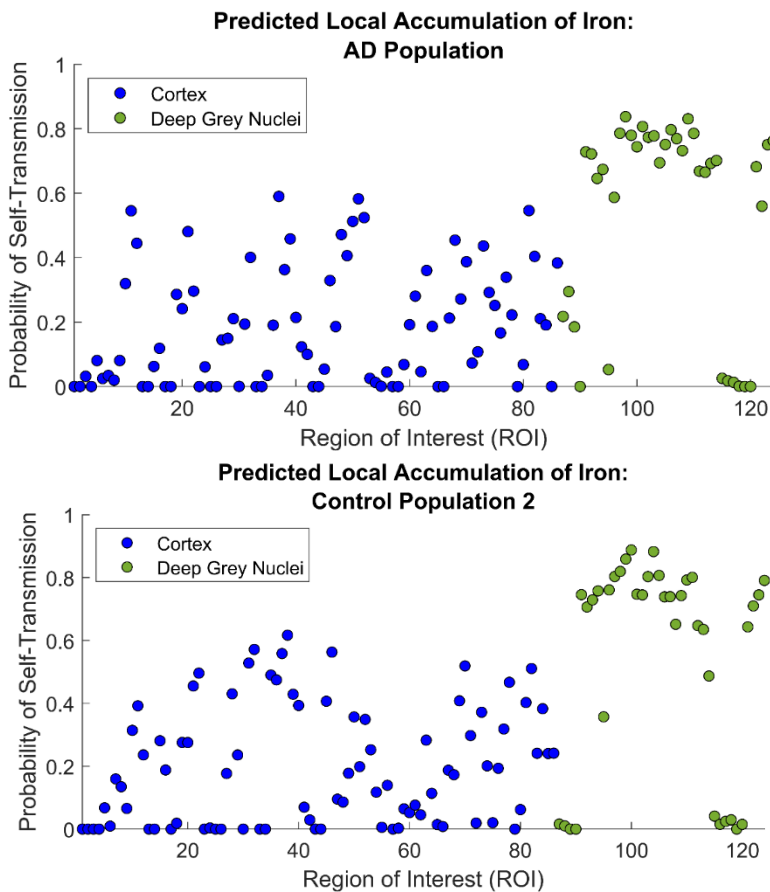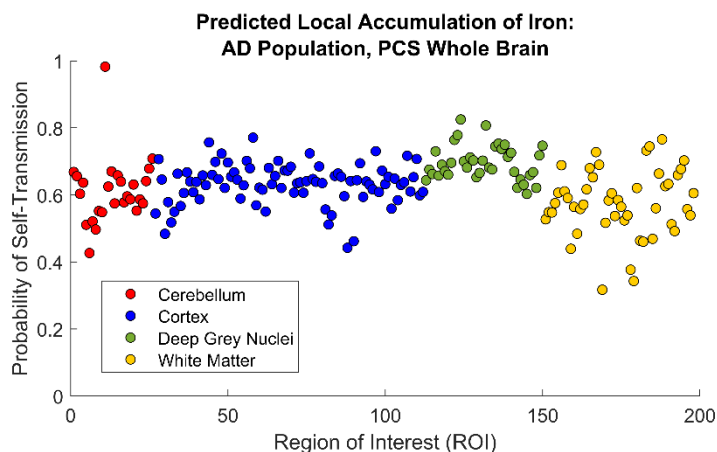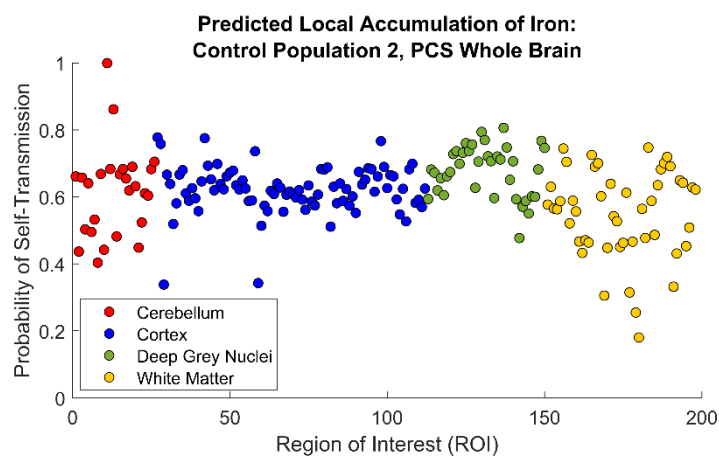
Figure 7.6: **Predicted local accumulation of iron (PCS), AD vs. control**. Our model, when trained using PCS iron estimates with cortical and deep grey matter as nodes, predicts slightly higher local accumulation of iron in the deep grey nuclei for both the control and AD population.

Local Accumulation of Iron:
AD Population (PCS)

	Cerebellum	Cortex	Deep Grey	White Matter
Mean	.612	.632	.696	.576
Standard Dev	.100	.060	.051	.099

Control Population 2 (PCS)

	Cerebellum	Cortex	Deep Grey	White Matter
Mean	.615	.622	.678	.549
Standard Dev	.133	.071	.075	.132

Table 7.5: **Predicted local accumulation of iron (PCS), AD vs. control summary statistics**. Predicted probability of self-transmission for nodes in the cortex and deep grey nuclei for both the AD and control population.

Although we again find some differences in the graph measures between the two populations, these differences are not statistically significant. The predicted in-degree of deep grey nuclei nodes is observed to be slightly higher for the AD population (23.76) than the control population (20.74), mirroring our finding for the model trained with QSM iron estimates. These values are calculated after thresholding the Markov probability matrix, averaged over 1000 bootstrap resamples, by .008 (as described in Ch. 5 and 6). The deep grey regions also display slightly higher predicted local accumulation of iron for the AD population (.696) than the control population (.678).
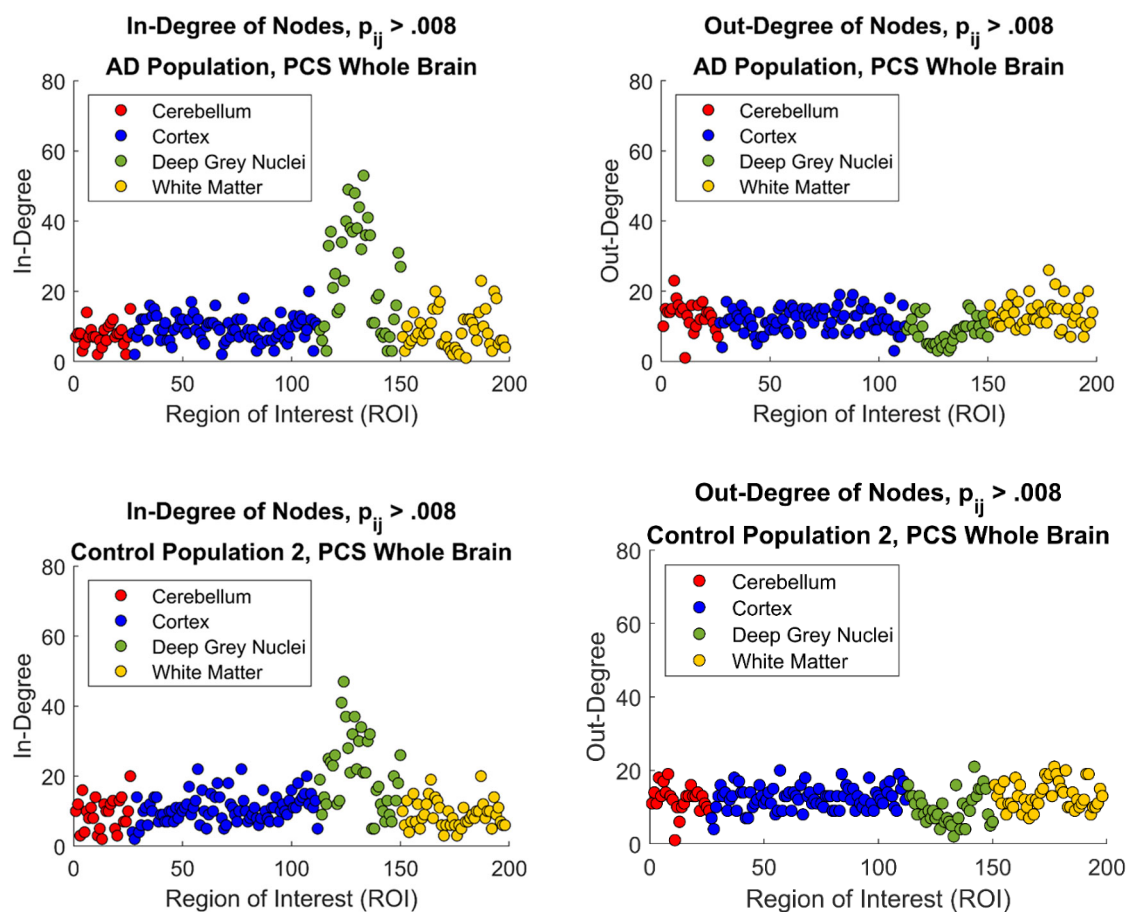
Figure 7.7: **Degree of nodes: AD vs. control population (PCS)**. Our model, when trained using PCS iron estimates with cerebellar, cortical, deep grey nuclei, and white matter regions as nodes, predicts higher in-degree and lower out-degree of nodes in the deep grey nuclei for both the AD and control population.

Degree of Nodes (PCS):
AD Population

	In-Degree				Out-Degree			
	Cerebellum	Cortex	Deep Grey	White Matter	Cerebellum	Cortex	Deep Grey	White Matter
Mean	7.54	9.37	23.76	8.81	13.0	11.80	8.61	13.50
Std Dev	3.20	3.58	14.94	5.27	4.17	3.33	3.64	3.98
Control Population 2								
Mean	9.31	10.76	20.74	9.06	12.08	12.47	9.68	13.25
Std Dev	4.52	3.98	10.58	3.76	3.67	3.10	4.34	3.73

Table 7.6: **Degree of nodes (PCS), AD vs. control summary statistics**. In-degree and out-degree calculated for nodes in grey matter regions for both the control and AD population.

7.4 Discussion

The motivation behind developing a mathematical model of iron transport in the brain was to unravel the mystery behind the spatio-temporal pattern of iron accumulation that is seen with age. This is relevant to the study of neurodegenerative disorders like AD, as iron concentrations in AD brains have been observed to be altered from those associated with normal aging [30], [42], [169], [170]. Studies have found increased iron in the deep nuclei regions in AD brains, however these studies tend to average across subjects of many ages, or look at patients in the earlier stages of the disease [30], [31], [171]. Our own analysis of basal ganglia regions (Fig. 7.5) shows that the normal pattern of exponential iron accumulation is disrupted in AD brains, and the iron estimate is actually observed to be lower in the GP and CN at advanced age in the AD brains when compared to healthy controls.

Additionally, we see that our model is able to accurately predict the alterations seen in the basal ganglia. However, the exact mechanism resulting in this difference is unclear. Although we see a higher number of predicted connections to deep grey nuclei nodes in the AD model compared to the control, this difference was not significant following an analysis of variance. When training with PCS data, the AD model predicts slightly higher probability of iron staying in all regions of the brain but the cerebellum. This suggests that AD brains may have less efficient transport of iron, although this difference was also not significant following an analysis of variance. Despite this, the model predicts differences in the pathways between deep grey nuclei regions, however, further analysis is needed to make sense of these comparisons.

It's not clear whether disrupted iron homeostasis is a cause or secondary effect of AD. The precursor protein to pathological amyloid beta plaques is involved in the transport of iron outside of cells, as is tau protein [30], [173]. Studies have also found an association between the apolipoprotein-E4 (APOE4) allele, which confers an increased risk of developing AD, and elevated brain iron [30], [172], [173]. Altered levels of the iron transporters transferrin (Tf) and ferritin (Ftn), as well as iron concentrations, in cortical regions measured from post-mortem brains provide further evidence for disrupted iron homeostasis in AD [170]. This suggests that not only is disordered iron transport a consequence of AD, but that altered iron homeostasis may be a primary mechanism of its progression.

Our inconclusive results may be the consequence of the AD population used to train the model. This population is composed of subjects diagnosed with either AD or mild cognitive impairment (MCI). Although there is overlap between the two diagnoses, studies have demonstrated variation in pathology seen in MCI, depending on whether other risk factors for AD are present [30], [174]. In particular, [30] found no difference in cortical iron levels for subjects diagnosed with MCI when compared to controls, however, a significantly higher level

of iron was seen in brain regions known be affected in AD for the MCI subjects who were carriers of the APOE4 allele. Additionally, there is evidence that the APOE4 allele is connected to both the cascade of brain iron accumulation as well as alterations in cortical networks [172], [173]. It would be interesting to redo our analysis using only a subset of the AD population, including only those with an AD diagnosis, or those displaying the APOE allele. Possibly by considering these smaller subsets with more advanced stages of the disease or greater genetic risk, we would see even larger differences between the predicted Markov probability matrix between the pathological and healthy populations.

7.5   Limitations

There are several limitations to our analyses. We are constrained by the availability of data, in particular, the ages of the subjects imaged for the AD population set. The age range skewed older, which likely affected our result. This is evidenced by the difference between the model predicted using iron estimates for control population 2 in this chapter and previous chapters, as we had to discard early time points from this set in order for the age distribution to align with the AD set (ages 45-90). At the older ages the iron accumulation has mostly plateaued, so it makes sense why the model prediction changed compared to the prediction found when training using earlier timepoints [19], [20].

Another limitation is that our model didn't account for the blood brain barrier dysfunction that is known to occur in AD [174]. Since we didn't account for this in the source term of our model, this could be affecting the predicted Markov transition probabilities. Our finding of minimal differences in the graph comparisons between the control and pathological population is surprising but may indicate that the AD population used is too variable. The AD population contained subjects diagnosed with both AD and MCI, and a subset of these carried the APOE4 allele, which is known to be associated with both a greater risk of developing AD and altered iron levels in AD [30], [172], [173]. Repeating our analysis using the subset of subjects carrying the APOE4 allele may yield a more interesting result.

Chapter 8

Conclusions and Future Directions

We've shown that QSM is a dynamic estimate of iron that reflects its concentration and activity, as measured by iron transporter expression, in the deep grey nuclei. We've also shown that our Markov model, when transition probabilities are estimated following the active transport hypothesis, accurately predicts the spatio-temporal pattern of iron in the brain. This work has significance for understanding the relationship between iron accumulation and neurodegeneration. This is further demonstrated by our work showing that our model predicts altered iron transport dynamics when trained on QSM and PCS data from subjects with Alzheimer's disease (AD).

It would be interesting to experimentally validate our model with an autoradiographic study, and possibly this approach could be used to identify more iron transport pathways. Autoradiographic experiments have been successfully used to identify iron transport pathways, as in [106], however, they are costly and it is infeasible to consider all brain regions. Our model identifies possible pathways between regions which can be experimentally tested using autoradiographic studies, therefore, serving as a useful tool in guiding these experiments.

In future, we hope to improve on our model by introducing more biologically motivated constraints, for instance, taking into account axonal connection. This could be done using connectivity atlases, which define an adjacency matrix of structural connections in the brain using diffusion tensor imaging (DTI) MRI [175]. However, connectivity atlases currently are limited in the scope of the brain regions they look at, and deep grey nuclei regions are frequently not included [175]. Alternatively, we could try a weighted combination of the passive diffusion model and active transport model. Also, a source term that takes into account time-dependent changes in blood brain barrier (BBB) integrity and is more detailed on a spatial level would help refine the model and separate out possible changes in iron transport due to aging-associated BBB leakage.

The Markov model could be further refined by shortening the time step, which would be possible with more data. We could also solve for a more time-dependent version of the Markov model by solving the optimization problem over smaller, successive time windows. We can use the UK Biobank dataset, which is an ongoing longitudinal imaging study of middle to older aged participants in the UK [176]. This dataset contains far more subjects than our current datasets, which would make these additional analyses possible.

Finally, we hope to continue our exploration of applying the Markov model to the study of altered iron transport dynamics in AD. Studies have indicated that the APOE4 allele confers a greater risk of developing AD and may also be involved in the dysregulation of iron homeostasis

in the disease [30], [172]. We plan to repeat our analysis of the Markov transition probability matrix found for an AD population in Chapter 7 using only subjects carrying the APOE4 allele.

Through a combination of Markov chain mathematics, blood brain barrier measurements taken from literature, and iron estimates from QSM, our model provides a systematic approach to describing the dynamics of iron transport in the brain on the system level. We have achieved the goals of this project, and we hope our work is helpful to advancing the understanding of brain iron homeostasis that is required for developing new techniques for early diagnosis and treatment of neurodegenerative disorders like AD.

Bibliography

[1]   A. D. Sheftel, A. B. Mason, and P. Ponka, "The long history of iron in the Universe and in health and disease," *Biochim. Biophys. Acta - Gen. Subj.*, vol. 1820, no. 3, pp. 161–187, Mar. 2012, doi: 10.1016/j.bbagen.2011.08.002.

[2]   A. Katsarou and K. Pantopoulos, "Basics and principles of cellular and systemic iron homeostasis," *Mol. Aspects Med.*, vol. 75, p. 100866, Oct. 2020, doi: 10.1016/j.mam.2020.100866.

[3]   J. R. Connor and S. L. Menzies, "Relationship of iron to oligodendrocytes and myelination," *GLIA*, vol. 17, no. 2, pp. 83–93, Jun. 1996, doi: 10.1002/(SICI)1098-1136(199606)17:2<83::AID-GLIA1>3.0.CO;2-7.

[4]   E. Ortiz *et al.*, "Effect of manipulation of iron storage, transport, or availability on myelin composition and brain iron content in three different animal models," *J. Neurosci. Res.*, vol. 77, no. 5, pp. 681–689, Sep. 2004, doi: 10.1002/jnr.20207.

[5]   *Neuroscience Online*. Department of Neurobiology and Anatomy, McGovern Medical School at UTHealth, 2020. [Online]. Available: https://nba.uth.tmc.edu/neuroscience/

[6]   H. E. Möller *et al.*, "Iron, Myelin, and the Brain: Neuroimaging Meets Neurobiology," *Trends Neurosci.*, vol. 42, no. 6, pp. 384–401, Jun. 2019, doi: 10.1016/j.tins.2019.03.009.

[7]   N. Baumann and D. Pham-Dinh, "Biology of oligodendrocyte and myelin in the mammalian central nervous system," *Physiol. Rev.*, vol. 81, no. 2, pp. 871–927, 2001, doi: 10.1152/PHYSREV.2001.81.2.871/ASSET/IMAGES/LARGE/9J0210133008.JPEG.

[8]   J. R. Connor and S. L. Menzies, "Cellular management of iron in the brain," *J. Neurol. Sci.*, vol. 134, no. SUPPL., pp. 33–44, Dec. 1995, doi: 10.1016/0022-510X(95)00206-H.

[9]   V. T. Cheli, J. Correale, P. M. Paez, and J. M. Pasquini, "Iron Metabolism in Oligodendrocytes and Astrocytes, Implications for Myelination and Remyelination," *ASN Neuro*, vol. 12, Sep. 2020, doi: 10.1177/1759091420962681/ASSET/IMAGES/LARGE/10.1177_1759091420962681-FIG1.JPEG.

[10]   M. Chen, E. Xu, C. Zeng, W. Zhu, J. Zheng, and H. Chen, "High Dietary Iron Has a Greater Impact on Brain Iron Homeostasis and Cognitive Function in Old Compared with Young C57BL/6J Male Mice," *J. Nutr.*, vol. 151, no. 9, pp. 2835–2842, Sep. 2021, doi: 10.1093/jn/nxab189.

[11]   T. J. Sobotka *et al.*, "Neurobehavioral dysfunctions associated with dietary iron overload," *Physiol. Behav.*, vol. 59, no. 2, pp. 213–219, Feb. 1996, doi: 10.1016/0031-9384(95)02030-6.

[12]   M. Chen *et al.*, "High Dietary Iron Disrupts Iron Homeostasis and Induces Amyloid-β and Phospho-τ Expression in the Hippocampus of Adult Wild-Type and APP/PS1 Transgenic Mice," *J. Nutr.*, vol. 149, no. 12, pp. 2247–2254, Dec. 2019, doi: 10.1093/jn/nxz168.

[13]   J. Kim and M. Wessling-Resnick, "Iron and mechanisms of emotional behavior," *J. Nutr. Biochem.*, vol. 25, no. 11, pp. 1101–1107, Nov. 2014, doi: 10.1016/j.jnutbio.2014.07.003.

[14]   B. Lozoff, J. Beard, J. Connor, B. Felt, M. Georgieff, and T. Schallert, "Long-Lasting Neural and Behavioral Effects of Iron Deficiency in Infancy," *Nutr. Rev.*, vol. 64, no. suppl_2, pp. S34–S43, May 2006, doi: 10.1111/j.1753-4887.2006.tb00243.x.

[15] K. L. H. Carpenter *et al.*, "Magnetic susceptibility of brain iron is associated with childhood spatial IQ," *NeuroImage*, vol. 132, pp. 167–174, May 2016, doi: 10.1016/j.neuroimage.2016.02.028.

[16] A. Ferreira, P. Neves, and R. Gozzelino, "Multilevel Impacts of Iron in the Brain: The Cross Talk between Neurophysiological Mechanisms, Cognition, and Social Behavior," *Pharmaceuticals*, vol. 12, no. 3, p. 126, Aug. 2019, doi: 10.3390/ph12030126.

[17] M. Han and J. Kim, "Effect of Dietary Iron Loading on Recognition Memory in Growing Rats," *PLoS ONE*, vol. 10, no. 3, p. e0120609, Mar. 2015, doi: 10.1371/journal.pone.0120609.

[18] W. Zhang *et al.*, "Brain Iron Deposits in Thalamus Is an Independent Factor for Depressive Symptoms Based on Quantitative Susceptibility Mapping in an Older Adults Community Population," *Front. Psychiatry*, vol. 10, 2019, Accessed: Jul. 11, 2023. [Online]. Available: https://www.frontiersin.org/articles/10.3389/fpsyt.2019.00734

[19] W. Li *et al.*, "Differential developmental trajectories of magnetic susceptibility in human brain gray and white matter over the lifespan," *Hum. Brain Mapp.*, vol. 35, no. 6, pp. 2698–2713, Jun. 2014, doi: 10.1002/HBM.22360.

[20] Y. Zhang, H. Wei, M. J. Cronin, N. He, F. Yan, and C. Liu, "Longitudinal atlas for normative human brain development and aging over the lifespan using quantitative susceptibility mapping," *NeuroImage*, vol. 171, pp. 176–189, May 2018, doi: 10.1016/j.neuroimage.2018.01.008.

[21] Y. Zhang, J. Shi, H. Wei, V. Han, W. Z. Zhu, and C. Liu, "Neonate and infant brain development from birth to 2 years assessed using MRI-based quantitative susceptibility mapping," *NeuroImage*, vol. 185, pp. 349–360, Jan. 2019, doi: 10.1016/J.NEUROIMAGE.2018.10.031.

[22] M. W. B. Bradbury, "Transport of iron in the blood-brain-cerebrospinal fluid system," *J. Neurochem.*, vol. 69, no. 2, pp. 443–454, 1997, doi: 10.1046/j.1471-4159.1997.69020443.x.

[23] Y. Ke and Z. M. Qian, "Brain iron metabolism: neurobiology and neurochemistry," *Prog. Neurobiol.*, vol. 83, no. 3, pp. 149–173, Oct. 2007, doi: 10.1016/j.pneurobio.2007.07.009.

[24] T. Moos, T. R. Nielsen, T. Skjørringe, and E. H. Morgan, "Iron trafficking inside the brain," *J. Neurochem.*, vol. 103, no. 5, pp. 1730–1740, Dec. 2007, doi: 10.1111/j.1471-4159.2007.04976.x.

[25] C. Langkammer *et al.*, "Quantitative susceptibility mapping (QSM) as a means to measure brain iron? A post mortem validation study," *NeuroImage*, vol. 62, no. 3, pp. 1593–1599, Sep. 2012, doi: 10.1016/j.neuroimage.2012.05.049.

[26] W. Li, B. Wu, and C. Liu, "Quantitative susceptibility mapping of human brain reflects spatial variation in tissue composition," *NeuroImage*, vol. 55, no. 4, pp. 1645–1656, Apr. 2011, doi: 10.1016/j.neuroimage.2010.11.088.

[27] P. Matak *et al.*, "Disrupted iron homeostasis causes dopaminergic neurodegeneration in mice," *Proc. Natl. Acad. Sci.*, vol. 113, no. 13, pp. 3428–3435, Mar. 2016, doi: 10.1073/pnas.1519473113.

[28] Y. Peng, X. Chang, and M. Lang, "Iron Homeostasis Disorder and Alzheimer's Disease," *Int. J. Mol. Sci.*, vol. 22, no. 22, Art. no. 22, Jan. 2021, doi: 10.3390/ijms222212442.

[29] N. Ball, W.-P. Teo, S. Chandra, and J. Chapman, "Parkinson's Disease and the Environment," *Front. Neurol.*, vol. 10, p. 218, 2019, doi: 10.3389/fneur.2019.00218.

[30] J. M. G. van Bergen *et al.*, "Colocalization of cerebral iron with Amyloid beta in Mild Cognitive Impairment," *Sci. Rep.*, vol. 6, p. 35514, Oct. 2016, doi: 10.1038/srep35514.

[31] P. M. Cogswell *et al.*, "Associations of quantitative susceptibility mapping with Alzheimer's disease clinical and imaging markers," *NeuroImage*, vol. 224, p. 117433, Jan. 2021, doi: 10.1016/j.neuroimage.2020.117433.

[32] S. Agrawal, K. L. Berggren, E. Marks, and J. H. Fox, "Impact of high iron intake on cognition and neurodegeneration in humans and in animal models: a systematic review," *Nutr. Rev.*, vol. 75, no. 6, pp. 456–470, Jun. 2017, doi: 10.1093/nutrit/nux015.

[33] A. Ndayisaba, C. Kaindlstorfer, and G. K. Wenning, "Iron in neurodegeneration - Cause or consequence?," *Front. Neurosci.*, vol. 13, 2019, doi: 10.3389/fnins.2019.00180.

[34] Z. M. Qian and Y. Ke, "Brain iron transport," *Biol. Rev.*, vol. 94, no. 5, pp. 1672–1684, Oct. 2019, doi: 10.1111/BRV.12521.

[35] E. Mills, X. P. Dong, F. Wang, and H. Xu, "Mechanisms of Brain Iron Transport: Insight into Neurodegeneration and CNS Disorders," *Future Med. Chem.*, vol. 2, no. 1, pp. 51–51, Jan. 2010, doi: 10.4155/FMC.09.140.

[36] T. Skjørringe, A. Burkhart, K. B. Johnsen, and T. Moos, "Divalent metal transporter 1 (DMT1) in the brain: Implications for a role in iron transport at the blood-brain barrier, and neuronal and glial pathology," *Front. Mol. Neurosci.*, vol. 8, no. June, pp. 19–19, Jun. 2015, doi: 10.3389/FNMOL.2015.00019/BIBTEX.

[37] L. J. C. Wu *et al.*, "Expression of the iron transporter ferroportin in synaptic vesicles and the blood–brain barrier," *Brain Res.*, vol. 1001, no. 1–2, pp. 108–117, Mar. 2004, doi: 10.1016/J.BRAINRES.2003.10.066.

[38] E. C. Theil, "FERRITIN: STRUCTURE, GENE REGULATION, AND CELLULAR FUNCTION IN ANIMALS, PLANTS, AND MICROORGANISMS," *Annu. Rev. Biochem.*, vol. 56, no. 1, pp. 289–315, Jun. 1987, doi: 10.1146/annurev.bi.56.070187.001445.

[39] D. G. Nishimura, *Principles of Magnetic Resonance Imaging*. Department of Electrical Engineering, Stanford University, 2010.

[40] C. Liu, W. Li, K. A. Tong, K. W. Yeom, and S. Kuzminski, "Susceptibility-weighted imaging and quantitative susceptibility mapping in the brain," *J. Magn. Reson. Imaging*, vol. 42, no. 1, pp. 23–41, Jul. 2015, doi: 10.1002/jmri.24768.

[41] A. Elster and J. Burdette, *Questions and Answers in MRI*, 2nd ed. St. Louis, Mo, 2001.

[42] R. J. Ward, F. A. Zucca, J. H. Duyn, R. R. Crichton, and L. Zecca, "The role of iron in brain ageing and neurodegenerative disorders," *Lancet Neurol.*, vol. 13, no. 10, pp. 1045–1060, Oct. 2014, doi: 10.1016/S1474-4422(14)70117-6.

[43] B. Bilgic, A. Pfefferbaum, T. Rohlfing, E. V. Sullivan, and E. Adalsteinsson, "MRI Estimates of Brain Iron Concentration in Normal Aging Using Quantitative Susceptibility Mapping," *Neuroimage*, vol. 59, no. 3, pp. 2625–2635, 2012, doi: 10.1016/j.neuroimage.2011.08.077.

[44] L. de Rochefort *et al.*, "Quantitative susceptibility map reconstruction from MR phase data using bayesian regularization: Validation and application to brain imaging," *Magn. Reson. Med.*, vol. 63, no. 1, pp. 194–206, 2010, doi: 10.1002/mrm.22187.

[45] J. Liu *et al.*, "Morphology enabled dipole inversion for quantitative susceptibility mapping using structural consistency between the magnitude image and the susceptibility map," *NeuroImage*, vol. 59, no. 3, pp. 2560–2568, Feb. 2012, doi: 10.1016/j.neuroimage.2011.08.082.

[46] Y. Wang and T. Liu, "Quantitative susceptibility mapping (QSM): Decoding MRI data for a tissue magnetic biomarker," *Magn. Reson. Med.*, vol. 73, no. 1, pp. 82–82, Jan. 2015, doi: 10.1002/MRM.25358.

[47] H. Wei *et al.*, "Imaging whole-brain cytoarchitecture of mouse with MRI-based quantitative susceptibility mapping," *NeuroImage*, vol. 137, pp. 107–115, Aug. 2016, doi: 10.1016/j.neuroimage.2016.05.033.

[48] F. Schweser, A. Deistung, and J. R. Reichenbach, "Foundations of MRI phase imaging and processing for Quantitative Susceptibility Mapping (QSM)," *Z. Med. Phys.*, vol. 26, no. 1, pp. 6–34, Mar. 2016, doi: 10.1016/j.zemedi.2015.10.002.

[49] A. Deistung, A. Rauscher, J. Sedlacik, J. Stadler, S. Witoszynskyj, and J. R. Reichenbach, "Susceptibility weighted imaging at ultra high magnetic field strengths: Theoretical considerations and experimental results," *Magn. Reson. Med.*, vol. 60, no. 5, pp. 1155–1168, 2008, doi: 10.1002/mrm.21754.

[50] C. Liu, "Susceptibility tensor imaging," *Magn. Reson. Med.*, vol. 63, no. 6, pp. 1471–1477, 2010, doi: 10.1002/mrm.22482.

[51] C. Liu, H. Wei, N.-J. Gong, M. Cronin, R. Dibb, and K. Decker, "Quantitative Susceptibility Mapping: Contrast Mechanisms and Clinical Applications," *Tomography*, vol. 1, no. 1, pp. 3–17, Sep. 2015, doi: 10.18383/j.tom.2015.00136.

[52] S. Wharton, A. Schäfer, and R. Bowtell, "Susceptibility mapping in the human brain using threshold-based k-space division," *Magn. Reson. Med.*, vol. 63, no. 5, pp. 1292–1304, 2010, doi: 10.1002/mrm.22334.

[53] B. Wu, W. Li, A. Guidon, and C. Liu, "Whole brain susceptibility mapping using compressed sensing," *Magn. Reson. Med.*, vol. 67, no. 1, pp. 137–147, 2012, doi: 10.1002/MRM.23000.

[54] W. Zheng, H. Nichol, S. Liu, Y. C. N. Cheng, and E. M. Haacke, "Measuring iron in the brain using quantitative susceptibility mapping and X-ray fluorescence imaging," *NeuroImage*, vol. 78, pp. 68–74, Sep. 2013, doi: 10.1016/J.NEUROIMAGE.2013.04.022.

[55] B. Chiou, E. Lucassen, M. Sather, A. Kallianpur, and J. Connor, "Semaphorin4A and H-ferritin utilize Tim-1 on human oligodendrocytes: A novel neuro-immune axis," *GLIA*, vol. 66, no. 7, pp. 1317–1330, Jul. 2018, doi: 10.1002/glia.23313.

[56] B. Todorich, X. Zhang, and J. R. Connor, "H-ferritin is the major source of iron for oligodendrocytes," *GLIA*, vol. 59, no. 6, pp. 927–935, Jun. 2011, doi: 10.1002/glia.21164.

[57] C. Liu, W. Li, G. A. Johnson, and B. Wu, "High-Field (9.4 T) MRI of Brain Dysmyelination by Quantitative Mapping of Magnetic Susceptibility," 2010, doi: 10.1016/j.neuroimage.2011.02.024.

[58] I. Chavarria-Siles *et al.*, "Myelination-related genes are associated with decreased white matter integrity in schizophrenia," *Eur. J. Hum. Genet. 2016 243*, vol. 24, no. 3, pp. 381–386, May 2015, doi: 10.1038/ejhg.2015.120.

[59] S. Kuhn, L. Gritti, D. Crooks, and Y. Dombrowski, "Oligodendrocytes in Development, Myelin Generation and Beyond," *Cells 2019 Vol 8 Page 1424*, vol. 8, no. 11, pp. 1424–1424, Nov. 2019, doi: 10.3390/CELLS8111424.

[60] M. C. Ortega, A. Bribián, S. Peregrín, M. T. Gil, O. Marín, and F. de Castro, "Neuregulin-1/ErbB4 signaling controls the migration of oligodendrocyte precursor cells during development," *Exp. Neurol.*, vol. 235, no. 2, pp. 610–620, Jun. 2012, doi: 10.1016/j.expneurol.2012.03.015.

[61] J. H. Duyn, P. van Gelderen, T.-Q. Li, J. A. de Zwart, A. P. Koretsky, and M. Fukunaga, "High-field MRI of brain cortical substructure based on signal phase," *Proc. Natl. Acad. Sci.*, vol. 104, no. 28, pp. 11796–11801, Jul. 2007, doi: 10.1073/pnas.0610821104.

[62] M. J. Hawrylycz *et al.*, "An anatomically comprehensive atlas of the adult human brain transcriptome," *Nature*, vol. 489, no. 7416, pp. 391–399, Sep. 2012, doi: 10.1038/nature11405.

[63] C. Wang *et al.*, "Phenotypic and genetic associations of quantitative magnetic susceptibility in UK Biobank brain imaging," *Nat. Neurosci.*, vol. 25, no. 6, Art. no. 6, Jun. 2022, doi: 10.1038/s41593-022-01074-w.

[64] B. Benyamin *et al.*, "Novel loci affecting iron homeostasis and their effects in individuals at risk for hemochromatosis," *Nat. Commun. 2014 51*, vol. 5, no. 1, pp. 1–11, Oct. 2014, doi: 10.1038/ncomms5926.

[65] L. T. Elliott *et al.*, "Genome-wide association studies of brain imaging phenotypes in UK Biobank," *Nat. 2018 5627726*, vol. 562, no. 7726, pp. 210–216, Oct. 2018, doi: 10.1038/s41586-018-0571-7.

[66] "Allen Institute for Brain Science." Allen Human Brain Atlas: Microarray [dataset], Available from human.brain-map.org, 2010. doi: RRID:SCR_007416.

[67] E. H. Shen, C. C. Overly, and A. R. Jones, "The Allen Human Brain Atlas. Comprehensive gene expression mapping of the human brain.," *Trends Neurosci.*, vol. 35, no. 12, pp. 711–714, Dec. 2012, doi: 10.1016/j.tins.2012.09.005.

[68] S. M. Smith *et al.*, "Advances in functional and structural MR image analysis and implementation as FSL," *NeuroImage*, vol. 23, no. SUPPL. 1, pp. S208–S219, Jan. 2004, doi: 10.1016/J.NEUROIMAGE.2004.07.051.

[69] F. Schweser, A. Deistung, W. Lehr, and J. R. Reichenbach, "Quantitative imaging of intrinsic magnetic tissue properties using MRI signal phase: An approach to in vivo brain iron metabolism? ☆," 2010, doi: 10.1016/j.neuroimage.2010.10.070.

[70] Y. Zhu and M. A. Schofield, "Fast phase unwrapping algorithm for interferometric applications," *Opt. Lett. Vol 28 Issue 14 Pp 1194-1196*, vol. 28, no. 14, pp. 1194–1196, Jul. 2003, doi: 10.1364/OL.28.001194.

[71] H. Wei *et al.*, "Streaking artifact reduction for quantitative susceptibility mapping of sources with large dynamic range," *NMR Biomed.*, vol. 28, no. 10, pp. 1294–1303, 2015, doi: 10.1002/nbm.3383.

[72] B. B. Avants, N. Tustison, and G. Song, "Advanced Normalization Tools: V1.0," 2009.

[73] "Allen Human Brain Atlas Technical White Paper: Case qualification and donor profiles," 2013, [Online]. Available: https://help.brain-map.org/display/humanbrain/Documentation

[74] "Allen Human Brain Atlas Technical White Paper: Microarray survey," 2013, [Online]. Available: https://help.brain-map.org/display/humanbrain/Documentation

[75] A. Arnatkevičiūtė, B. D. Fulcher, and A. Fornito, "A practical guide to linking brain-wide gene expression and neuroimaging data," *NeuroImage*, vol. 189, pp. 353–367, Apr. 2019, doi: 10.1016/J.NEUROIMAGE.2019.01.011.

[76] "Genome Reference Consortium Human Build 38", [Online]. Available: https://www.ncbi.nlm.nih.gov/assembly/GCF_000001405.26/

[77] M. Hawrylycz *et al.*, "Canonical genetic signatures of the adult human brain," *Nat. Neurosci. 2015 1812*, vol. 18, no. 12, pp. 1832–1844, Nov. 2015, doi: 10.1038/nn.4171.

[78] X. Li *et al.*, "Multi-atlas tool for automated segmentation of brain gray matter nuclei and quantification of their magnetic susceptibility," *NeuroImage*, vol. 191, pp. 337–349, May 2019, doi: 10.1016/j.neuroimage.2019.02.016.

[79] "Allen Reference Atlas - Adult Human [brain atlas]." Available from atlas.brain-map.org.

[80] S.-L. Ding *et al.*, "Comprehensive cellular-resolution atlas of the adult human brain," *J. Comp. Neurol.*, vol. 524, no. 16, pp. 3127–3481, Nov. 2016, doi: 10.1002/cne.24080.

[81] Y. Benjamini and D. Yekutieli, "The Control of the False Discovery Rate in Multiple Testing under Dependency," *Ann. Stat.*, vol. 29, no. 4, pp. 1165–1188, 2001.

[82] Y. Benjamini and Y. Hochberg, "Controlling the False Discovery Rate: A Practical and Powerful Approach to Multiple Testing," *J. R. Stat. Soc. Ser. B Methodol.*, vol. 57, no. 1, pp. 289–300, Jan. 1995, doi: 10.1111/J.2517-6161.1995.TB02031.X.

[83] A. Reiner, D. Yekutieli, and Y. Benjamini, "Identifying differentially expressed genes using false discovery rate controlling procedures," *Bioinformatics*, vol. 19, no. 3, pp. 368–375, Feb. 2003, doi: 10.1093/BIOINFORMATICS/BTF877.

[84] P. Geladi and B. R. Kowalski, "PARTIAL LEAST-SQUARES REGRESSION: A TUTORIAL," *Anal. Chim. Acta*, vol. 186, 1986.

[85] H. Abdi, "Partial least squares regression and projection on latent structure regression (PLS Regression)," *WIREs Comput. Stat.*, vol. 2, no. 1, pp. 97–106, 2010, doi: 10.1002/wics.51.

[86] S. Wold, M. Sjöström, and L. Eriksson, "PLS-regression: a basic tool of chemometrics," *Chemom. Intell. Lab. Syst.*, vol. 58, no. 2, pp. 109–130, Oct. 2001, doi: 10.1016/S0169-7439(01)00155-1.

[87] I. N. Wakeling and J. J. Morris, "A test of significance for partial least squares regression," *J. Chemom.*, vol. 7, no. 4, pp. 291–304, 1993, doi: 10.1002/cem.1180070407.

[88] J. M. Hill and R. C. Switzer, "The regional distribution and cellular localization of iron in the rat brain," *Neuroscience*, vol. 11, no. 3, pp. 595–603, Mar. 1984, doi: 10.1016/0306-4522(84)90046-0.

[89] B. Valério-Gomes, D. M. Guimarães, D. Szczupak, and R. Lent, "The absolute number of oligodendrocytes in the adult mouse brain," *Front. Neuroanat.*, vol. 12, Oct. 2018, doi: 10.3389/fnana.2018.00090.

[90] B. Todorich, J. M. Pasquini, C. I. Garcia, P. M. Paez, and J. R. Connor, "Oligodendrocytes and myelination: The role of iron," *Glia*, vol. 57, no. 5, pp. 467–478, Apr. 2009, doi: 10.1002/GLIA.20784.

[91] P. Arosio and S. Levi, "Ferritin, iron homeostasis, and oxidative damage," *Free Radic. Biol. Med.*, vol. 33, no. 4, pp. 457–463, Aug. 2002, doi: 10.1016/S0891-5849(02)00842-0.

[92] S. Levi *et al.*, "Evidence of H- and L-chains have co-operative roles in the iron-uptake mechanism of human ferritin," *Biochem. J.*, vol. 288, no. 2, pp. 591–596, Dec. 1992, doi: 10.1042/BJ2880591.

[93] J. R. Connor, K. L. Boeshore, S. A. Benkovic, and S. L. Menzies, "Isoforms of ferritin have a specific cellular distribution in the brain," *J. Neurosci. Res.*, vol. 37, no. 4, pp. 461–465, Mar. 1994, doi: 10.1002/JNR.490370405.

[94] A. Reinert, M. Morawski, J. Seeger, T. Arendt, and T. Reinert, "Iron concentrations in neurons and glial cells with estimates on ferritin concentrations," *BMC Neurosci.*, vol. 20, no. 1, pp. 1–14, May 2019, doi: 10.1186/S12868-019-0507-7/FIGURES/7.

[95] X. Zhang, N. Surguladze, B. Slagle-Webb, A. Cozzi, and J. R. Connor, "Cellular iron status influences the functional relationship between microglia and oligodendrocytes," *Glia*, vol. 54, no. 8, pp. 795–804, Dec. 2006, doi: 10.1002/GLIA.20416.

[96] K. Schulz, A. Kroner, and S. David, "Iron Efflux from Astrocytes Plays a Role in Remyelination," *J. Neurosci.*, vol. 32, no. 14, pp. 4841–4847, Apr. 2012, doi: 10.1523/JNEUROSCI.5328-11.2012.

[97] Y. J. Suh and S. David, "Age-Related Changes in Iron Homeostasis and Cell Death in the Cerebellum of Ceruloplasmin-Deficient Mice," *J. Neurosci.*, vol. 26, no. 38, pp. 9810–9819, Sep. 2006, doi: 10.1523/JNEUROSCI.2922-06.2006.

[98] L. J. Lawson, V. H. Perry, P. Dri, and S. Gordon, "Heterogeneity in the distribution and morphology of microglia in the normal adult mouse brain," *Neuroscience*, vol. 39, no. 1, pp. 151–170, Jan. 1990, doi: 10.1016/0306-4522(90)90229-W.

[99] L. M. De Biase *et al.*, "Local Cues Establish and Maintain Region-Specific Phenotypes of Basal Ganglia Microglia," *Neuron*, vol. 95, no. 2, pp. 341-356.e6, Jul. 2017, doi: 10.1016/j.neuron.2017.06.020.

[100] K. Grabert *et al.*, "Microglial brain region−dependent diversity and selective regional sensitivities to aging," *Nat. Neurosci. 2016 193*, vol. 19, no. 3, pp. 504–516, Jan. 2016, doi: 10.1038/nn.4222.

[101] B. Bloch, T. Popovici, M. J. Levin, D. Tuil, and A. Kahn, "Transferrin gene expression visualized in oligodendrocytes of the rat brain by using in situ hybridization and immunohistochemistry.," *Proc. Natl. Acad. Sci.*, vol. 82, no. 19, pp. 6706–6710, Oct. 1985, doi: 10.1073/PNAS.82.19.6706.

[102] A. J. Dwork, E. A. Schon, and J. Herbert, "Nonidentical distribution of transferrin and ferric iron in human brain," *Neuroscience*, vol. 27, no. 1, pp. 333–345, Oct. 1988, doi: 10.1016/0306-4522(88)90242-4.

[103] C. M. Morris, J. M. Candy, C. A. Bloxharn, and J. A. Edwardson, "Immunocytochemical Localisation of Transferrin in the Human Brain," *Cells Tissues Organs*, vol. 143, no. 1, pp. 14–18, 1992, doi: 10.1159/000147223.

[104] J. M. Hill, M. R. Ruff, R. J. Weber, and C. B. Pert, "Transferrin receptors in rat brain: neuropeptide-like pattern and relationship to iron distribution.," *Proc. Natl. Acad. Sci.*, vol. 82, no. 13, pp. 4553–4557, Jul. 1985, doi: 10.1073/PNAS.82.13.4553.

[105] T. Moos and E. H. Morgan, "Kinetics and distribution of [59Fe–125I]transferrin injected into the ventricular system of the rat," *Brain Res.*, vol. 790, no. 1, pp. 115–128, Apr. 1998, doi: 10.1016/S0006-8993(98)00055-9.

[106] Z. Wang *et al.*, "Axonal iron transport in the brain modulates anxiety-related behaviors," *Nat. Chem. Biol.*, vol. 15, no. 12, Art. no. 12, Dec. 2019, doi: 10.1038/s41589-019-0371-x.

[107] J. r. Burdo *et al.*, "Distribution of divalent metal transporter 1 and metal transport protein 1 in the normal and Belgrade rat," *J. Neurosci. Res.*, vol. 66, no. 6, pp. 1198–1207, 2001, doi: 10.1002/jnr.1256.

[108] V. T. Cheli *et al.*, "The Divalent Metal Transporter 1 (DMT1) Is Required for Iron Uptake and Normal Development of Oligodendrocyte Progenitor Cells," *J. Neurosci.*, vol. 38, no. 43, pp. 9142–9159, Oct. 2018, doi: 10.1523/JNEUROSCI.1447-18.2018.

[109] V. T. Cheli *et al.*, "Transferrin Receptor Is Necessary for Proper Oligodendrocyte Iron Homeostasis and Development," *J. Neurosci.*, vol. 43, no. 20, pp. 3614–3629, May 2023, doi: 10.1523/JNEUROSCI.1383-22.2023.

[110] D. Fulton, P. M. Paez, and A. T. Campagnoni, "The multiple roles of myelin protein genes during the development of the oligodendrocyte," *ASN Neuro*, vol. 2, no. 1, pp. 25–37, Feb. 2010, doi: 10.1042/AN20090051/ASSET/IMAGES/LARGE/10.1042_AN20090051-FIG1.JPEG.

[111] S. J. Chun, M. N. Rasband, R. L. Sidman, A. A. Habib, and T. Vartanian, "Integrin-linked kinase is required for laminin-2–induced oligodendrocyte cell spreading and CNS myelination," *J. Cell Biol.*, vol. 163, no. 2, pp. 397–408, Oct. 2003, doi: 10.1083/jcb.200304154.

[112] M. Frank, N. Schaeren-Wiemers, R. Schneider, and M. E. Schwab, "Developmental Expression Pattern of the Myelin ProteolipiMAL Indicates Different Functions of MAL for Immature Schwann Cells and in a Late Step of CNS Myelinogenesis," *J. Neurochem.*, vol. 73, no. 2, pp. 587–597, Aug. 1999, doi: 10.1046/J.1471-4159.1999.0730587.X.

[113] F. Mei *et al.*, "Stage-Specific Deletion of Olig2 Conveys Opposing Functions on Differentiation and Maturation of Oligodendrocytes," *J. Neurosci.*, vol. 33, no. 19, pp. 8454–8462, May 2013, doi: 10.1523/JNEUROSCI.2453-12.2013.

[114] R. H. Quarles, "Myelin-associated glycoprotein (MAG): past, present and beyond," *J. Neurochem.*, vol. 100, no. 6, pp. 1431–1448, Mar. 2007, doi: 10.1111/J.1471-4159.2006.04319.X.

[115] H. Yoon *et al.*, "Blocking Kallikrein 6 promotes developmental myelination," *Glia*, vol. 70, no. 3, pp. 430–450, 2022, doi: 10.1002/glia.24100.

[116] A. A. Shulgin, T. D. Lebedev, V. S. Prassolov, and P. V. Spirin, "Plasmolipin and Its Role in Cell Processes," *Mol. Biol.*, vol. 55, no. 6, pp. 773–785, Nov. 2021, doi: 10.1134/S0026893321050113/FIGURES/5.

[117] Y. Yaffe *et al.*, "The myelin proteolipid plasmolipin forms oligomers and induces liquid-ordered membranes in the Golgi complex," *J. Cell Sci.*, vol. 128, no. 13, pp. 2293–2302, Jul. 2015, doi: 10.1242/JCS.166249/VIDEO-3.

[118] A. Holz and M. E. Schwab, "Developmental expression of the myelin gene MOBP in the rat nervous system," *J. Neurocytol.*, vol. 26, no. 7, pp. 467–477, 1997, doi: 10.1023/A:1018529323734/METRICS.

[119] P. Montague, A. S. McCallion, R. W. Davies, and I. R. Griffiths, "Myelin-Associated Oligodendrocytic Basic Protein: A Family of Abundant CNS Myelin Proteins in Search of a Function," *Dev. Neurosci.*, vol. 28, no. 6, pp. 479–487, Oct. 2006, doi: 10.1159/000095110.

[120] P. Vourc'h, S. Dessay, O. Mbarek, S. Marouillat Védrine, J.-P. Müh, and C. Andres, "The oligodendrocyte-myelin glycoprotein gene is highly expressed during the late stages of myelination in the rat central nervous system," *Dev. Brain Res.*, vol. 144, no. 2, pp. 159–168, Sep. 2003, doi: 10.1016/S0165-3806(03)00167-6.

[121] A. R. Denninger *et al.*, "Claudin-11 Tight Junctions in Myelin Are a Barrier to Diffusion and Lack Strong Adhesive Properties," *Biophys. J.*, vol. 109, no. 7, pp. 1387–1397, Oct. 2015, doi: 10.1016/j.bpj.2015.08.012.

[122] K. J. Maheras, M. Peppi, F. Ghoddoussi, M. P. Galloway, S. A. Perrine, and A. Gow, "Absence of Claudin 11 in CNS Myelin Perturbs Behavior and Neurotransmitter Levels in Mice," *Sci. Rep. 2018 81*, vol. 8, no. 1, pp. 1–16, Feb. 2018, doi: 10.1038/S41598-018-22047-9.

[123] J. Marcus, S. Honigbaum, S. Shroff, K. Honke, J. Rosenbluth, and J. L. Dupree, "Sulfatide is essential for the maintenance of CNS myelin and axon structure," *Glia*, vol. 53, no. 4, pp. 372–381, Mar. 2006, doi: 10.1002/GLIA.20292.

[124] H. Ramakrishnan *et al.*, "Increasing Sulfatide Synthesis in Myelin-Forming Cells of Arylsulfatase A-Deficient Mice Causes Demyelination and Neurological Symptoms Reminiscent of Human Metachromatic Leukodystrophy," *J. Neurosci.*, vol. 27, no. 35, pp. 9482–9490, Aug. 2007, doi: 10.1523/JNEUROSCI.2287-07.2007.

[125] Y. Du and C. F. Dreyfus, "Oligodendrocytes as providers of growth factors," *J. Neurosci. Res.*, vol. 68, no. 6, pp. 647–654, Jun. 2002, doi: 10.1002/JNR.10245.

[126] M. R. Gerber and J. R. Connor, "Do oligodendrocytes mediate iron regulation in the human brain?," *Ann. Neurol.*, vol. 26, no. 1, pp. 95–98, Jul. 1989, doi: 10.1002/ANA.410260115.

[127] H. Zeng *et al.*, "Large-scale cellular-resolution gene profiling in human neocortex reveals species-specific molecular signatures," *Cell*, vol. 149, no. 2, pp. 483–496, Apr. 2012, doi: 10.1016/j.cell.2012.02.052.

[128] J. Han, J. R. Day, J. R. Connor, and J. L. Beard, "H and L Ferritin Subunit mRNA Expression Differs in Brains of Control and Iron-Deficient Rats," *J. Nutr.*, vol. 132, no. 9, pp. 2769–2774, Sep. 2002, doi: 10.1093/JN/132.9.2769.

[129] M. Clark and R. D. Cramer III, "The Probability of Chance Correlation Using Partial Least Squares (PLS)," *Quant. Struct.-Act. Relatsh.*, vol. 12, no. 2, pp. 137–145, 1993, doi: 10.1002/qsar.19930120205.

[130] J. Chen, N.-J. Gong, T. Chaim, M. Concepción, G. Otaduy, and C. Liu, "Decompose quantitative susceptibility mapping (QSM) to sub-voxel diamagnetic and paramagnetic components based on gradient-echo MRI data," *NeuroImage*, vol. 242, pp. 118477–118477, 2021, doi: 10.1016/j.neuroimage.2021.118477.

[131] J. Chifman *et al.*, "The core control system of intracellular iron homeostasis: A mathematical model," *J. Theor. Biol.*, vol. 300, pp. 91–99, May 2012, doi: 10.1016/j.jtbi.2012.01.024.

[132] T. A. Rouault, D.-L. Zhang, and S. Y. Jeong, "Brain iron homeostasis, the choroid plexus, and localization of iron transport proteins," *Metab. Brain Dis.*, vol. 24, no. 4, pp. 673–684, Dec. 2009, doi: 10.1007/s11011-009-9169-y.

[133] E. A. Malecki, B. M. Cook, A. G. Devenyi, J. L. Beard, and J. R. Connor, "Transferrin is required for normal distribution of Fe and Mn in q mouse brain," *J. Neurol. Sci.*, vol. 170, pp. 112–118, 1999.

[134] A. J. Dwork *et al.*, "An autoradiographic study of the uptake and distribution of iron by the brain of the young rat," *Brain Res.*, vol. 518, no. 1–2, pp. 31–39, Jun. 1990, doi: 10.1016/0006-8993(90)90950-G.

[135] G. Grimmett and D. Stirzaker, *Probability and random processes*, 4th ed. Oxford University Press, 2020.

[136] B. A. Craig and P. P. Sendi, "Estimation of the transition matrix of a discrete-time Markov chain," *Health Econ.*, vol. 11, no. 1, pp. 33–42, 2002, doi: 10.1002/hec.654.

[137] J. Helenius *et al.*, "Cerebral hemodynamics in a healthy population measured by dynamic susceptibility contrast MR imaging," *Acta Radiol.*, vol. 44, no. 5, pp. 538–546, Sep. 2003, doi: 10.1080/J.1600-0455.2003.00104.X.

[138] A. J. Farrall and J. M. Wardlaw, "Blood–brain barrier: Ageing and microvascular disease – systematic review and meta-analysis," *Neurobiol. Aging*, vol. 30, no. 3, pp. 337–352, Mar. 2009, doi: 10.1016/j.neurobiolaging.2007.07.015.

[139] I. H. Ha, C. Lim, Y. Kim, Y. Moon, S.-H. Han, and W.-J. Moon, "Regional Differences in Blood-Brain Barrier Permeability in Cognitively Normal Elderly Subjects: A Dynamic Contrast-Enhanced MRI-Based Study," *Korean J. Radiol.*, vol. 22, no. 7, pp. 1152–1162, Jul. 2021, doi: 10.3348/kjr.2020.0816.

[140] E. Ficiarà *et al.*, "A mathematical model for the evaluation of iron transport across the blood-cerebrospinal fluid barrier in neurodegenerative diseases," in *2020 42nd Annual International Conference of the IEEE Engineering in Medicine & Biology Society (EMBC)*, Jul. 2020, pp. 2270–2273. doi: 10.1109/EMBC44109.2020.9175988.

[141] J. Bernal *et al.*, "A four-dimensional computational model of dynamic contrast-enhanced magnetic resonance imaging measurement of subtle blood-brain barrier leakage," *NeuroImage*, vol. 230, p. 117786, Apr. 2021, doi: 10.1016/j.neuroimage.2021.117786.

[142] P. Mukherjee, J. I. Berman, S. W. Chung, C. P. Hess, and R. G. Henry, "Diffusion Tensor MR Imaging and Fiber Tractography: Theoretic Underpinnings," *Am. J. Neuroradiol.*, vol. 29, no. 4, pp. 632–641, Apr. 2008, doi: 10.3174/ajnr.A1051.

[143] C. Beaulieu, "The basis of anisotropic water diffusion in the nervous system – a technical review," *NMR Biomed.*, vol. 15, no. 7–8, pp. 435–455, Nov. 2002, doi: 10.1002/nbm.782.

[144] T. Moos and T. Rosengren Nielsen, "Ferroportin in the Postnatal Rat Brain: Implications for Axonal Transport and Neuronal Export of Iron," *Semin. Pediatr. Neurol.*, vol. 13, no. 3, pp. 149–157, Sep. 2006, doi: 10.1016/j.spen.2006.08.003.

[145] P. Zhang *et al.*, "Electron tomography of degenerating neurons in mice with abnormal regulation of iron metabolism," *J. Struct. Biol.*, vol. 150, no. 2, pp. 144–153, May 2005, doi: 10.1016/j.jsb.2005.01.007.

[146] C. Mukherjee *et al.*, "Oligodendrocytes Provide Antioxidant Defense Function for Neurons by Secreting Ferritin Heavy Chain," *Cell Metab.*, vol. 32, no. 2, pp. 259-272.e10, Aug. 2020, doi: 10.1016/j.cmet.2020.05.019.

[147] L. J. O'Donnell and C.-F. Westin, "An introduction to diffusion tensor image analysis," *Neurosurg. Clin. N. Am.*, vol. 22, no. 2, pp. 185–viii, Apr. 2011, doi: 10.1016/j.nec.2010.12.004.

[148] S. Mori *et al.*, "Stereotaxic White Matter Atlas Based on Diffusion Tensor Imaging in an ICBM Template," *NeuroImage*, vol. 40, no. 2, pp. 570–582, Apr. 2008, doi: 10.1016/j.neuroimage.2007.12.035.

[149] G. Casella and R. L. Berger, *Statistical Inference*, 2nd ed. Australia: Thomson Learning, 2002.

[150] S. Mori, K. Oishi, and A. V. Faria, "White matter atlases based on diffusion tensor imaging," *Curr. Opin. Neurol.*, vol. 22, no. 4, pp. 362–369, Aug. 2009, doi: 10.1097/WCO.0b013e32832d954b.

[151] X. Tang *et al.*, "Multi-Contrast Multi-Atlas Parcellation of Diffusion Tensor Imaging of the Human Brain," *PLoS ONE*, vol. 9, no. 5, p. e96985, May 2014, doi: 10.1371/journal.pone.0096985.

[152] X. Shen, H. Yang, D. Zhang, and H. Jiang, "Iron Concentration Does Not Differ in Blood but Tends to Decrease in Cerebrospinal Fluid in Parkinson's Disease," *Front. Neurosci.*, vol. 13, p. 939, 2019, doi: 10.3389/fnins.2019.00939.

[153] M. J. Simon and J. J. Iliff, "Regulation of cerebrospinal fluid (CSF) flow in neurodegenerative, neurovascular and neuroinflammatory disease," *Biochim. Biophys. Acta BBA - Mol. Basis Dis.*, vol. 1862, no. 3, pp. 442–451, Mar. 2016, doi: 10.1016/j.bbadis.2015.10.014.

[154] D. A. Bórquez, F. Castro, M. T. Núñez, and P. J. Urrutia, "New Players in Neuronal Iron Homeostasis: Insights from CRISPRi Studies," *Antioxidants*, vol. 11, no. 9, Art. no. 9, Sep. 2022, doi: 10.3390/antiox11091807.

[155] T. Sato, J. S. Shapiro, H.-C. Chang, R. A. Miller, and H. Ardehali, "Aging is associated with increased brain iron through cortex-derived hepcidin expression," *eLife*, vol. 11, p. e73456, Jan. 2022, doi: 10.7554/eLife.73456.

[156] P. Garrido-Gil, J. Rodriguez-Pallares, A. Dominguez-Meijide, M. J. Guerra, and J. L. Labandeira-Garcia, "Brain angiotensin regulates iron homeostasis in dopaminergic neurons and microglial cells," *Exp. Neurol.*, vol. 250, pp. 384–396, Dec. 2013, doi: 10.1016/j.expneurol.2013.10.013.

[157] W. Li *et al.*, "A method for estimating and removing streaking artifacts in quantitative susceptibility mapping," *NeuroImage*, vol. 108, pp. 111–122, Mar. 2015, doi: 10.1016/j.neuroimage.2014.12.043.

[158] E. T. Rolls, C.-C. Huang, C.-P. Lin, J. Feng, and M. Joliot, "Automated anatomical labelling atlas 3," *NeuroImage*, vol. 206, p. 116189, Feb. 2020, doi: 10.1016/j.neuroimage.2019.116189.

[159] MOSEK ApS, "The MOSEK optimization toolbox for MATLAB manual. Version 10.0." 2023. [Online]. Available: https://docs.mosek.com/10.0/toolbox/index.html

[160] M. Grant and S. Boyd, "CVX: Matlab software for disciplined convex programming, version 2.0 beta." Sep. 2013. [Online]. Available: http://cvxr.com/cvx

[161] M. Grant and S. Boyd, "Graph implementations for nonsmooth convex programs," in *Recent Advances in Learning and Control*, V. Blondel, S. Boyd, and H. Kimura, Eds., in Lecture Notes in Control and Information Sciences. , Springer-Verlag Limited, 2008, pp. 95--110. [Online]. Available: http://stanford.edu/~boyd/graph_dcp.html

[162] L.-N. Lu, Z.-M. Qian, K.-C. Wu, W.-H. Yung, and Y. Ke, "Expression of Iron Transporters and Pathological Hallmarks of Parkinson's and Alzheimer's Diseases in the Brain of Young, Adult, and Aged Rats," *Mol. Neurobiol.*, vol. 54, no. 7, pp. 5213–5224, Sep. 2017, doi: 10.1007/s12035-016-0067-0.

[163] M. Mezzanotte, G. Ammirata, M. Boido, S. Stanga, and A. Roetto, "BBB damage in aging causes brain iron deposits via astrocyte-neuron crosstalk and Hepc/Fpn1 pathway," Neuroscience, preprint, Jul. 2021. doi: 10.1101/2021.07.01.450665.

[164] W. R. Marchand, "Cortico-basal ganglia circuitry: a review of key research and implications for functional connectivity studies of mood and anxiety disorders," *Brain Struct. Funct.*, vol. 215, no. 2, pp. 73–96, Dec. 2010, doi: 10.1007/s00429-010-0280-y.

[165] B. Draganski *et al.*, "Evidence for Segregated and Integrative Connectivity Patterns in the Human Basal Ganglia," *J. Neurosci.*, vol. 28, no. 28, pp. 7143–7152, Jul. 2008, doi: 10.1523/JNEUROSCI.1486-08.2008.

[166] I. C. M. Verheggen *et al.*, "Increase in blood–brain barrier leakage in healthy, older adults," *GeroScience*, vol. 42, no. 4, pp. 1183–1193, Aug. 2020, doi: 10.1007/s11357-020-00211-2.

[167] M. F. Callaghan *et al.*, "Widespread age-related differences in the human brain microstructure revealed by quantitative magnetic resonance imaging," *Neurobiol. Aging*, vol. 35, no. 8, pp. 1862–1872, Aug. 2014, doi: 10.1016/j.neurobiolaging.2014.02.008.

[168] N. Spotorno *et al.*, "Relationship between cortical iron and tau aggregation in Alzheimer's disease," *Brain*, vol. 143, no. 5, pp. 1341–1349, May 2020, doi: 10.1093/brain/awaa089.

[169] S. Mandel, T. Amit, O. Bar-Am, and M. B. H. Youdim, "Iron dysregulation in Alzheimer's disease: Multimodal brain permeable iron chelating drugs, possessing neuroprotective-neurorescue and amyloid precursor protein-processing regulatory activities as therapeutic agents," *Prog. Neurobiol.*, vol. 82, no. 6, pp. 348–360, Aug. 2007, doi: 10.1016/j.pneurobio.2007.06.001.

[170] J. R. Connor, B. S. Snyder, J. L. Beard, R. E. Fine, and E. J. Mufson, "Regional distribution of iron and iron-regulatory proteins in the brain in aging and Alzheimer's disease," *J. Neurosci. Res.*, vol. 31, no. 2, pp. 327–335, 1992, doi: 10.1002/jnr.490310214.

[171] A. Damulina *et al.*, "Cross-sectional and Longitudinal Assessment of Brain Iron Level in Alzheimer Disease Using 3-T MRI," *Radiology*, vol. 296, no. 3, pp. 619–626, Sep. 2020, doi: 10.1148/radiol.2020192541.

[172] S. M. Kagerer *et al.*, "APOE4 moderates effects of cortical iron on synchronized default mode network activity in cognitively healthy old-aged adults," *Alzheimers Dement. Diagn. Assess. Dis. Monit.*, vol. 12, no. 1, p. e12002, 2020, doi: 10.1002/dad2.12002.

[173] S. S. Rao and P. A. Adlard, "Untangling Tau and Iron: Exploring the Interaction Between Iron and Tau in Neurodegeneration," *Front. Mol. Neurosci.*, vol. 11, p. 276, Aug. 2018, doi: 10.3389/fnmol.2018.00276.

[174] W.-J. Moon *et al.*, "Hippocampal blood–brain barrier permeability is related to the APOE4 mutation status of elderly individuals without dementia," *J. Cereb. Blood Flow Metab.*, vol. 41, no. 6, pp. 1351–1361, Jun. 2021, doi: 10.1177/0271678X20952012.

[175] A. Škoch *et al.*, "Human brain structural connectivity matrices–ready for modelling," *Sci. Data*, vol. 9, no. 1, Art. no. 1, Aug. 2022, doi: 10.1038/s41597-022-01596-9.

[176] C. Sudlow *et al.*, "UK Biobank: An Open Access Resource for Identifying the Causes of a Wide Range of Complex Diseases of Middle and Old Age," *PLoS Med.*, vol. 12, no. 3, p. e1001779, Mar. 2015, doi: 10.1371/journal.pmed.1001779.